UNIVERSITY OF OKLAHOMA

GRADUATE COLLEGE

RADIO-FREQUENCY EMISSIONS FROM RUNAWAY ELECTRON AVALANCHE MODELS COMPARED WITH INTENSE, TRANSIENT RADIO-FREQUENCY SIGNALS ASSOCIATED WITH THUNDERSTORMS

A Dissertation

SUBMITED TO THE GRADUATE FACULTY

in partial fulfillment of the requirements for the

degree of

Doctor of Philosophy

By

HEIDI ELLEN TIERNEY
Noman, Oklahoma
2002

UMI Number: 3056944

ProQuest Information and Learning Company
300 North Zeeb Road
P.O. Box 1346
Ann Arbor, MI 48106-1346

RADIO-FREQUENCY EMISSIONS FROM RUNAWAY ELECTRON AVALANCHE MODELS COMPARED WITH INTENSE, TRANSIENT RADIO-FREQUENCY SIGNALS ASSOCIATED WITH THUNDERSTORMS

A Dissertation APPROVED FOR THE DEPARTMENT OF PHYSICS AND ASTRONOMY

BY

William H. Beasley, Co-chair

Michael Morrison, ~~Co-chair~~

Robert Roussel-Dupré, LANL Advisor

Andrew Miller

W. David Rust

Stewart Ryan

Acknowledgments

My advisor at the University of Oklahoma, Dr. William Beasley, said that mentoring a graduate student is like being the center track for a car ride at an amusement park. The drivers are allowed to steer but are caught by this track when they get too far off course. Dr. Beasley had always encouraged me to follow my interests, and found ways to provide financial support if necessary. I believe that it is a great thing to find an advisor who values the scientific process above convenience.

I would also like to thank Dr. Robert Roussel-Dupré of Los Alamos National Laboratory (LANL) for providing a fascinating dissertation topic. For much of the time spent working on my thesis research I was a member of the Atmospheric and Climate Science group, EES-8. I would like to thank this group and the Department of Energy for financial and intellectual support. Dr. Robert Roussel-Dupré and Dr. Eugene Symbalisty have been developing a fully electromagnetic and hydrodynamic lightning code for many years. This background work was essential for the present work. Many others at LANL deserve recognition. I would like to thank Dr. Abram Jacobson and all members of the FORTE satellite team for providing access to, and instruction on, the FORTE satellite data.

I am grateful to my husband, Tom Tierney, who is also currently finishing his dissertation in physics, for his friendship and our interesting conversations. My scientific and artistic mother, Katherine Bachman, is my favorite role model. I thank my grandparents Miles and Anne MacGran, and Clara Morris, for being constant sources of support and love throughout my life. Finally, I would like to thank my dear aunt, Ellen MacGran, who has taught me to visualize ideal situations and make them reality.

Chapter 1

Introduction

Observations of intense transient radiation pulses, lasting only microseconds, using ground based, [*Le Vine*, 1980; *Shao et al.*, 1996b; *Smith*, 1998; *Smith and Holden*, 1996; *Willett et al.*, 1989] and space-based [*Holden et al.*, 1995; *Massey and Holden*, 1995; *Massey et al.*, 1998] instruments motivate further investigation of the production of radio frequency (RF) radiation from lightning. The transient signals discussed in this dissertation are unique in comparison with other RF signals produced by lightning because of their short timescale, broadband spectrum, intensity, and temporal isolation from other activity. Ground-based observations have shown that intense, relatively isolated waveforms in the very high frequency (HF/VHF) range (3-30 and 30-300 MHz) are time correlated with a class of waveforms measured in the medium frequency (MF) range (300-3000 kHz) and below and known as narrow bipolar pulses (NBPs). In space-based observations transient, broadband VHF pulses are often recorded in association with lightning. Though several types of signals have been classified, one group in particular has been analyzed in detail; these are transionospheric pulse pairs (TIPPs). TIPP signals have origins kilometers above the ground, have temporal 1/e widths on the order of microseconds, and can appear to be part of a lightning flash of longer duration or can occur in isolation. For a satellite-recorded event to be classified as a TIPP, two distinct pulses separated by several to tens of microseconds must be recorded in a single data record. The occurrence of solitary, or pairs of, VHF pulses in pairs at space-based receivers is not unusual. And it is not presently clear what these events are in terms of the charged particles that produce them. Hypotheses of these sources and tests thereof are the core of this dissertation. One additional motivation to investigate VHF radiation signals produced by lightning is recent observational evidence that suggests that they may be associated with lightning initiation. Investigators at New Mexico Tech (NMT) have shown that a very intense VHF pulse can be the first event recorded of an intracloud lightning discharge [*Thomas et al.*, 2001].

Scientists from the fields of laboratory spark physics, theoretical physics, and meteorology are currently working on models that are applied to the lightning discharge. The present work focuses on runaway breakdown theory. Its application to lightning-related events has been investigated over about the past ten years. The conceptual model begins with a thunderstorm electric field that exists over a large spatial scale. The required strength of this ambient electric field is 0.22 MV/(m·Atm) ,which is about ten times less intense than that required for a conventional discharge in air. A high energy (~1 MeV) seed electron, which is one of a ubiquitous background population of cosmic ray secondary electrons, can maintain its energy in this field and create more high-energy and low-energy electrons through ionization processes.

The recent interest in the application of runaway theory to lightning is in large measure a result of observational evidence. It is well known that high-energy electrons of a runaway avalanche, with characteristic mean energy of 7.2 MeV, produce bremsstrahlung X rays [*Roussel-Dupré et al.*, 1994]. Recently, *Eack*, [1997] was the first to obtain measurements of increased X-ray intensity associated with increases in ambient electric fields in thunderstorms. In addition, after many years of failed attempts by many competent scientists, "bursts of radiation with energies in excess of 1 MeV" have just recently been observed in conjunction with the stepped-leader process of lightning [*Moore et al.*, 2001]. The radiation bursts subsided with the onset of the return stroke. Because measured electron energies in conventional breakdown are on the order of 10 eV, X radiation will not be produced by a bremsstrahlung process.

The runaway avalanche is believed to develop with relativistic speed, and it has already been suggested that ionization by high-energy electrons may be in part responsible for the stepped leader process of a cloud-to-ground discharge [*Roussel-Dupré et al.*, 2000]. Although the velocity of a single step of a stepped leader has not been resolved, it is known that it exceeds 5.0×10^7m/s [*Uman*, 1987]. It has been noted by *Labaune et al.* [1990] that there is a major class of VHF radiators with estimated propagation speed of 2.0×10^7 m/s. This author states, "[i]t must be remembered that this type of event cannot be directly linked to a conventional discharge phenomena due to the very low charge transfers involved." Furthermore, relativistic electron beams can form narrow, conducting channels in air. An experimental study of relativistic electron beams in neutral gases revealed, for N_2:O_2=4:1 and a pressure of 600 Torr (about 800 mB, or approximately 2 km above sea level in the U.S. Standard Atmosphere), that the beam conductivity becomes confined to a 1-cm radius after 60 ns, and the conductivity on the propagation axis at this time is higher than the initial value [*Kondratiev et al.*, 1991]. The electron energy in this experiment was $1\text{-}1.2\times10^6$ eV, and for a pressure of 760 Torr (1 atm) the maximum applied electric field was about 10^4V/cm.

The application of runaway theory to the stepped leader of lightning seems to be justified at this time in part because of the documented X-ray measurements. The source of the current change, which produces both a narrow bipolar pulse signal and a strong

VHF impulse, may or may not involve a runaway avalanche. For example, it is not known whether X rays are time-correlated with narrow bipolar pulse signals. Also, the typical propagation speed(s) of currents that produce narrow bipolar pulses and strong VHF radiation can only be estimated based on estimates of stepped-leader and return-stroke current speeds. However, both stepped leaders and the currents that produce NBP signals are believed to be associated with the initial breakdown of air [*Smith*, 1998]. It is reasonable, therefore, to investigate application of runaway theory to the events that produce NBPs and strong VHF impulses as a first "step" towards increased understanding of these and possibly other lightning discharge processes. In particular, it may be that lightning initiation involves runaway processes.

1.1 Fundamental Considerations

Peak electric-field amplitudes in the time domain and spectral intensities in the HF/VHF radio range are investigated in this thesis for runaway electron avalanches. There are several other measurable quantities associated with lightning that are routinely observed and compared with models. These include X-ray, optical, thermal, and acoustic intensities among others. Models that simultaneously account for various observations including the RF emissions are being produced in the context of runaway and conventional breakdown. However, little is understood about the VHF radiation in particular. It seems to be something of an enigma. Once the VHF-producer is thought to be understood in terms of a conceptual model, new observations will contradict the belief. For example, observations of TIPPs were originally thought, unequivocally, to resemble noise. This was because of the broadband, non-smooth appearance of the VHF spectra associated with the electric-field waveforms recorded at the satellite. A picture developed that the VHF impulses were radiated from many small "bristle-brush" channels around a larger lightning channel. However, it was later learned that a subset of the very strong VHF impulses were anti-correlated with strong optical radiation. Thus, an energetic event that heats the air and produces strong optical emissions, such as a return-stroke lightning channel, doesn't always co-exist with a strong VHF producer. Later it was learned that many so-called TIPPs possess a strong degree of polarization. This lead investigators to believe that at least some of the VHF impulses were produced by a less noise-like source. Of course there is not only one process that produces VHF radio impulses. However, the process that simultaneously produces intense VHF and NBP signals and that also may be associated with lightning initiation is the focus here. The following paragraphs discuss some fundamental properties of radio-frequency radiation and what can be learned about the sources of the radiation using models and observations.

1.1.1 Time scale

A runaway electron avalanche, as described above, provides initial ionization of air where the electric field is sufficient within a thunderstorm and may also produce strong VHF radiation. Traveling with relativistic speed, the high-energy electrons of the avalanche would traverse the distance between the thunderstorm charge layers in microseconds. The overall duration of the VHF radiation associated with NBPs is on the order of microseconds. Relativistic effects would further compress the electromagnetic radiation in time and would thus increase the intensity of the signal and the VHF frequency content. Current variations with real, or apparent, characteristic time scales of

~1-10 ns produce VHF radiation in the 50-MHz range and are often referred to as transients. There are many anthropogenic and natural transient currents that give rise to electromagnetic pulses. Many lightning processes have current variations that occur on a short time scale and produce VHF radiation. The signals of interest here are, in addition, unusually powerful. The magnitude of the time rate of change of current, *dI/dt*, is usually advanced as an explanation for the powerful signals. The question then becomes: what charged source under the influence of what forces can produce the *dI/dt* required for the strong VHF impulses?

1.1.2 Calculation of Radiation Field

A general expression for calculating the radiation electric field, E, is given in Eq (1.1) [*Jackson*, 1975]. This expression is derived by substituting $\mathbf{B}=\nabla\times\mathbf{A}$ into Faraday's law and noting that the curl of the gradient of a scalar function is zero. Note the dependence of the magnitude of the radiated electric field on the time variation of the current. Below, A is the vector potential, c is the speed of light, and J is the current flowing through a unit cross sectional area dS', where $dV'=dz'dS'$ (cgs units). The electronic charge is denoted e, the electron drift velocity is u_e, and the charge density is n_e.

$$\vec{E}(\vec{r},t) = -\nabla\phi(\vec{r},t) - \frac{1}{c}\frac{\partial\vec{A}(\vec{r},t)}{\partial t} \tag{1.1a}$$

$$\text{where } \vec{A}(\vec{r},t) = \frac{1}{c}\int_{V'}\frac{\vec{J}(r',t-|\vec{r}-\vec{r}'|/c)}{|\vec{r}-\vec{r}'|}dV' \tag{1.1b}$$

$$\text{and } \vec{J} = (-e)n_e\vec{u}_e\,. \tag{1.1c}$$

The electric field contribution from the scalar potential, first term on the right hand side of 1.1a, is not important in the radiation zone and is not included here. Note that the scalar potential falls off like $1/r$ and the spatial derivative of a function with this r dependence essentially falls off like $1/r^2$. The component of **A** transverse to the propagation vector, A_θ, is the important contributor in the radiation zone (see, for example, *Uman et al.*, [1975]). A spherical coordinate system centered at a current element is shown in Figure 1.1.

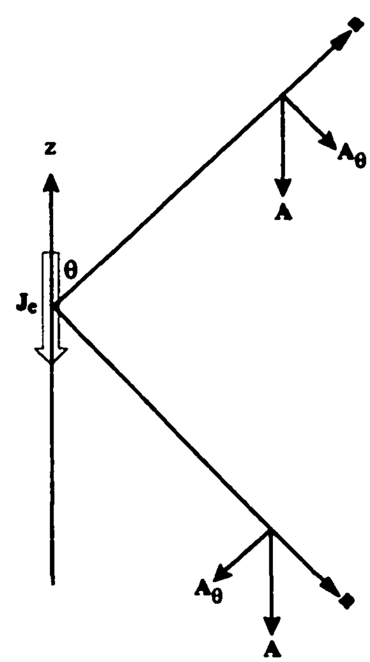

Figure 1.1. Electron current $\mathbf{J}_e$ density, total vector potential **A**, and vector potential transverse ($\mathbf{A}_\theta$) to wave propagation direction, **n** for upward moving electron current increasing in magnitude with time.

For many applications, such as for a model of a straight lightning channel or antenna, it is sufficient to model the current as a one-dimensional source. For these circumstances one can convert from an integral over volume to an integral over length using $dV'=dS'\cdot dz'$ and $J=I/dS'$. Thus, Eq (1.1a) can be written as

$$\bar{E}_\theta(\bar{r},t) = -\frac{\partial}{\partial t}\frac{1}{c^2}\int_{z'}\frac{I_z(z',t-|\bar{r}-z'|/c)}{|\bar{r}-z'|}\sin\theta dz' \ . \tag{1.2}$$

The radiated electric field is proportional to the time derivative of the spatially integrated current. The current change can be a result of charge acceleration, or an increase or decrease in the charge magnitude.

The power radiated as a function of angle has a familiar $sin^2\theta$ dependence for non-relativistic currents. Consider the general analytic expression for electromagnetic power radiated per unit solid angle by an accelerating point charge [*Jackson*, 1975]. The following equation applies to a charge with velocity, u, and acceleration, a, in the same direction.

$$\frac{\partial P(t')}{\partial\Omega} = \frac{e^2 a^2}{4\pi c^3}\frac{\sin^2\theta}{(1-\beta\cos\theta)^5} \tag{1.3}$$

In Eq (1.3), β is the ratio of the electron velocity to the speed of light. For small β the angular distribution of the radiated power has a $sin^2\theta$ dependence. The angular factor of Eq (1.3) is plotted in Figure 1.2 for β=0.987 and β=0.001. The acceleration and constant coefficient are taken to be equal for the relativistic and non-relativistic charges. For the charge with dimensionless speed β=0.987 the angle of peak radiated power is about 4.75° and the maximum value of the angular factor is about 5.8×10^6. For the charge with β=0.001, the angular factor has a maximum at about 88.5 degrees and a value of about 1.0006.

For these two point charges, which are assumed to be accelerating along straight lines, the charge of relatively low velocity is radiating much more isotropically. For a dipole radiator the solid angle average of the angular factor is

$$\frac{1}{4\pi}\int_S \sin^2\theta d\Omega = \frac{2}{3} \quad , \quad where \quad d\Omega = d\phi \sin\theta d\theta \,. \tag{1.4}$$

The power is azimuthially symmetric and the phi integral gives a factor of 2π. Since the maximum of the angular factor is 1.0 for a perfect dipole, by assuming that this amplitude applies at every angle, the total power is only overestimated by 50%. Of course the power will not, in general, be sampled where it is a maximum. Therefore, if the source is a true dipole radiator one can obtain an order-of-magnitude estimate for the power radiated from the source by assuming that the power is radiated isotropically.

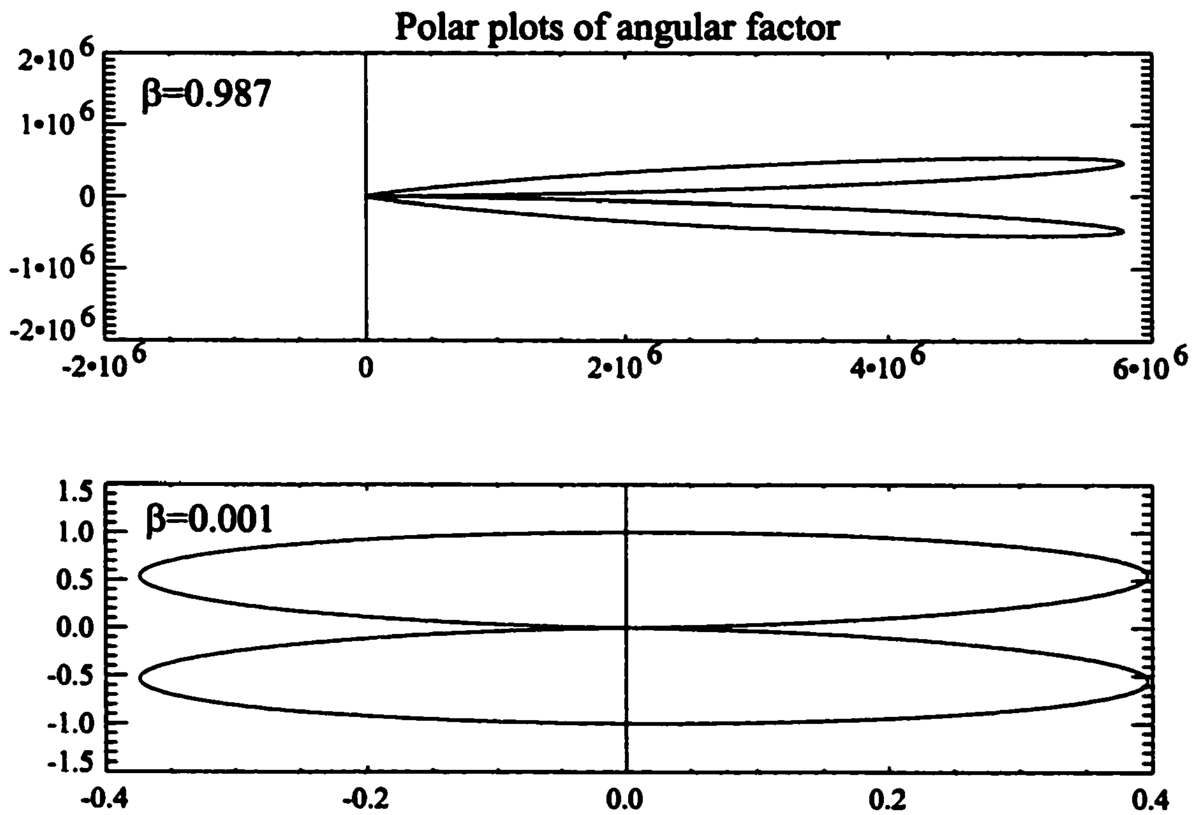

Figure 1.2. Angular factor of Eq (1.3) for a relativistic (top) and a relatively non-relativistic (bottom) accelerating point charge.

Furthermore, the direction of charge motion can be deduced from the electric field change. For a static electric field change, a removal of negative charge from its initial position above a ground-based observer results in a negative vertical electric field change. This is the case in a negative cloud-to-ground discharge, which lowers negative charge to Earth. Most return-stroke electric-field-change waveforms are negative. According to the "physics convention" an electric-field vector points in the direction that a positive charge would move if released, from rest, from a point in space. In a coordinate system on the surface of the Earth with the z axis pointing upward the static vertical electric field points in the positive z direction. In Figure 1.3 only the z component of the static electric field is drawn. If the observer is above the negative charge, the z-component of the static field is initially negative and goes to zero, so the field change would be positive.

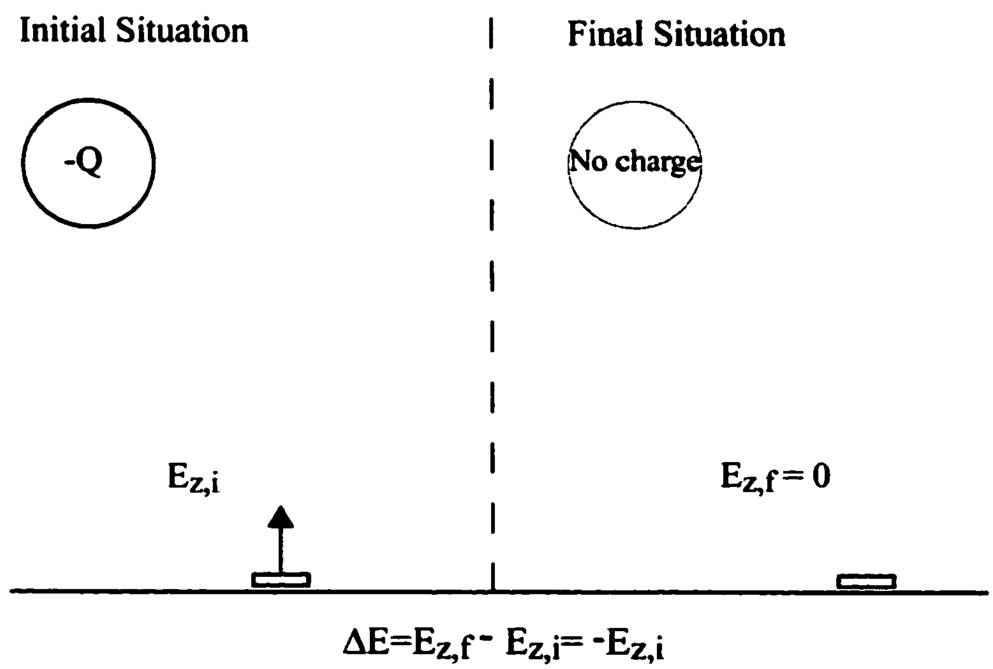

Figure 1.3. Static electric field change diagram. A lowering of negative charge to the ground (or a removal of negative charge overhead), as in the –CG discharge, produces a negative field change as viewed from the surface of the Earth.

Consider a current of electrons that is moving upward (+z) above the surface of the Earth and increasing in magnitude with time (Figure 1.1). The direction of electron current is in the -z direction in the physics convention. The velocity vector is positive in Eq (1.1c), but the charge of the electron is negative. The vector potential, **A**, has the same direction as the current. Far from the current, the transverse component of the vector potential, A_θ, alone contributes to the radiation electric field. The radiation electric field is $-dA/dt$, and points in the $-\theta$, or $\mathbf{n}\times(\mathbf{n}\times\mathbf{J}_e)$, direction. For a dipole radiation pattern, and an observation angle of 90°, the electric field vector will be in the +z direction and it can be concluded from the sign of the observed waveform that the electron current is moving upward.

Note also that by rotating Figure 1.1 so that a relativistic electron avalanche is moving horizontal to the ground, and generally toward a ground-based observer, a vertical component of the radiated electric field will be observed. For a dipole radiation pattern, the radiated electric field is strongest at a 90-degree angle, while for a relativistic radiation pattern, the radiated electric field is strongest at a small angle from the direction of charge motion (Figure 1.2). Thus, a positive electric field or field change observed on the ground can mean that a fast current is moving roughly toward an observer. Note that if the relativistic electrons are exactly moving in a narrow line and directly toward an observer, the radiated power will be zero.

Another useful parameter that can be deduced from the electric field is the charge transferred by the discharge current. For a static configuration of charges along an axis, such as in a model thunderstorm, the dipole moment, P, is defined as

$$P = 2\sum_i Q_i H_i \, . \tag{1.5}$$

Each charge Q_i is specified by an index, i, and has an associated height, H_i, at some position along the axis relative to a common origin. Lightning discharges can alter the dipole moment of the thunderstorm so that a time-varying dipole moment can be discussed in terms of the time-varying electric fields. Assuming that the observation range, D, is much larger than any charge height, that the magnitude and phase of the discharge current is constant along the current path, and that the charge heights are constant, the expression relating the electric field to the dipole moment is

$$E = \frac{P}{4\pi\varepsilon_o D^3} + \frac{1}{4\pi\varepsilon_o c D^2}\left(\frac{dP}{dt}\right) + \frac{1}{4\pi\varepsilon_o c^2 D}\left(\frac{d^2P}{dt^2}\right). \tag{1.6}$$

Above, the first term on the right hand side is electrostatic, the second term is the induction field, and the third term is the radiation field. Given a waveform such as shown in Figure 1.6, it is common practice to estimate the charge transferred using Eq (1.6) and Eq (1.7). The charge transferred is calculated from the dipole moment using

$$\Delta Q = \frac{\Delta P}{\Delta z}. \tag{1.7}$$

Far from a discharge, the third term will dominate because it falls off less rapidly with distance than the other terms. Two integrations are needed to find E. The first integral will yield the time variation of a function that is proportional to the vector potential or current, and integration of this function followed by multiplication by a factor proportional to the range will give the dipole moment change. Sometimes the 10-90% rise time of a waveform will be considered for the calculation of the dipole moment change. Once ΔP is obtained, multiplication by the distance over which charge is transferred gives ΔQ. Note that for the runaway avalanche model considered later, the current varies as a function of time and space and so it is not appropriate to use Eq (1.6) and Eq (1.7) in the calculation of the dipole moment.

1.1.3 Phase Correlation or Coherence

Lightning electric-field-change waveforms can appear smooth or noisy. Smooth signals are often described as "coherent." Here we discuss what the meaning of coherence is and what can be learned from a waveform based on whether it appears noisy or not. Coherence, in a mathematical sense refers to the degree of correlation between two separate electromagnetic signals. This is analogous to the linear correlation coefficient of statistics. For example, if two vectors $\boldsymbol{a}$ and $\boldsymbol{b}$ have the same direction, they have a correlation coefficient of 1, or the cosine of the angle between the two vectors is one.

$$\cos\theta = \frac{\bar{a}\cdot\bar{b}}{|\bar{a}||\bar{b}|} \tag{1.8}$$

With correlation analysis, the vectors are also normalized and the correlation coefficient can be thought of as the cosine of the angle between vectors. The correlation coefficient, r, for two vectors with M elements each is defined as

$$r = \frac{\sum_{i=0}^{M-1}(x_i - \bar{x})(y_i - \bar{y})}{\sqrt{\sum_{i=0}^{M}(x_i - \bar{x})^2}\sqrt{\sum_{i=0}^{M}(y_i - \bar{y})^2}}. \tag{1.9}$$

Above, the barred quantities are the mean values of the vectors x and y. The numerator is the scalar product of the two vectors. Note that for radiation fields, the time-averaged value of the amplitude is also zero if the complete field disturbance is included. For electromagnetics a "degree of coherence" between two or more signals is measured.

For example, in Young's double-slit experiment, two slits in a screen separate monochromatic light into two sources and the intensity patterns produced by constructive and destructive interference of the two sources on a distant screen are measured. The amplitude of each source at some position on the screen as a function of time can be represented as a series of elements in a vector. The complex degree of coherence [*Beran and Parrent*, 1964] between the two signals, γ, is written

$$\gamma_{12}(\tau)=\frac{\Gamma_{12}(\tau)}{\sqrt{\Gamma_{11}(0)\Gamma_{22}(0)}}, \text{ where } \Gamma_{ab}(\tau)=\left\langle E_a(t+\tau)E_b^*(t)\right\rangle. \qquad (1.10)$$

With the fields E_1 and E_2 given in the time domain, τ is the time difference between the phases of the two signals. This value is zero for the central position on Young's screen where the intensity is a maximum. The angled brackets in Eq (1.10) signify the scalar product of the two vectors or functions within the brackets. It is often convenient to express electromagnetic fields using complex functions. The examples presented here for demonstration purposes will be real valued. The above discussion gives a precise definition of coherence.

This concept is important to the consideration of the source of the VHF impulses of interest here because a perfectly coherent superposition of N signals will increase the measured power at an antenna by N^2. If N signals with the same time-averaged amplitude, but with no phase correlation are simultaneously measured the power will be approximately N times the power from one signal. Assume that we are only looking at one component of the electric field. First consider a noise source. One can imagine that several small randomly oriented current channels radiating from a region of space can result in a noisy electromagnetic waveform at a distant antenna. Assume that the waveform as a function of time is as shown in the top plot of Figure 1.4. The spectrum of this signal is shown in the second plot of Figure 1.4. It is calculated by first computing the Fourier transform of the signal in the time domain to form *E(f)*. The energy spectral density per unit area is

$$\frac{dW}{df \cdot dA} \approx \frac{T}{376.73\Omega} \frac{|E(f)|^2}{\Delta f}. \tag{1.11}$$

Above, dW is the energy [Joules] corresponding to a frequency interval df detected per unit area dA. The impedance of free space is 376.73 Ω and T is the total duration, or period, of the pulse. If this equation were divided by T it would give the time-averaged power spectral density per unit area in the waveform [*Rybicki and Lightman*, 1979].

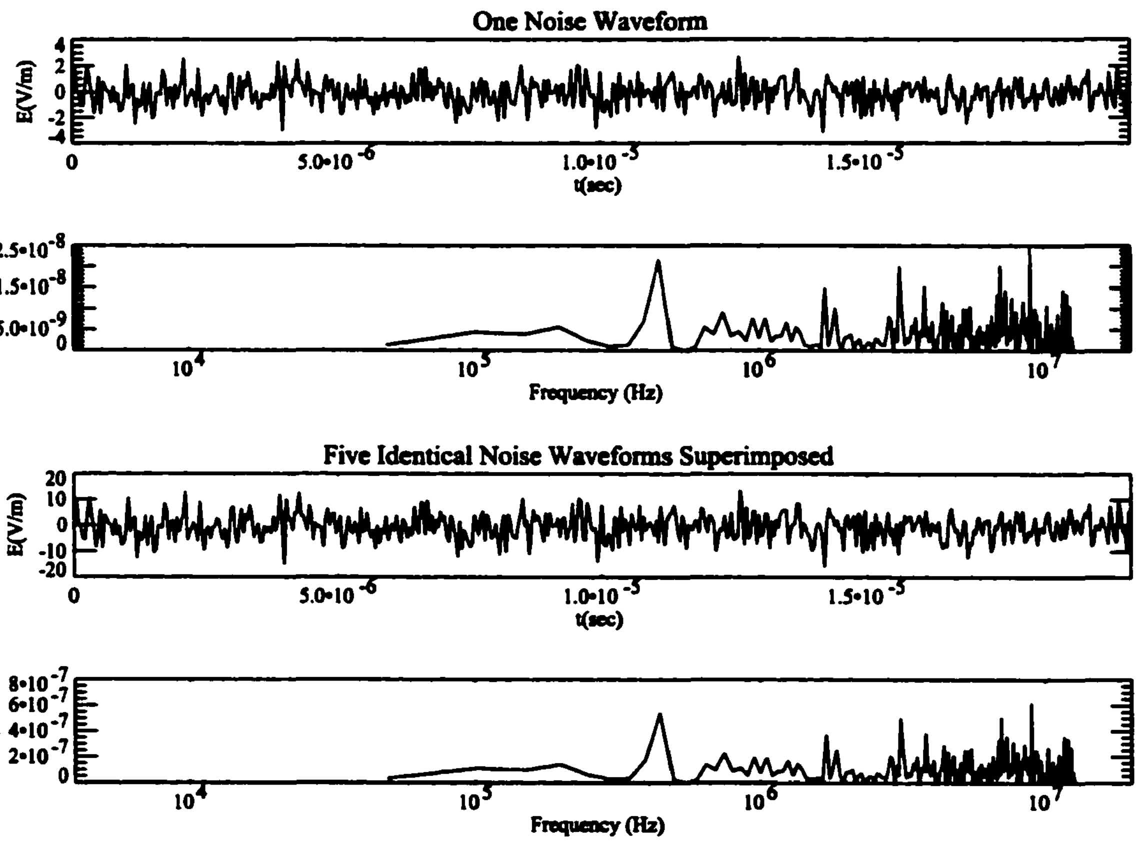

Figure 1.4. Top Plot: Waveform with random temporal phase. Second Plot: Power spectral density per unit area. Third Plot: Same waveform as top plot multiplied by N=5. Fourth Plot: PSD per unit area for third plot. Note that the two spectra have the same shape, but the amplitudes differ by a factor of N^2= 25.

For comparison consider the effect of amplifying the electric-field waveform from this noise source by a factor of N=5. This is equivalent to considering a case where 5 identical noise signals exactly interfere constructively. One might imagine a noise source of the same geometrical shape and current phase as whatever source produced the N=1 waveform, but with five times the *dI/dt* amplitude. The energy spectral density per unit area will be a factor of N^2=25 (bottom plot Fig.1.4) larger than that for the waveform shown in the top plot of Figure 1.4. Usually, noisy signals are said to be "totally incoherent" because of the randomly received phase. However, the above example is used to illustrate phase correlation in a mathematical sense whether the signal is noise-like or smooth.

For contrast consider having N=5 separate noise sources that produce electric fields that will have random phase at the receiver. The energy spectral density in this case will increase by only a factor of N over the single-source case. Note that the calculated factor is 4.76 and not exactly 5. These plots are shown in Figure 1.5. The waveforms and spectra of Fig. 1.4 and Fig. 1.5 are noisy because the amplitude of each received sample of the electric field does not vary smoothly with neighboring values of the recorded electric field. The amplitude as a function of time and the amplitude as a function of frequency appear random.

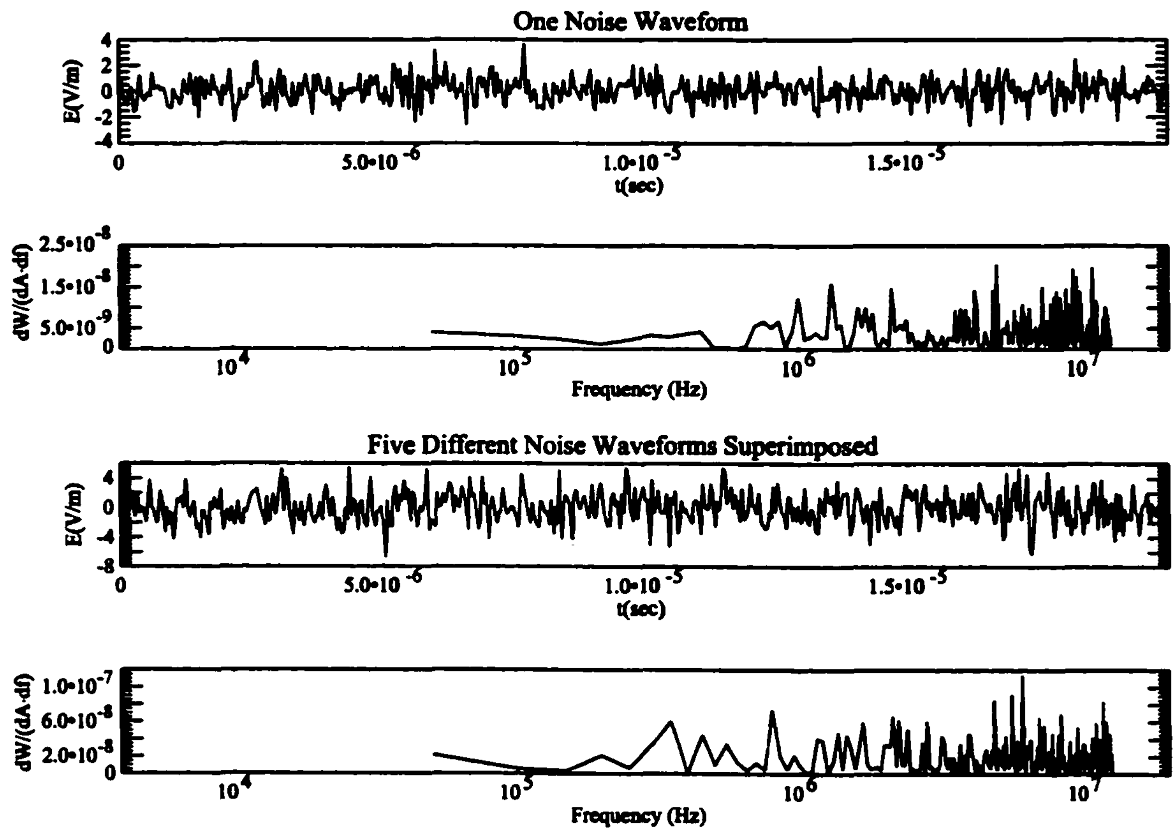

Figure 1.5. Top Plot: Waveform with random temporal phase. Second Plot: Power spectral density per unit area. Third Plot: Five different waveforms with random temporal phase (includes waveform shown in top plot). Fourth Plot: PSD per unit area for third plot. Note that the two spectra have the same shape, but the amplitudes differ by a factor of about $N = 5$.

The previous discussion on phase correlation for noisy signals also applies for smooth waveforms. If N signals are phase correlated, and have the same electric field amplitude, the power will be N^2 times that of one signal. If they are not, it will be roughly N times the power of one signal. For sources and signals with smoothly varying phase the amplitude variations in the time and frequency domains do not appear random but change gradually.

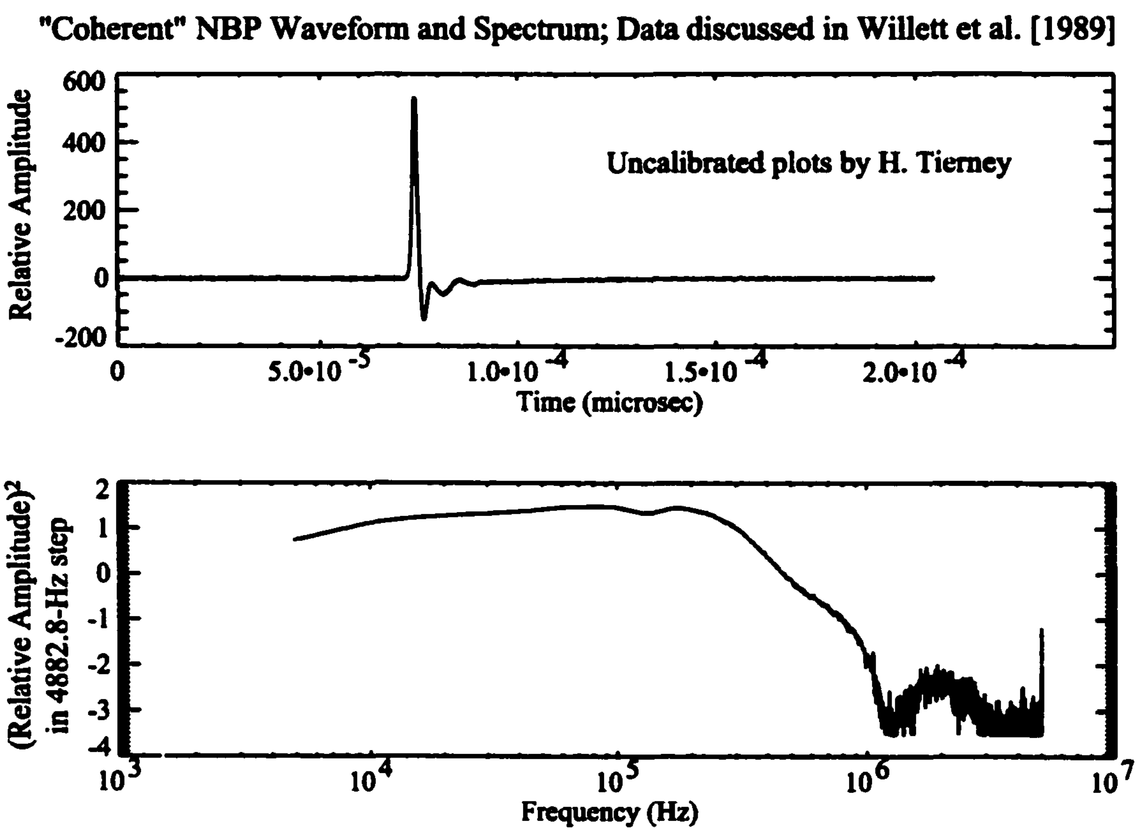

Figure 1.6. Top Plot: Uncalibrated narrow positive bipolar pulse waveform recorded by Willett *et al.* [1989]. Bottom Plot: Spectral amplitude is smooth, "coherent" for low frequencies with noise of relatively low amplitude above about 1 MHz.

Signals with a fast rise time and a relatively slow decay will often have a spectrum that represents the rise time of the pulse with the highest frequency bin of the associated spectrum. For this situation, the lower frequency bins represent the decay of the pulse. A relatively smooth signal, with low amplitude noise superimposed on it, is shown in Figure 1.6. This plot is shown for comparison with the noise-like signals only and has not been calibrated.

There are two points from this discussion that are relevant to the present study. First, an increase in the number of noise radiators in a region of space by a factor of N will increase the power received by approximately a factor of N. It is unlikely that such noise sources will arrive at a receiver in phase. If a coherent source increases by a factor of N the average radiated power increases by a factor of N^2. This seems to imply that a smooth current change with a short rise time may be producing the intense VHF radiation. However, some of the data show spectra that resemble noise waveforms.

1.1.4 Polarization

The degree of polarization for an electromagnetic field can also give insight into the source of the radiation. Polarization is discussed in many text books including [*Budden*, 1988; *Jackson*, 1975; *Rybicki and Lightman*, 1979]. For a plane wave, the electric and magnetic field vectors are perpendicular to the propagation vector at all times. For a linearly polarized wave, the electric-field vector oscillates along a line. This line and the propagation vector lie in, and define, the plane of polarization. Perhaps the most common way to describe a time-varying electric field is in terms of two mutually orthogonal components. The two components will oscillate along their respective coordinate axes. For a linearly polarized wave, these two components will oscillate in phase.

Consider the superposition of two linearly polarized plane waves that lie along orthogonal coordinates **x** and **y**. If these two plane waves are 90-degrees out of phase the resultant vector is said to be circularly polarized. In the following equations, the amplitude E_o is not time dependent. For a fixed value of z, e.g. 0, the set of points defined by $[E_x, E_y]$ trace out a circle in time.

$$E_x = E_o \cos(kz - \omega t) \tag{1.12}$$

$$E_y = -E_o \sin(kz - \omega t) \tag{1.13}$$

In this example, the net electric field vector rotates counterclockwise and is often called a left circularly polarized wave. If the two components have different amplitudes and phases, the wave is said to be "elliptically polarized" because the net vector will trace out an ellipse in time. If the amplitude variations of the electric-field vector are smooth and are consistent with elliptical polarization then the signal will have a high degree of polarization, as calculated using Stoke's parameters. Furthermore, the degree of polarization of a signal can give clues about the radiating source. For example, if a highly-polarized signal is observed, the radiating particles are, primarily, accelerating or have motion in the same direction.

Under the assumptions made for a model runaway electron avalanche in Chapter 4, the radiation will be completely polarized. Note that in the case of the relativistic electron avalanche the high-energy electrons are characterized by a mean energy and the radiation is a result of the growing number of radiators in time through ionization. Perfect polarization will not be present from a real electron avalanche. Motions of the individual electrons will be influenced by the electric and magnetic forces acting on them. The signals radiated as a result of accelerations of the individual electrons will add a partially unpolarized component to the radiated signal.

Recently it was shown, for a study of 313 TIPPs, that 225 have calculated degrees of polarization that are higher than 0.8, 1.0 being complete polarization [*Shao and Jacobson*, 2001]. These authors concluded that "the breakdown processes that produce the VHF radiation are highly organized." The TIPP events are discussed in detail in Chapter 2. This information, coupled with the fact that a relativistic electron avalanche will produce highly-polarized radiation, also encourages the consideration of a runaway electron avalanche as a source for the impulsive VHF signals.

1.2 Summary of Following Chapters

As part of the background section of this thesis, observations of the NBPs and time-correlated VHF transients are discussed in Chapter 2. Also in Chapter 2, background information is presented for runaway breakdown theory, which is the foundation of the present work. A runaway electron avalanche is considered as a source of the transient VHF signals because the time for an avalanche to develop over a spatial scale corresponding to the distance between charged regions of a thunderstorm is on the order of microseconds. These events are also believed to produce powerful radio-frequency radiation and it is the goal of this work to quantify the angular distribution of the radiated power for this hypothesized source and compare it with observations. The consideration of runaway breakdown model is also validated because runaway breakdown theory has been successful in reproducing observations of enhancements in X-ray counts measured during thunderstorms [*Roussel-Dupré et al.*, 1994].

Chapter 3 discusses the "state of the art." Because the goal is to compare a model of the VHF radiation from a runaway avalanche with observations of NBPs and TIPPs, the existing models of VHF radiation from lightning are discussed. Though progress has been made in understanding the sources of VHF radiation from lightning, the existing models often apply to a specific lightning phenomenon other than that described above. Models of the source physics, including physical reasoning applied to the variations of the ionic species as a function of space and time, and the accompanying radiation are scarce. One semi-empirical model [*Bondiou et al.*, 1987] that has gained credibility among lightning scientists as an explanation for the VHF radiation is reviewed. In addition, an analytic model of radio emissions produced by a point charge runaway electron avalanche is presented [*Roussel-Dupré and Gurevich*, 1996].

In Chapter 4 (and Appendix A), a numerical method for calculating radiation electric fields in the VHF range is presented. This routine was developed for use in investigating whether the relativistic electron avalanche might reproduce radio observations of NBPs and VHF transients. It is demonstrated that the numerical calculation of the peak electric field as a function of observer angle is in agreement with the analytic result of *Roussel-Dupré and Gurevich*, [1996]. A 1-D model of an electron avalanche evolving within a spatially varying electric field is then considered as a source. The production rates of the high-energy (primary) and low-energy (secondary) electron species are dependent upon the ambient electric field and pressure. The results from an electron avalanche occurring within a thunderstorm, for which ±30-C spheres are used to model the positive and negative charge regions, are shown to be in agreement with observations of peak electric fields for NBPs and the spectral intensity of the corresponding VHF impulses. However, this is only true for a limited observation angle range. This is discussed in Chapter 5, and the results from three model thunderstorms are presented. Chapter 6 outlines the primary conclusions, addresses some further points of discussion and suggests directions for future research.

Chapter 2

Background

2.1 Observations

Radiation at meter wavelengths is observed in conjunction with many lightning processes including preliminary breakdown [*Beasley et al.*, 1982], stepped and dart leaders, attachment, and return strokes for cloud to ground flashes. In addition VHF radiation is used to map the development of lightning within clouds where the optical radiation is scattered, and the visual details of the discharge are therefore obscured. For further information see: *Hayenga and Warwick* [1981], *Krehbiel et al.* [1999], *Mazur et al.* [1995], *Oetzel and Pierce* [1969b], *Proctor* [1981], *Proctor et al.* [1988], *Rhodes et al.* [1994] and *Shao et al.* [1996a]. The NBP and associated VHF signals form a distinct class of lightning-related electric-field waveforms [*Smith*, 1998]. For the NBP signals the magnitude of the peak electric field is comparable to that measured for return strokes. Observations of the NBPs, the HF/VHF radiation accompanying NBPs, and the satellite-observed signals known as TIPPs are reviewed in section 2.1.

2.1.1 Ground-Based Observations of NBPs

In a quest to find the sources of the strongest HF (3-30 MHz) and VHF radiation (30-300 MHz) in thunderstorms [*Le Vine*, 1980] used a "very high" threshold to trigger an electric-field waveform recorder with a 20-MHz sample rate. The RF system included several channels between 3 and 300 MHz, each with 300-kHz bandwidth. The VHF pulses strong enough to trigger this instrument were accompanied by electric-field pulses with 10 to 20-μs duration and a characteristic shape. The peaks of these waveforms were followed by overshoots of the opposite polarity (hence bipolar). In this study, the polarities of the observed waveforms were consistent with negative charge moving upward for a dipole radiator. It was concluded that the bipolar pulses have characteristics similar to K-changes, but are of much shorter duration. A "K-change" is conceptualized as a small return-stroke-like event or "recoil streamer" occurring within a cloud [*Uman*, 1987]. A transmission line model developed by *Le Vine and Meneghini* [1978] was used to show that a 1-km recoil streamer with a phase speed of c/3 could reproduce the bipolar pulse. No attempt was made to model the strong VHF radiation in this paper. The NBP model is briefly discussed in Chapter 3.

Further observations of narrow bipolar and VHF pulses were made by *Willett et al.* [1989]. It was found that the NBPs were not associated with K changes, but they were also not attributable to any other process. They write: "Since we do not know the location, either in space within the storm or in time relative to any other familiar lightning process, of the sources of these peculiar pulses, it is perhaps premature to speculate on their nature." However, these investigators do agree with *Le Vine* [1980] that the pulses are relatively isolated, within 1-ms data recordings, and can occur before or after a return stroke in a cloud-to-ground flash. For a storm at known range, statistical and spectral analyses were performed on 18 narrow positive bipolar pulse (NPBP) waveforms and were compared to 50 first return strokes. The work of *Willett et al.* [1989] is summarized in the following three figures. Figure 2.1 shows an example of one of the positive NBPs (top: E [V/m]) and the associated HF-VHF radiation (bottom: dE/dt [V/(m·μs)]). The frequency response (half-power points) of the electric-field (*E*) data is about 160 Hz - 3 MHz. The (*dE/dt*) data has bandwidth of approximately 30 MHz.

In Figure 2.1 the top plot, showing a narrow bipolar pulse, has an electric-field amplitude that varies smoothly in time. The *dE/dt* waveform (bottom plot of Figure 2.1) exhibits relatively strong noise in addition to the appropriate sign for the expected field change of the corresponding *E* waveform. The HF-VHF radiation noise appears to be strongest at the time of the first positive portion of the NBP. For comparison, Figure 2.2 shows the electric-field (*E*) waveform and associated HF-VHF radiation for a return stroke occurring in the same storm as the NBP of Figure 2.1. In Figure 2.2, the magnitude of the peak amplitude of the return-stroke electric field is about the same as that of the NBP. However, the duration of the return-stroke waveform is greater. Note that in the "physics convention" the negative electric field indicates that negative charge is being transferred downward. The bottom plot showing the time-derivative of the return stroke signal exhibits much less HF-VHF noise than the NBP. Figure 2.3 shows that, overall, the energy spectral density (ESD) of NBPs (solid curve) is greater than that for return strokes (dashed curve) for frequencies of 8 MHz and above. The ESD in this figure has been normalized to a 50-km range, and zero dB corresponds to $1(V/m/Hz)^2$. This spectrum is believed to be reliable from 200 kHz to about 20 MHz. At 18 MHz, the energy spectral density of the radiation from the narrow bipolar pulses is about 16 dB above that from the return strokes. The spike at 25 MHz is present in all of the data (personal communication). These authors conclude: "it would appear that NPBPs are the largest producers identified to date of electromagnetic radiation from lightning in the upper HF band and perhaps beyond."

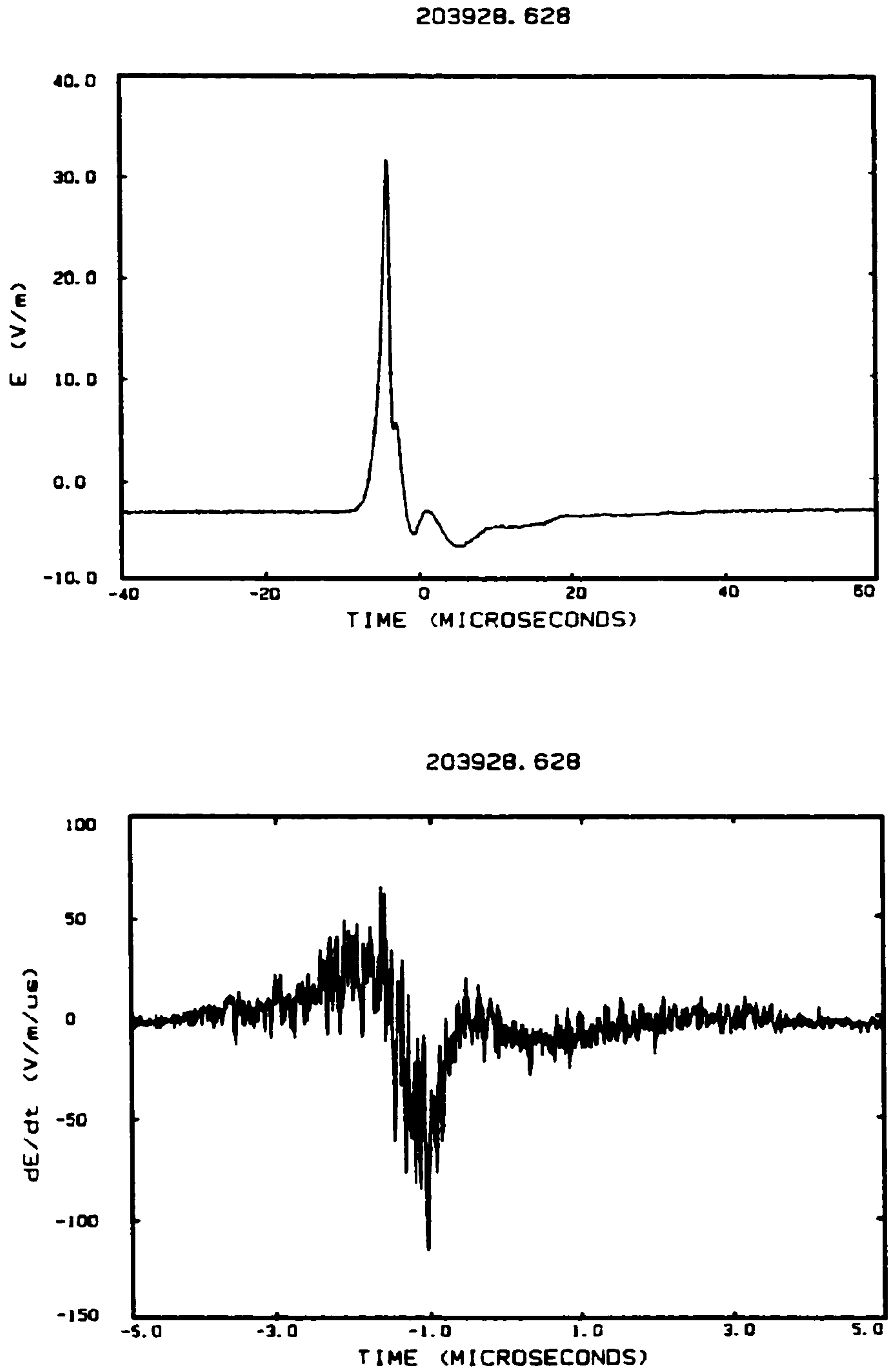

Figure 2.1 Electric field and field-derivative waveforms of a narrow positive bipolar pulse (NPBP) recorded by *Willett et al.* [1989]. The polarity of the electric field waveform seems to indicate that negative charge is moving upward. The large amplitude noise shown in the dE/dt waveform is characteristic of this type of lightning event. (*Willett et al.* [1989], Copyright 1989 American Geophysical Union. Reproduced/modified by permission of American Geophysical Union.)

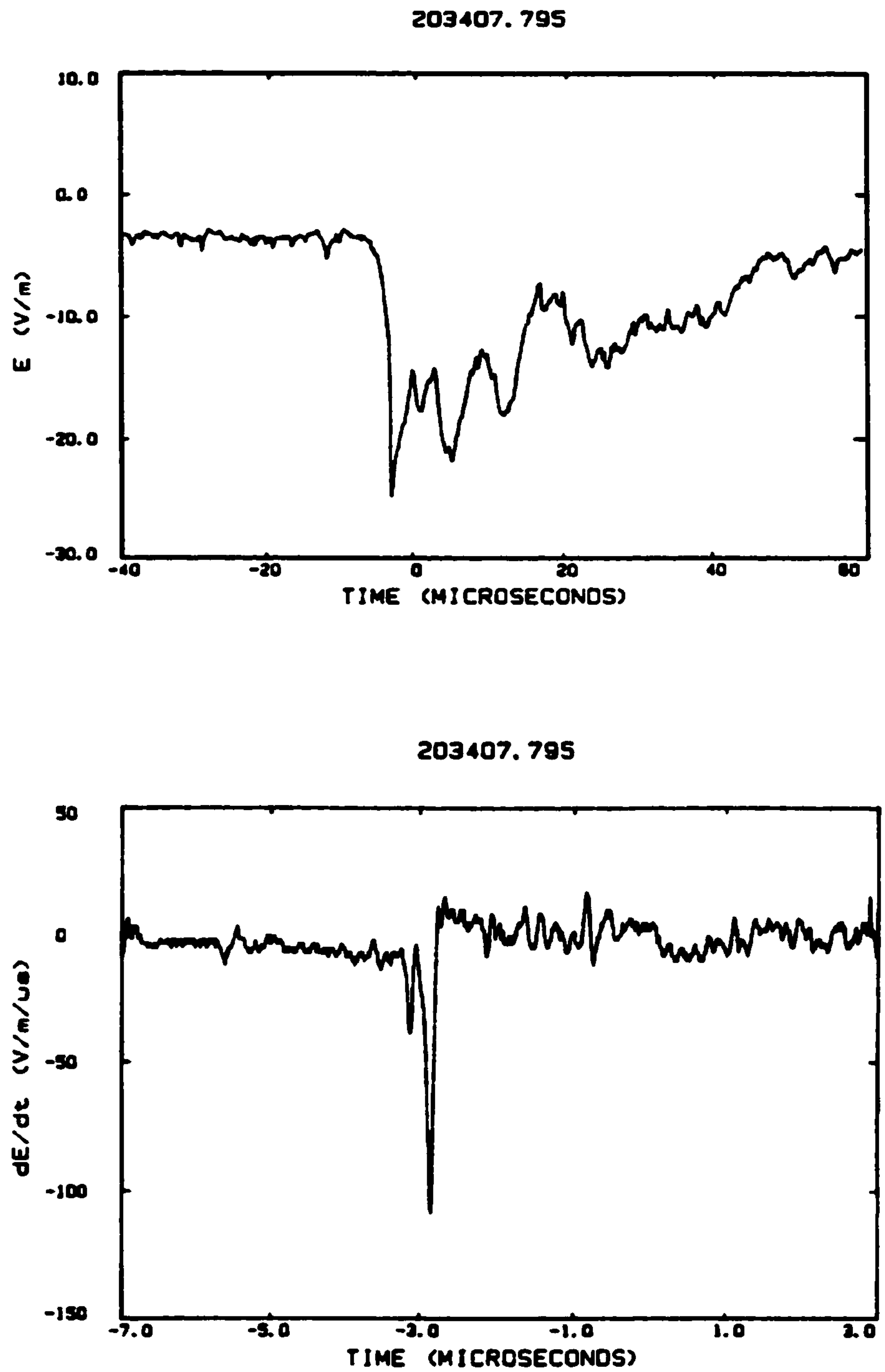

Figure 2.2 Electric field and field-derivative waveforms of a return stroke lowering negative charge to ground recorded by *Willett et al.*[1989]. The magnitude of the electric-field waveform is comparable to that of the NPBP of Figure 2.1. In contrast with the NPBP dE/dt waveform there is a relatively low amount of high frequency noise. (*Willett et al.*[1989], Copyright 1989 American Geophysical Union. Reproduced/modified by permission of American Geophysical Union.)

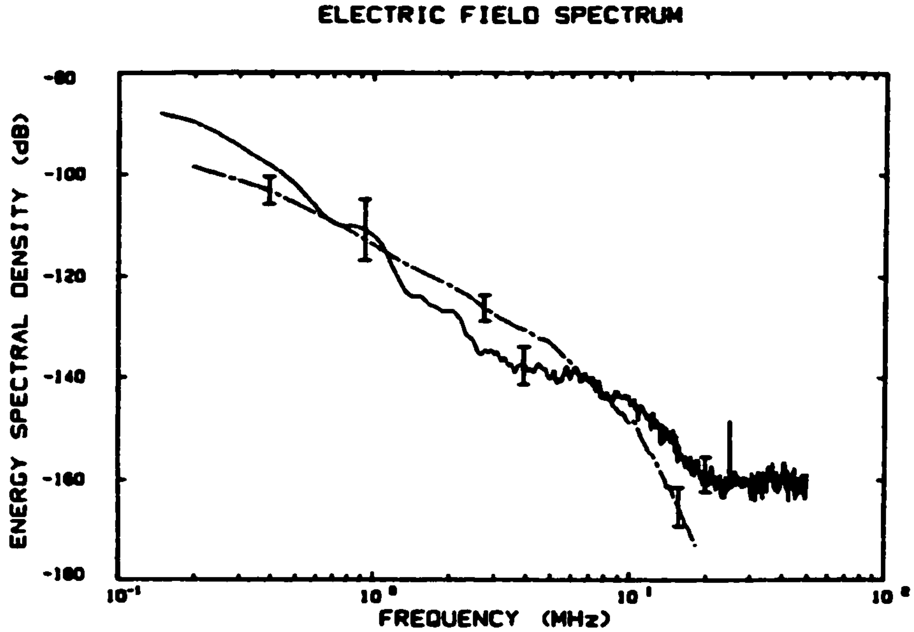

Figure 2.3 Average total energy spectral density (ESD) for 18 NPBP events (solid curve) and 50 first return strokes (dot-dashed curve) recorded by *Willett et al.* [1989]. The reference level for the decibel conversion is 1 $(V/m/Hz)^2$. The error bars show the standard deviation about the average. Above about 8 MHz, the ESD is largest for the NPBP events. (*Willett et al.* [1989], Copyright 1989 American Geophysical Union. Reproduced/modified by permission of American Geophysical Union.)

A study of 24 NBPs occurring in southwestern thunderstorms during the summer of 1996 was performed by *Smith* [1998]. This author estimated the source heights of the 24 NBPs to be between 8 and 11 km MSL. The NPBPs recorded by *Smith* [1998] had average range-normalized peak amplitudes 9.9 times greater than return strokes from the same storms and 29 times greater than any portion of any intracloud discharge. In addition, the radiation in the HF range was 20 dB higher than radiation from other types of lightning discharges. The HF noise bursts, recorded in the frequency range of 3-25 MHz, occurred during the first half-cycle of the NBP waveforms. These observations lead *Smith* [1998] to believe that the HF energy is from an unusually strong breakdown process. The bipolar waveform with period of roughly 20 μs was hypothesized to be radiated by a charge transfer, or current, process. The dipole moments, charge transferred, and lengths of the current processes producing the NBP waveforms were also estimated as explained in Chapter 3.

Investigators at the Langmuir Laboratory for Atmospheric Research use VHF radio receivers with passbands of 60-66 MHz to map lightning activity. Their system is a deployable array that gives a three-dimensional and temporal picture of lightning development [*Rison et al.*, 1999]. Each station records the most intense signals within 100-μs time windows. Many such signals are recorded for each cloud-to-ground or intracloud discharge. In a recent report on the source powers of these data [*Thomas et al.*, 2001] it was found that signals with power of about 1 W or more are often detected and locatable; typical observations are in the 10-30-kW range. Above about 100 W, the number distribution of events falls off as the inverse of the power. These authors also report the observation of a bipolar event with a peak power in excess of 300 kW. This was the "initial radiation source" of an intracloud discharge discussed in *Thomas et al.* [2001]. It also is mentioned that the strongest VHF sources are located near the positive charge regions of thunderstorms. The source-power range of 1W-30 kW is scaled to a 10-km range and 1-kHz bandwidth, converted to electric-field units of μV/m, and plotted for comparison with other measurements in Figure 2.8.

2.1.2 Space-Based Observations: TIPPs

The study of lightning using satellite-based VHF receivers at LANL has recently been of interest in part because of the plethora of transionospheric pulse pairs observed in association with lightning activity. TIPPs were first observed in 1993 with a VHF receiver, called Blackbeard, onboard the ALEXIS (Array of Low Energy X-ray Imaging

Sensors) satellite [*Holden et al.*, 1995]. TIPPs are distinguished from other naturally occurring radio emissions by several features [*Massey and Holden*, 1995]. Using Blackbeard, TIPPs were found to consist of exactly two broadband (25-100 MHz) pulses that exhibit dispersion caused by propagation through the Earth's ionosphere. The duration of each pulse is a few microseconds and the time separation of the pulses is typically tens of microseconds. The ionosphere acts as a high-pass dispersive filter for lightning electromagnetic pulses such that frequency components of signals that are lower than about 20 MHz are effectively reflected toward Earth. Higher frequency components of VHF radio signals arrive first at a space-based receiver. To first order, the frequency cutoff depends on the time of day, latitude, and other factors. The amount of temporal dispersion depends on the total electron content (TEC) of the ionosphere which has units of #electrons/m^2 and is the path integral of the electron density along the line of sight.

Using Blackbeard, the peak power of either pulse in a TIPP was found to be stronger than the peak VHF power of return strokes from cloud-to-ground (CG) lightning. However, the triggering mechanism of Blackbeard requires only that the instantaneous power within a 75-MHz bandwidth reach a selected level. With this triggering scheme, it was necessary to set the triggering power level high in order to avoid triggering by narrow band signals. As a result, only the very high-power VHF signals were recorded and TIPPs became the primary focus of lightning studies using that instrument.

A second satellite carrying optical and RF instruments, FORTE, was launched on August 29,1997. FORTE carries two RF receivers, both of which are described in detail in *Jacobson et al.* [1999]. One of these receivers has two passbands; each is independently tunable in the range of 20-300 MHz with 22-MHz effective bandwidth. For the data reported here, the observations were made over a 26-48 MHz band. Both of the passbands have eight subbands of 1-MHz bandwidth that trigger independently. This design was implemented so that the receiver would trigger off of wideband signals and discriminate against carriers [*Enemark and Shipley*, 1994]. The trigger threshold for each subband can be set at a fixed level, or at a selected dB level above the noise background. For a signal to be recorded it is typically required that 5 out of 8 of the subbands trigger within a several-microsecond coincidence window. Using this triggering scheme, a variety of broadband VHF signals from lightning, including TIPPs, have been recorded. The TIPPs recorded by FORTE cover a wider energy range than those recorded by Blackbeard. An example of a TIPP periodogram is shown in Figure 2.4.

FORTE has recorded millions of lightning-related events. These measurements have been placed in the context of other lightning observations through time correlation with events located by the National Lightning Detection Network (NLDN). Recent studies have shown that many of the LF/VLF waveforms of lightning return strokes and cloud pulses observed by the NLDN correlate in time with VHF signals observed by FORTE. For example, optical and VHF signals recorded by FORTE that are time-coincident with type-classified NLDN waveforms have been analyzed by *Suszcynsky et al.* [1999]. With better than 90% confidence, these authors were able to distinguish between the NLDN designations of return stroke, subsequent return stroke, and intra-cloud discharge based on the satellite-recorded VHF signature.

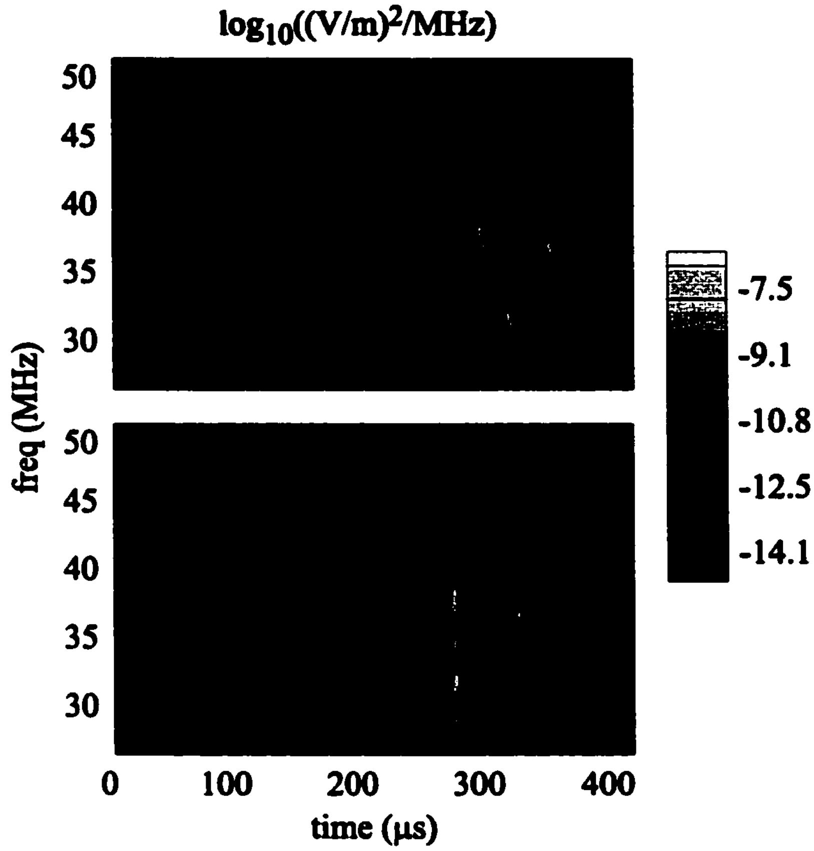

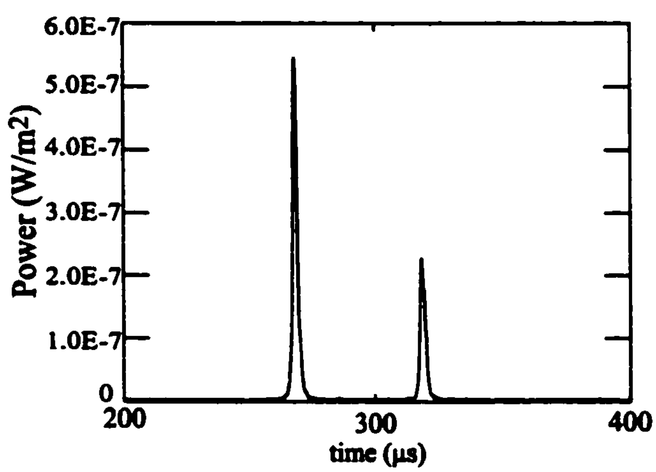

Figure 2.4 Example of a FORTE VHF periodogram of a TIPP. In the top plot ionospheric dispersion is evident for both pulses of the TIPP. The second plot has been corrected for dispersion. The spectral components of the TIPP signal are relatively intense across the entire frequency range. The response of the receiver rolls off at about 48 MHz. The bottom plot shows the total intensity in the 22-MHz band as a function of time.

Time coincidences between the LF/VLF field signals recorded by the NLDN and lightning signals recorded by other systems, which do not independently classify data recordings, have been used to correlate types of lightning discharges with the recorded waveforms. Standard, quality-controlled NLDN data provide locations of cloud-to-ground lightning strike points for flashes that occur within 625 km of the nearest participating NLDN station. The overall detection efficiency for first return strokes and subsequent return strokes is about 80 to 90 percent. For this standard data set, return stroke events with peak currents exceeding 5 kA are located with a median accuracy of 500 m [*Cummins et al.*, 1998]. Events classified as positive CG strokes with peak currents less than 10-kA may be misidentified cloud pulses [*Jacobson et al.*, 1999].

The NLDN data discussed here were obtained with waveform discrimination criteria that were "relaxed", that is, less stringent than normal NLDN data. This allowed for more time coincidences with FORTE observations than was possible using only the standard data. In addition to the standard data, this data set provides locations for energetic cloud discharges occurring within or near the network, distant CG discharges, and discharges that are not type classified [*Jacobson et al.*, 1999]. Locations reported for the relaxed-criteria data are less accurate than those for the standard data. Events classified as cloud discharges have a location accuracy of better than 3 km [*Jacobson et al.*, 1999]. Any impulsive waveform with a peak-to-zero time of less than 10 μs is classified as a cloud discharge. Lightning discharges occurring 2000-4000 km outside of the U.S. have an error of 16-32 km in their assigned NLDN coordinates [*Cramer and Cummins*, 1999]. Peak currents of discharges with sources greater than 625 km beyond the nearest participating NLDN station were set to zero, and thus are not type classified. Beyond this range, the ionospheric reflection of the sky wave can be stronger than the ground wave and hence, source strength estimates based on ground wave propagation may not be valid. The relaxed criterion data set also contains numerous "outlier" events, which have location errors of greater than or equal to 50 km [*Jacobson et al.*, 1999].

The peak source powers of signals recorded by FORTE were calculated by *Jacobson et al.* [2000]. The sources were assumed to be isotropic radiators, meaning that the power per unit area is independent of angle. The power was summed over the 22-MHz band covering 26-48 MHz as shown in the bottom plot of Figure 2.4. Since most signals originate within a 1000-3000 km range from the satellite, a 2000-km range was assumed to obtain these source powers. The VHF data records were also assigned to lightning types based on their time correlation with classified signals received by the NLDN. This result is shown in Figure 2.5. The most powerful VHF events were found to be associated with the intracloud, "C", discharges. The satellite observations that were time correlated with events designated as "intracloud" by the NLDN contained the highest percentage of TIPPs. The peak in the source-power histogram for these events is near 100 kW.

Other authors have used time correlation analysis to investigate the sources of TIPPs. TIPPs were found to correlate in time with LF/VLF intracloud pulses observed by the NLDN [*Jacobson et al.*, 1999; *Zuelsdorf et al.*, 1998]. *Cummins et al.* [1998] report that some of the relatively intense, longer-duration intracloud discharge events may be the same class of event as that which includes the isolated, positive bipolar pulses identified by *Weidman and Krider* [1979]. Because the narrow bipolar pulses are accompanied by intense noise-like bursts of radiation in the HF and VHF ranges [*Le Vine*, 1980; *Willett et* *al.*, 1989], it has been suggested that some of these events are the source of the first pulse of a TIPP [*Smith*, 1998].

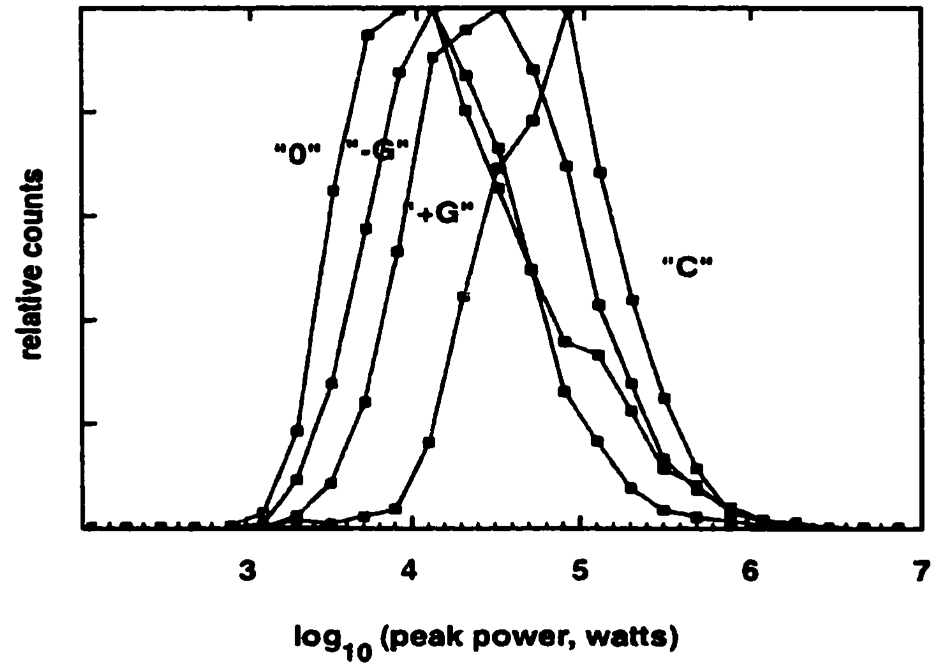

Figure 2.5 FORTE VHF peak power histograms for data that were time correlated with discharges that were identified by the NLDN as unclassified (0), negative/positive cloud-to-ground (-G/+G), and intracloud (C). (*Jacobson et al.* [2000], Copyright 2000 American Geophysical Union. Reproduced/modified by permission of American Geophysical Union.)

Since the initial recordings of TIPPs, some evidence has supported the hypothesis that the two pulses of the pair are the direct and ground-reflected signals from a thunderstorm source [*Holden et al.*, 1995; *Jacobson et al.*, 1999; *Massey and Holden*, 1995; *Massey et al.*, 1998; *Smith*, 1998; *Tierney et al.*, 2002]. A model in which two temporally linked VHF sources of thunderstorm origin are responsible for the production of TIPPs was also presented [*Roussel-Dupré and Gurevich*, 1996]. In this model the first pulse is attributed to the onset of an electron avalanche in a thunderstorm. The source of the second pulse radiates tens of kilometers above the thunderstorm. The time separation of the two pulses in this theory is the time for the electromagnetic disturbance to travel between the low and high-altitude regions of maximum VHF production. For a vertical discharge, this time delay is a maximum for a satellite viewing the emissions from the horizon. A satellite directly above the radio emissions would observe the two maxima of emission almost simultaneously because the electrons are moving near the speed of light.

This relationship between the satellite observation angle and TIPP separation, advanced by the previous result, was later shown to be inconsistent with most of the TIPP data. As shown in *Jacobson et al.* [1999], for the majority of TIPPs, the time separation of the two pulses is a minimum for a low satellite observation angle and a maximum when the satellite is near the zenith with respect to the thunderstorm. This finding led TIPP investigators to believe that the second pulse of a TIPP is the result of a surface reflection. This result, however, does not preclude the occurrence of runaway breakdown in any discharge at high or low altitudes. The implications for directed radiation are important and will be discussed in Chapters 5 and 6.

Despite this evidence, the surface-reflection hypothesis has been questioned recently. One objection has been that the reflectivity of land may not be high enough to explain the large percentage of events in which the second pulse is as intense or more intense than the first [*Rodger*, 1999]. To address this *Tierney et al.* [2002] calculated the pulse energy ratios for TIPPs occurring over land and water. The energy in the "ground-reflected" pulse is divided by the energy in the pulse that takes a direct path to the satellite. The TIPPs were previously located by using time-coincidence locations given by the National Lightning Detection Network (NLDN). Discrete storms were identified using plots of measured total electron content of the ionosphere vs. time [*Tierney et al.*, 2001]. A total of 65 storms and a total of 2467 TIPP events were assigned locations over land, water, and coastal regions. Figure 2.6 shows the pulse energy ratios for TIPPs occurring within these storms, parsed by the type of underlying reflection surface.

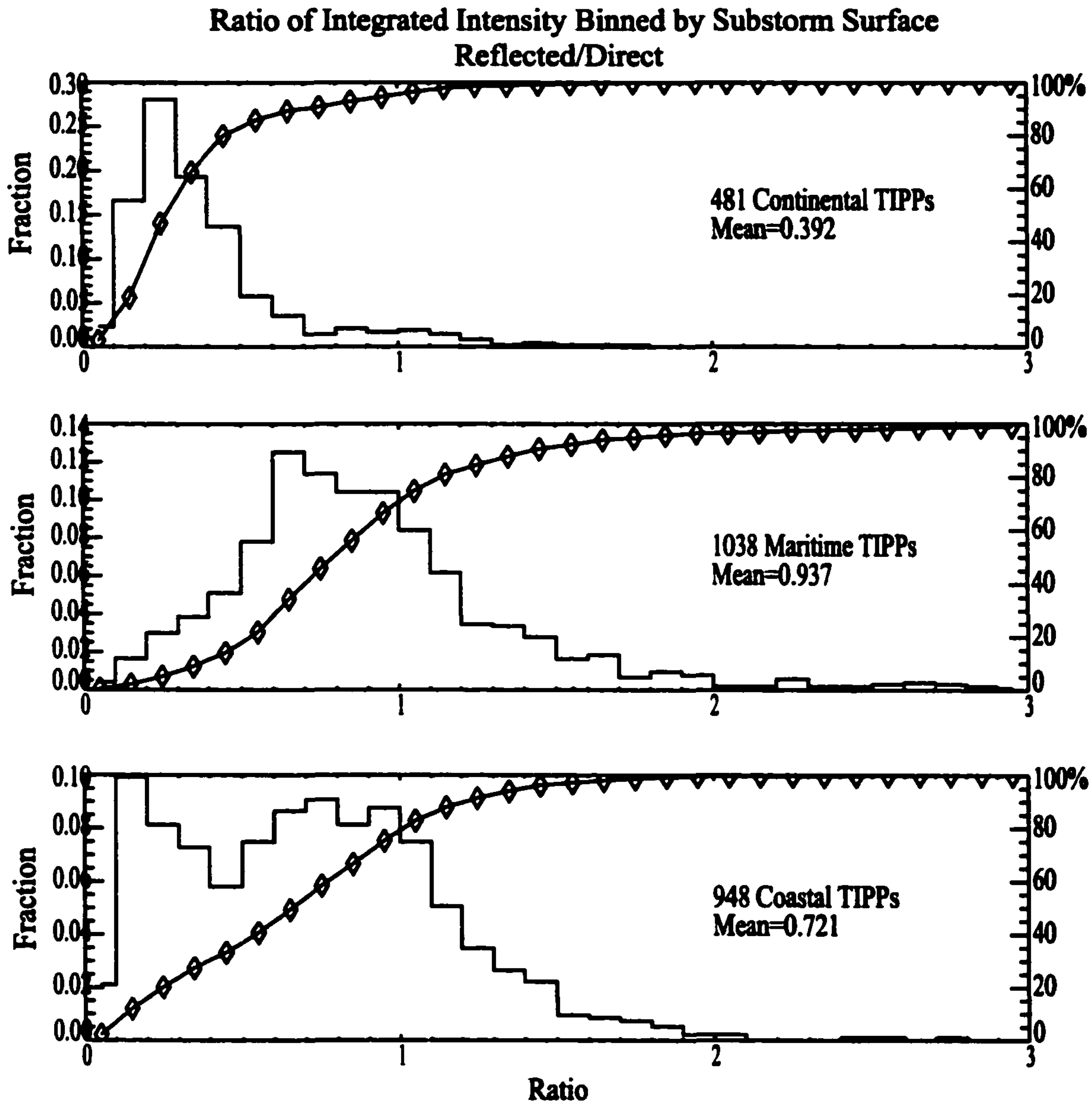

Figure 2.6 Pulse energy ratios for TIPPs occurring over continental, maritime, and coastal regions. (*Tierney et al.* [2002], Copyright 2002 American Geophysical Union. Reproduced/modified by permission of American Geophysical Union.)

The ratio of the reflected to incident energy is equal to the square of the magnitude of the reflection coefficient. The Fresnel equations give the reflection coefficients for the horizontal-plane and vertical-plane polarization of an electromagnetic (EM) wave, R_H and R_V. In the following equations the horizontal component of an EM field vector is perpendicular to the propagation vector and lies in the plane of the reflecting surface. The vertical component is perpendicular to both the propagation vector and the horizontal component of the EM field vector.

$$R_H = \frac{\sin\alpha - (K - \cos^2\alpha)^{1/2}}{\sin\alpha + (K - \cos^2\alpha)^{1/2}} \tag{2.1}$$

$$R_V = \frac{K\sin\alpha - (K - \cos^2\alpha)^{1/2}}{K\sin\alpha + (K - \cos^2\alpha)^{1/2}} \tag{2.2}$$

Above, K is the complex dielectric constant. The incident angle measured from the reflecting surface is α. The dielectric constant can be expressed in terms of its real and imaginary components.

$$K(\omega) = K'(\omega) - iK''(\omega) \tag{2.3}$$

K' is the ratio of the dielectric permittivity, ε, of a medium to the permittivity of free space, ε_o. The imaginary component is inversely proportional to the frequency, ω, and proportional to the electrical conductivity, σ, of the reflecting surface.

$$K'' = \frac{\sigma}{\omega\varepsilon_o}\ . \tag{2.4}$$

The TIPPs analyzed here were recorded using a 26 to 48-MHz frequency range, and the corresponding wavelength range is about 11 to 8.25 m. The real and imaginary parts of the dielectric constant for oven-dry and water adsorbed soils in the frequency range of 30 MHz to 3 GHz have been measured by *Saarenketo* [1998]. For the dry and wet soil, the measured average values of the dielectric constant in the range of 30 to 50 MHz are used in Eqs (2.1) and (2.2). For seawater the results from a study of water salinity using 30-MHz radar by *Kachan and Pimenov* [1997] are used. Figure 2.7 shows that the expected reflection coefficients squared for land and seawater are in agreement with the pulse energy ratios calculated from the satellite data. Because the Fresnel equations apply to a polarized source, this agreement suggests that many of the signals called TIPPs have a high degree of polarization. Based on the above results it also is believed that, for the events called TIPPs, significant ground-directed and satellite-directed radiation in the VHF range is required of a successful model.

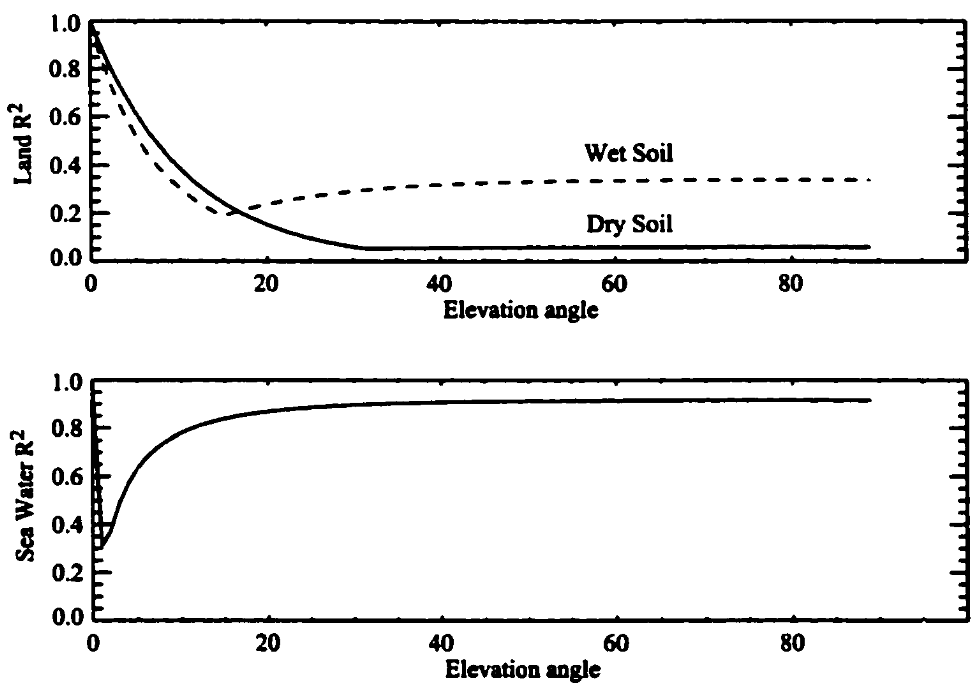

Figure 2.7 Squared reflection coefficients for wet and dry land, and sea water.

2.1.3 Comparison with Pierce Curve

Measurements of electric-field amplitudes from various lightning processes, by different investigators, have been scaled to a 10-km observation range and a 1-kHz bandwidth [*Oetzel and Pierce*, 1969a]. The overall amplitude variation with frequency follows a *1/f* behavior, but there are substantial deviations above about 10 MHz [*Pierce*, 1977]. The individual measurements are included as data points on the plot in this reference but are excluded from Figure 2.8. These observations were made with receivers of varying bandwidth, so no information is provided about the spectra of the received signals. The data follow the *1/f* curve, which is plotted for comparison as a straight line.

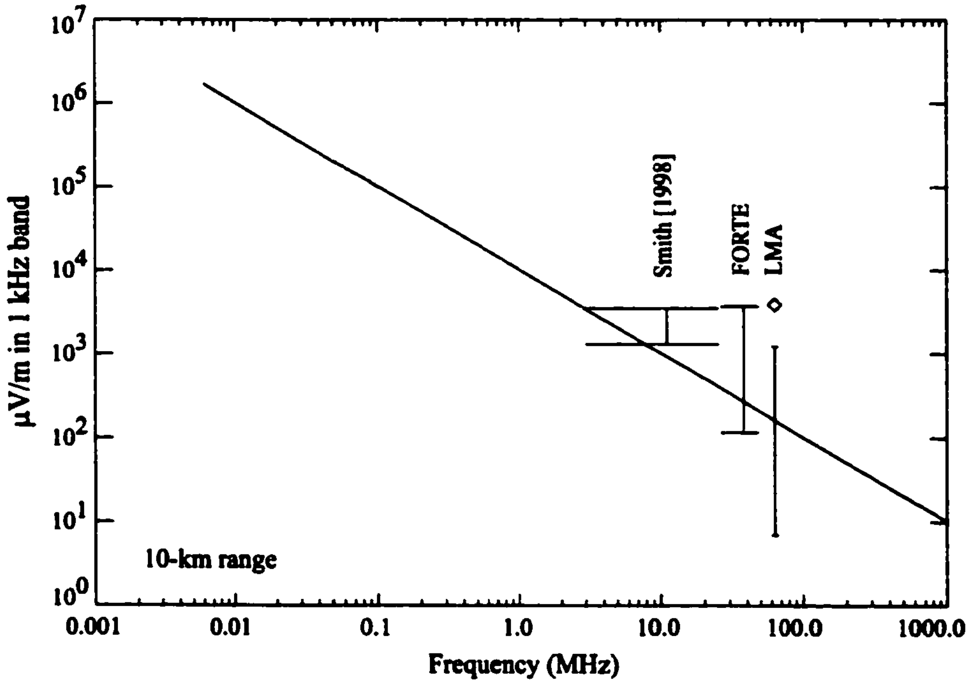

Figure 2.8 Peak electric field vs. frequency. The downward sloping line on this logarithmic plot represents the Pierce curve. The ranges of electric-field values produced by the events recorded by *Smith* [1998], FORTE, and by the LMA are shown as vertical lines. The bandwidths of the instruments used are shown as horizontal bars.

It was stressed by *Oetzel and Pierce* [1969a] that "there is no good reason why a phenomenon as complex as the radiation from lightning must follow precisely an inverse frequency law." These investigators also stress the need for more experimental results above 30 MHz. The peak amplitude shown in Figure 2.8 occurs at a frequency of about 5 kHz. Overall, the return stroke process is the strongest radiator from this frequency up to about 300 kHz. Later it was shown that first return strokes have a spectrum that falls off as $(1/f)^2$ from about 50 kHz up to about 20 MHz [*Uman*, 1987]. Above 10 to 20 MHz there is a wide range of measured intensities. It is convenient, nonetheless, to compare observations made by various investigators by scaling them in this manner.

For the measurements made by a 26-48 MHz radio receiver onboard the FORTE satellite, a wide range of estimated source powers has been reported [*Jacobson et al.*, 2000]. The majority of the source powers plotted in Figure 2.5 fall within the range of 1 kW to 1 MW. This range is plotted as representative of typical sources powers detected at FORTE. For "periodograms", calculated from electric-field waveforms recorded at FORTE, the power spectral density per unit area ($W/(m^2 \cdot MHz)$) or electric field squared per frequency interval $(V/m)^2/MHz$ was summed over frequency. Then the temporal peak of the band-summed power recorded in 400 μs was found, and this value was used to calculate the source power. To obtain the electric-field amplitude at 10 km that would be measured by a receiver with 1-kHz bandwidth, the power was assumed to scale in direct proportion with bandwidth [*Pierce*, 1977]. For example, to calculate the source power for a 1-KHz band given the peak power in a 22-MHz band, one must multiply by the factor

$$\frac{1\ kHz}{22\ MHz} \cong 4.55 \times 10^{-5} . \tag{2.5}$$

This gives [4.55×10^{-2} W, 45.5 W] for the power range of [1 kW, 1 MW] if scaled to a 1-kHz band. The power per unit area on the surface of a sphere 10-km distant is obtained by dividing these power values by $4\pi\cdot(10\ km)^2$. To obtain the peak electric field squared at a 10-km range the power densities are multiplied by 376.73 Ω, the impedance of free space. The square root of this quantity is plotted for the amplitude range of interest and the bandwidth of 22 MHz is plotted as horizontal lines. A similar procedure was carried out for the LMA data (60-66 MHz) for source powers ranging from 1W - 30kW, and this is plotted at its center frequency of 63 MHz. The 300-kW event mentioned in section 2.1.1 is plotted as a diamond. *Smith* [1998] reports the mean and standard deviation for the electric field from 3-25 MHz scaled to a 1-kHz band as 2.4±1.1 (mV/m). This is plotted using units of μV/m in Figure 2.8.

It is also interesting to add, as it has been explained by *Oetzel and Pierce* [1969a], that there is a general trend in the total number of impulses recorded per CG or IC flash as a function of frequency. They report that at 10 MHz one can expect to record hundreds to a few thousand pulses per flash. For receivers recording in the 50-100 MHz range the number of pulses in a flash will be as many as 10^4. Above 100 MHz, the number decreases, and above 200 MHz one can expect to record only a few hundred pulses. Also of interest is the separation of cloud flashes into those with apparent stepping and those with no apparent stepping by *Proctor* [1981]. This author reports that for receivers at 30, 250, 600, and 1430 MHz cloud flashes of the low emission rate type (stepping) produced measurable radiation at all four channels. Thus, stepping processes have been reported as being broadband and cover the VHF and part of the UHF frequency range. The high pulse rate discharges are generally not broadband. Stepping processes observed by the FORTE satellite are broadband and the physics involved might be similar to that which produces the VHF impulses associated with NBP signals.

2.1.4 Summary of Observations

Table 2.1 gives the peak electric fields in the time domain for NBP signals, and peak spectral amplitudes of the associated HF/VHF radiation as determined by some of the investigators mentioned in the preceding sections. These results will be compared with the electric radiation fields produced by runaway electron avalanches.

Summary of NBP and VHF/HF Pulse Observations Discussed Here			
Signal: Measurement	Observer / Sample Rate	Frequency Range	Amplitude (in band if frequency domain)
NBP: ΔE	[*Smith*, 1998] / 0.5-2 MHz	Response flat from ~ 300 Hz to 300 kHz	For 100-km range, Peak ΔE=9.5±3.6 V/m
HF accompanying NBP: E	[*Smith*, 1998] / 50 MHz	3-25 MHz	2.4±1.1 [mV/m @ 10 km, 1-kHz bandwidth]
NPBP: E	[*Willett et al.*, 1989] / (10^7/sec)	About 160 Hz- 3 MHz	For 100-km range, Peak E=8.0±5.3 V/m
HF accompanying NPBP: dE/dt	[*Willett et al.*, 1989] / (10^8/sec)	30-MHz bandwidth ~DC to 30 MHz	For 100-km range, Peak E=20.0±15 V/m/μs
VHF accompanying NBP:-	Lightning Mapping Array (LMA)	60-66 MHz	10-30 kW in 6-MHz band radiated from source (typical)
TIPP: E	FORTE (100 MHz effective sample rate for low passband)	26-48 MHz	1 kW to 1 MW in 22-MHz band peak power

2.2 Background of Runaway Theory

This section reviews the evolution of the concepts that laid the foundation for the model of runaway breakdown as it is applied to lightning. Some early papers on this topic include: *Gurevich et al.* [1992], *Roussel-Dupré et al.* [1993], and *Roussel-Dupré et al.*, [1994]. It is reasonable to pursue lightning models that invoke runaway theory because this is the only theory [*Roussel-Dupré et al.*, 1994], presently, that can explain observations of X-rays associated with lightning. In runaway models relativistic electrons can create significant X-ray radiation through the bremsstrahlung radiation process. In addition, a runaway avalanche can initiate in an electric field that is ten times lower than that required for a conventional discharge in air under similar conditions. This section presents a brief the history of runaway theory, its application to X-ray observations, and an existing 2-D runaway avalanche model that has been applied to lightning.

2.2.1 Cosmic Rays and X-ray Observations

C.T.R. Wilson hypothesized that high-energy β-particles (electrons) could be accelerated and multiplied in externally applied electric fields [*Wilson*, 1925]. This concept was derived from experimental knowledge of electron tracks in drift tubes.

> "When the energy of the β-particle exceeds 40,000 volts [40 keV], then even in the extreme case of an encounter in which the original particle gives half its energy to the ejected electron and is diverted through 45°, the energy remaining will exceed the critical value required for acceleration; there will in this case be two β-particles after the encounter, for each of which the component of the field along the path is more than sufficient to make the gain of energy per cm. exceed the average rate of loss."

Wilson [1925] stated that the "air carried up from the lower atmosphere contains radium emanation and its products" and this material could be pulled up into the updraft region of a thunderstorm and emit β-particles. Based on measurements made at the time, the β-particle emission rate from this source is $10/(\text{sec}\cdot\text{m}^3)$.

> "These β-particles are emitted with velocities greatly exceeding the minimum required for acceleration in the strongest parts of the field of a thundercloud; they will be accelerated even if they have initially a direction nearly at right angles to the field."

These high-energy particles would emit X rays via the process of bremsstrahlung radiation. Investigators, including *Eack et al.* [1996], *McCarthy and Parks* [1985], and *Parks et al.* [1981], were indeed successful in measuring increases in the background flux of X radiation. These observations were made using instruments on aircraft or tethered to balloons, and photon energy fluxes in the range of 5 to 120 keV were measured. The observations of *Eack et al.* [1996] were especially noteworthy because X rays and ambient electric fields were measured simultaneously, demonstrating the connection between the increased electric fields and increased X-ray counts. More recently, *Moore et al.* [2001] at Langmuir National Laboratory measured 10-μs integrated photon energies in excess of 1.2 MeV associated with the stepped leader of lightning.

2.2.2 X-Ray Intensification Model

A first quantitative attempt to explain X rays in thunderstorms was published by *McCarthy and Parks* [1992]. These authors mention two potential sources for the seed energetic electrons. One source is the decay of an isotope of radon gas, ${}_{86}Rn^{222}$. In a second scenario, energetic electrons are attributed to the decay of cosmic ray particles in the dense regions of the atmosphere. These authors mention that above about 3 km, neutral pions decay into pairs of γ rays, which then convert their energy, if sufficient, into electron-positron pairs. These background high-energy electrons gain energy in a thunderstorm electric field and lose energy in ionization and in the production of X-ray bremsstrahlung. *McCarthy and Parks* [1992] find that, for their model, neither source of high-energy electrons is sufficient to account for the observed X-ray fluxes. It is stressed, however, that the model is not an accurate representation of nature. The geometry is one-dimensional and the ambient electric field is assumed constant. Furthermore, the Earth's magnetic field, water vapor and hydrometeors, and the attenuation of the X rays from the source to the detector are neglected. It was clear from the work of *McCarthy and Parks* [1992] that X-ray bremsstrahlung might be enhanced by the acceleration of high-energy electrons in a thunderstorm field, but the calculated radiation was an order of magnitude lower than observations without considering attenuation. These authors do not include ionization as a source of additional high-energy electrons as was later considered by other investigators.

2.2.3 Electron Distribution Function and Rate Calculations

As mentioned by *Wilson* [1925] and quantified by *Gurevich et al.* [1992] and *Roussel-Dupré et al.* [1993] a newly born energetic electron will have an initial momentum at some angle with respect to the applied electric field. In order for this electron to gain more energy from the field than it loses in collisions it must have some initial angle-dependent energy above a threshold. Force equations can be written for individual electrons by assuming that a "slowing down" force acts to reduce the electron energy as a result of ionizing collisions. This effective drag force can be used to determine important parameters for a high-energy electron in air without considering changes in the electron orbit as a result of collisions, which is a stochastic process. Electron acceleration in an applied electric field is also a deterministic process. Quantities that are deterministic are known as a function of time given a set of initial values. By writing the collisional energy loss in terms of an effective drag force, the following equation set, (2.6), can be written. In Eq (2.6), μ is the cosine of the angle between the electron momentum and the applied, or external, electric field (Figure 2.9).

$$m_e \frac{du}{dt} = eE\mu - F(u)$$
$$\frac{d\mu}{dt} = \frac{eE}{m_e u}(1-\mu^2) \tag{2.6}$$

The equations listed above are included in *Gurevich et al.* [1992]. The kinetic energy and momentum are given by the following expressions. The ratio of the total relativistic electron energy (kinetic energy plus rest-mass energy) to its rest-mass energy is γ.

$$\gamma = \frac{\varepsilon_{tot}}{mc^2} = \frac{1}{\sqrt{1-\frac{u^2}{c^2}}}$$

Note that the electron kinetic energy is $\varepsilon = (\gamma - 1)mc^2$.

$$\vec{p} = \gamma m_o u$$

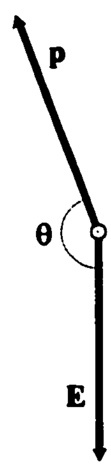

Figure 2.9. Energetic electron momentum, **p**, external electric field, **E**, and angle, θ.

The effective drag force is taken from *Bethe* [1930] and *Bethe and Ashkin* 1953]. This force is a function of the mean number of protons and bound electrons per molecule in air. For a composition of seventy-eight percent molecular nitrogen (14), twenty-one percent molecular oxygen (16), and one percent atomic argon (18) [*Rogers and Yau*, 1989], the mean molecular number Z is about 14.5. The drag force also depends on the number density of neutral species, N_m, and the electronic mass and charge. The frictional force depends on the electron energy through γ.

$$F_D = \frac{4\pi Z e^4 N_m}{mc^2} \frac{\gamma^2}{\gamma^2 - 1} S(\gamma) \tag{2.7}$$

$$S(\gamma) = \ln\left(\frac{mc^2}{I}\sqrt{(\gamma^2-1)(\gamma-1)/2}\right) - \frac{\ln(2)}{2}\left(\frac{2}{\gamma} - \frac{1}{\gamma^2}\right) + \frac{2}{2\gamma^2} + \frac{(\gamma-1)^2}{16\gamma^2} \tag{2.8}$$

In Eq (2.8), I = 80.5 eV, which is the total energy expended per ionization event. This is the ionization potential energy plus the average kinetic energy of the newly freed electrons. This force characterizes the slowing down of energetic electrons and the associated energy lost is converted into ionization potential energy and low-energy electron kinetic energy.

The effective drag on a group of high-energy electrons in a distribution can, instead, be characterized by two terms. One term represents an average momentum, or energy, loss as a result of collisions. The scattering of the electrons can be characterized by a diffusion term. Individual scattering events will not significantly change the mean electron energy or angular distribution of the group. Large deviations from an initial angle and momentum distribution only result from multiple small changes.

Note that the electron avalanche is not an equilibrium system. If a gas or plasma is in thermodynamic equilibrium then collisions do not change the momentum and angle distribution, f.

$$\frac{\partial f}{\partial t}_{collisions} = 0 \quad \text{Thermodynamic Equilibrium Condition} \tag{2.9}$$

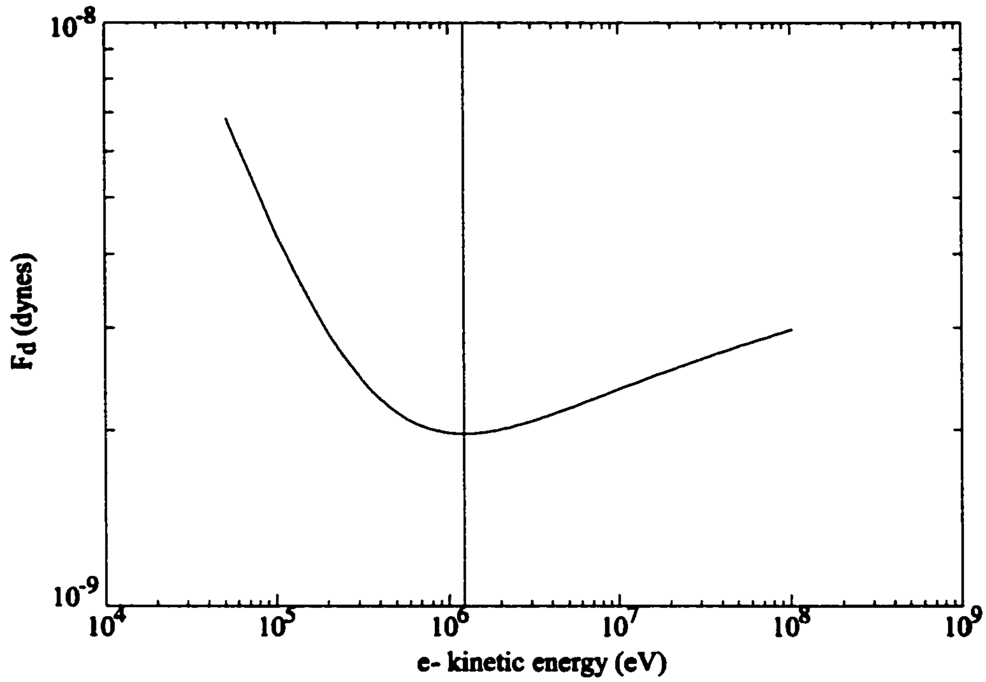

Figure 2.10. Effective drag force, Eq (2.7), as a function of electron kinetic energy. The minimum force occurs for an electron energy near 1 MeV.

Particle orbits are often represented in phase space. For non-relativistic particles, it is convenient to use a position and velocity space. For a relativistic group of electrons with energy greater than the rest mass energy $m_e c^2$, all velocities are near the speed of light and velocity is not a convenient parameter for describing the orbits. However, because the kinetic energies and momenta of the particles can increase to large values as the velocity asymptotically reaches c these quantities are employed in a relativistic modified Boltzmann equation.

The momentum and angle evolution of electrons, above an angle dependent minimum energy for avalanching to occur, is modeled in an atmospheric environment with pressure corresponding to an altitude of 5 km. An externally applied electric field of constant magnitude and direction, E, is assumed to be uniform over the computational angle and momentum grid. The distribution function has been calculated, as a function of time, for several values of applied electric field at the 5-km altitude. As a result of the applied forces and collisions, electrons groups will shift to new positions in phase space. The rate of change of the number densities of electrons as a function of momentum, angle, and time have been calculated by solving a relativistic modified Boltzmann equation [*Symbalisty et al.*, 1998]. For a uniform electric field, E, the equation for the electron momentum and angle distribution is

$$\frac{\partial f}{\partial t}-\left[\frac{(1-\mu^2)}{p}\frac{\partial f}{\partial \mu}+\mu\frac{\partial f}{\partial p}\right]eE=\frac{\partial_e f}{\partial t}. \tag{2.10}$$

Here, f is the distribution function, p is the scalar electron momentum, μ is the cosine of the angle between the momentum vector and the applied electric field vector, and the electron charge is denoted by e. Thus, the left hand side of the equation characterizes the evolution of particles acted on by an external electric field. Because the electric field is spatially uniform there are no spatial gradient terms and the momentum transport only occurs in momentum 'space.' Hence, there is no dependence on position in the above equation. The term on the right hand side is a collision integral and in its full form describes the rate of change of the momentum distribution function as a result of electron-air interactions.

$$\frac{\partial_e f}{\partial t}=\frac{1}{p^2}\frac{\partial\left(p^2F_D f\right)}{\partial p}+\frac{(1+Z/2)F_D}{4\gamma p}\frac{\partial}{\partial \mu}\left[(1-\mu^2)\frac{\partial f}{\partial \mu}\right]+Q_{ion} \tag{2.11}$$

The first two terms on the right side of Eq (2.11) contain the effective drag force mentioned previously. These terms are also relativistic and incorporate the dynamical friction force derived by Bethe. It is assumed that the incident electrons experience only a small change in the direction of their momentum per encounter and this assumption allows a Fokker-Planck analysis.

The ionization term of Eq (2.11) is

$$Q_{ion} = N_m c \frac{\beta}{\gamma^2 - 1} \frac{2\pi Ze^4}{mc^2} \int_{\varepsilon_L}^{\infty} d\varepsilon' \gamma'^2 Q_M(\varepsilon, \varepsilon') \frac{1}{2} \cdot \left[f(\varepsilon', \mu_+) + f(\varepsilon', \mu_-) \right]. \quad (2.12)$$

In Eq (2.12), Q_M is the Møller cross section as described in *Symbalisty et al.* [1998] and references contained therein. This terms represents a source of high-energy electrons and allows the beam distribution to grow in time. However, the energy loss corresponding to the production of these high-energy electrons is small compared to the energy loss associated with the production of low-energy electrons through the terms including F_D.

The ratio of the applied electric field, E, to the minimum electric field required for a relativistic electron to maintain its energy under the influence of external energy losses is the dimensionless parameter δ_o.

$$\delta_o = \frac{E}{E_t} \cong \frac{qE}{F_{D,\min}} \quad (2.13)$$

In Eq (2.13), δ_o is also expressed in terms of the electrostatic force and minimum effective drag force. The minimum drag force can be thought of as the electronic charge times the threshold electric field, E_t.

The electron distribution has been shown to evolve from a given initial distribution to one that is self-similar as a function of energy [*Roussel-Dupré et al.*, 1994]. That is, the normalized shape of the distribution function does not change; only the magnitude changes. Thus, the mean energy of the beam, or high-energy, electrons is taken to be constant. Furthermore, the mean energy of the beam only weakly depends on the applied electric field.

Figure 2.11 shows the distribution function, at a time after its shape has become unchanging in time, for three angles of electron momentum. Below $\mu=\cos\theta$ and $\mu=-1$ is the direction of propagation for the avalanche, which is anti-parallel to the applied electric field. As seen in this figure most of the high-energy electrons will have momentum anti-parallel to the applied electric field after the distribution function becomes self-similar in time. In addition, the electrons with this direction will have higher mean energy than those with initial momentum transverse, or 180 degrees from, the beam propagation direction.

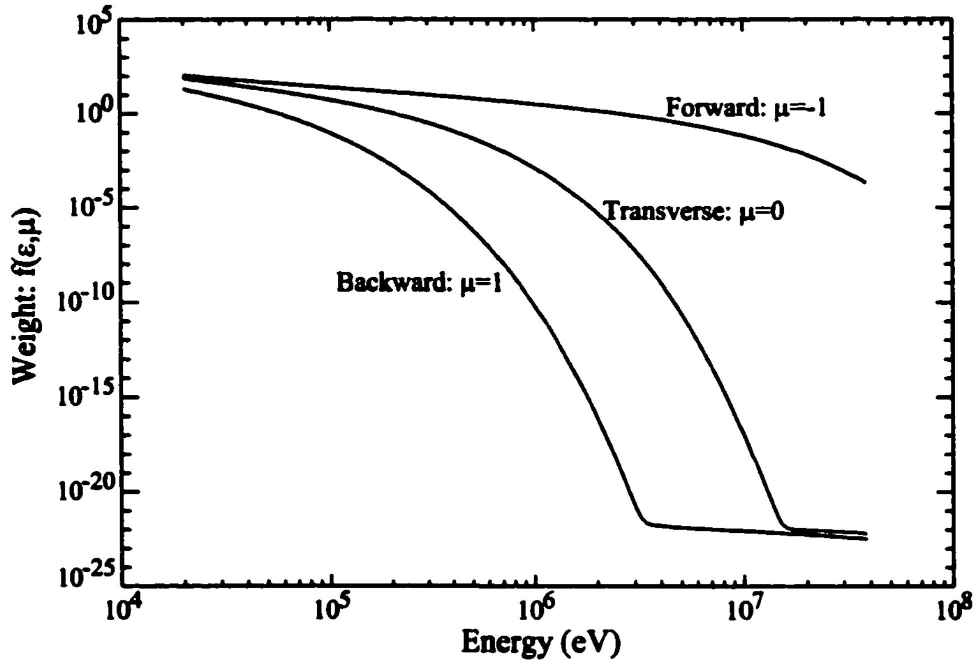

Figure 2.11 Distribution function $f(\varepsilon,\mu)$ vs. electron energy for three different values of $\mu=\cos\theta$. This example is for $\delta_o=6$.

The rates R_p, R_s, and α are functions of the local electric field and air pressure. We consider each of these rates in turn. The primary ionization rate used here, R_p, is calculated in *Symbalisty et al.* [1998]. These authors performed their calculation for an air density and pressure corresponding to a 5-km altitude for application to lightning models.

$$R_p = \frac{\partial \ln\langle\rho\rangle}{\partial t} \tag{2.14}$$

Above, ρ is the density of beam electrons. The time-dependent average density is a moment of the distribution function and the avalanche rate becomes constant after a time that is approximately equal to the avalanche time. Thus the growth of the distribution as a function of time implies a growth rate for the population of energetic electrons. A table of the calculated rates, as a function of δ_0, is found in *Symbalisty et al.* [1998] and an updated version of this plot is included here for reference (Figure 2.12).

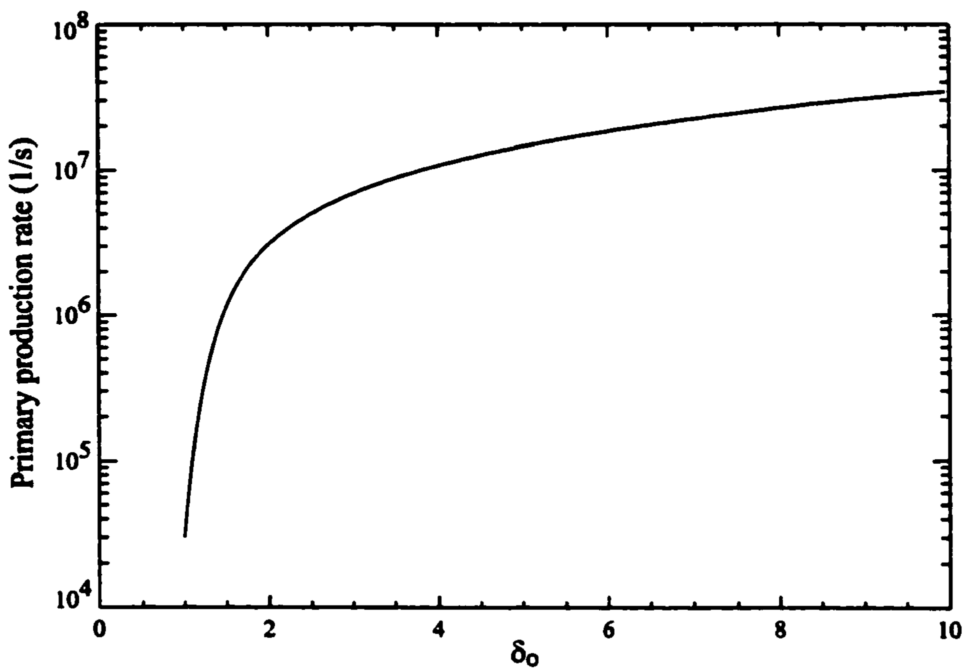

Figure 2.12 High-energy electron production rate as a function of δ_0.

Once the primary production rates are obtained for different values of *E/p*, an external electric field and atmospheric pressure characterize initial evolution of the runaway electron avalanche.

A second group of electrons included in runaway avalanche models are characterized by a relatively low mean energy of 1-3 eV. First this energy is discussed and then the rate of production for these electrons, R_s, is discussed. In addition to the characteristic mean energy, the low-energy electrons have a drift velocity in an external electric field where $mu_d^2/2$ is a small percentage of the total kinetic energy. The experimental mean characteristic energies are given as a function of electric field and air pressure by *Ali* [1986]. The following equations are valid for electric-field units of [V/cm] and pressure units of [Torr]. The average energy is given in units of eV.

$$1 \le \frac{E}{P} \le 5 \qquad T_e = 0.31 \cdot \left(\frac{E}{P}\right)^{0.75} \tag{2.15}$$

$$5 \le \frac{E}{P} \le 30 \qquad T_e = 0.82 + 0.035 \cdot \left(\frac{E}{P}\right) \tag{2.16}$$

$$30 \le \frac{E}{P} \le 54 \qquad T_e = 0.12 \cdot \left(\frac{E}{P}\right)^{0.8} \tag{2.17}$$

For a 5-km altitude, the pressure is ~372 Torr. The thunderstorm electric field in the 1-D model ranges from 1 to about 10 times the threshold electric field required for a runaway avalanche. At 5-km the electric field required for avalanche ionization is about 1.531×10^3 [V/cm]. Therefore *E/P* typically ranges from about 3.92 to 39.25 [V/(cm·Torr)] and the electron temperature range is 0.86 to 2.26 eV.

The ionization rate for the low-energy electrons, R_s, is found using the following considerations. The low-energy electrons are freed through ionizing collisions with the high-energy electrons. This is included in the modified Boltzmann equation through the effective drag force. This accounts for most of the primary electron energy loss, since ionizing collisions that result in newly born high-energy electrons are relatively infrequent. The average energy of the beam electrons was found to be constant with a value of 7.2 MeV. The energy lost per avalanche time, $1/R_p$, is equal to the energy gained. This energy is spent in the production of secondary electrons and is close to 7.2 MeV.

Thus, the number of secondary electrons produced per primary electron in an avalanche time can be approximated as 7.2 MeV/32 eV. The denominator, 34 eV, is the amount of energy expended in the production of an ion pair.

2.2.4 Existing Atmospheric Breakdown Model

A two-dimensional hydrodynamic and fully electromagnetic model of the runaway breakdown process occurring within a thunderstorm has been developed by *Roussel-Dupré and Gurevich* [1996], *Roussel-Dupré et al.* [1999], *Roussel-Dupré et al.* [1998], and *Roussel-Dupré et al.*, [2000], among others. Whether the application is lightning initiation or sprites and jets, the avalanche is modeled using the continuity equations and Maxwell's equations. The 2-D model includes the evolution of four ionic species as a function of space and time. Each ionic species is evolved by one flow equation that includes the dominant source and sink terms as well as a transport term. Eq (2.18) gives the dependence of the density of relativistic, "primary", electrons, n_p, as a function of time and space.

$$\frac{\partial n_p}{\partial t} = -\nabla \cdot n_p \vec{u}_p + R_p n_p + \frac{F_c}{\lambda_{mfp}} \tag{2.18}$$

The first term on the right side of Eq (2.18) is the advection term, or the transport of the electrons by the velocity field. The electron velocity, u_p, is obtained from the kinetic theory described above. The production rate of primary electrons is R_p, which is also obtained from solution of a relativistic modified Boltzmann equation [*Symbalisty et al.*, 1998]. The last term of Eq (2.18) is a source term, which represents the production of primary electrons by an incoming flux of cosmic rays. Though this flux is stochastic, it is treated as a constant fractional flux in this model. A different approach is adopted in this thesis and is described in Chapter 4. The cosmic ray flux of electrons having energy greater than ~1 MeV is given approximately as a function of altitude, H >11.2, in km, by

$$F_c\left[\frac{electrons}{cm^2 s}\right] \approx 2.5e^{-(H-11.2)/11.3}. \tag{2.19}$$

This expression for the flux of cosmic ray secondaries is discussed in *Roussel-Dupré et al.* [1998] and is an extension of that given by *Daniel and Stephens* [1974] for electrons with energies greater than 10 MeV. The mean free path, λ_{mfp}, is calculated using

$$\lambda_{mfp} = \frac{\langle \varepsilon_p \rangle}{F_D}. \tag{2.20}$$

The mean free path is the average kinetic energy of the primary electrons divided by the effective drag force. The division of the cosmic ray flux by the mean free path defines the production rate of primary electrons per unit volume per unit time. For the applied electric fields considered here, the mean energy is weakly dependent on the electric field. The primary electron energy is defined in terms of a moment of the distribution function, namely,

$$\langle \varepsilon_p \rangle = \frac{\int_{\varepsilon > 10keV} \varepsilon f(\varepsilon) \partial\varepsilon}{\int f(\varepsilon) \partial\varepsilon}. \tag{2.21}$$

The directions of motion and densities of the primary electrons are also influenced by the applied and self electric and magnetic fields. The electric and magnetic fields are calculated using Maxwell's equations [*Symbalisty*, 2001].

$$\frac{\partial \vec{B}}{\partial t} = -\nabla \times \vec{E}, \quad \frac{\partial \vec{D}}{\partial t} = \nabla \times \vec{H} - \vec{J} \tag{2.22}$$

$$B = \mu H \quad D = \varepsilon E \quad J = \sigma E + J_s \tag{2.23}$$

The changes in the electron momentum are calculated from these fields as solved in the relativistic momentum Eq (2.24). Below, $S = \gamma m_p u_p$. The self magnetic field is denoted $\boldsymbol{B}$, and the combined applied and self electric field is denoted $\boldsymbol{E}$.

$$\frac{\partial \vec{S}}{\partial t} = -(\nabla \cdot \vec{S})\vec{u}_p - en_p(\vec{E} + \vec{u}_p \times \vec{B}) - u_p \vec{S} \tag{2.24}$$

Eq (2.25) is the equivalent form of Eq (2.18), but for the "secondary" low-energy electron population.

$$\frac{\partial n_s}{\partial t} = -\nabla \cdot n_s u_s + R_s n_p - \alpha n_s + v_i n_s - \alpha_R n_+ n_s \tag{2.25}$$

The first term on the right side of Eq (2.25) accounts for low-energy electron transport by their velocity field. The production rate of secondary electrons is assumed to be proportional to the production rate of energetic electrons, $R_s = R_p \varepsilon_p / \varepsilon_i$. The energy loss per ion pair produced is denoted ε_i, which has a value of 34 eV for air. The energy of the incident primary electron is ε_p. The third term is a loss. It represents the total attachment rate.

Three body attachment: $O_2 + [M] + e^- \rightarrow O_2^- + [M]$ (2.26a)

Two body attachment: $O_2 + e^- \rightarrow O^- + O$ (2.26b)

Two body attachment: $H_2O + e^- \rightarrow OH^- + H$ (2.26c)

The fourth term on the right side of Eq (2.25) is the net rate of production of low energy electrons by other low energy electrons in ionizing collisions. The final loss term in Eq (2.25) accounts for recombination with positive ions.

The other two species included in the model are positive and negative molecular ions. The change in the density of negative ions as a function of time and space is given by

$$\frac{\partial n_-}{\partial t} = -\nabla \cdot n_- u_- + \alpha n_s - \alpha_I n_+ n_- . \tag{2.27}$$

The second term on the right hand side is the three-body attachment rate, which is a source for the negative ion density; this term was a sink for the low-energy electron density. The third term is the ion recombination coefficient times the density of positive ions and the density of negative ions.

The fourth species equation gives the change in the positive ion density as a function of time. All of these terms have been described previously.

$$\frac{\partial n_+}{\partial t} = -\nabla \cdot n_+ u_+ + R_s n_p + R_p n_p + \nu_i n_s - \alpha_I n_+ n_- - \alpha_R n_+ n_s \tag{2.28}$$

Now consider the current density. The currents are directed either anti-parallel (negative species), or parallel (positive ions) to the ambient electric field at each grid location. The currents are solved self-consistently with Maxwell's equations.

$$J = e(n_+ u_+ - n_- u_- - n_s u_s - n_p u_p) \tag{2.29}$$

A detailed study of the kinematics of high-energy electrons in uniform fields of different strengths was performed by *Roussel-Dupré et al.* [1994]. These investigators showed that the electrons of runaway avalanche beam could account for the observed x-ray emissions by including the avalanching effect. For example, at a 1-km range from a runaway discharge, a total number of 2.6×10^4 photons with 100 keV energy are expected, including attenuation. At a 2-km range, only 8 photons/event would remain. Thus, one must be close to the event to measure appreciable X radiation.

To elucidate the differences between a runaway model and a "conventional" model, the electron continuity equation from the 2-D streamer model of *Wang and Kunhardt* [1990] is shown here. These authors discuss the development of a streamer in a neutral gas between two infinite parallel-plate conductors. First consider the evolution of the streamer. In the beginning, there must be a seed electron. For the runaway model, this is a background cosmic ray secondary electron as shown in Eq (2.18). For the model of *Wang and Kunhardt* [1990] the seed electrons are produced by photoionization. This is the term S_{ph} in Eq (2.30). The electrons are transported by their velocity field, $\boldsymbol{u_e}$. This advection term is the first term on the right hand side of Eq (2.30). There is only one characteristic electron species. The electrons are of relatively low energy and there are two production terms: photoionization and electron impact ionization.

$$\frac{\partial n_e}{\partial t} = -\nabla \cdot n_e \vec{u}_e + (\alpha - \eta) n_e |\vec{u}_e| + S_{ph} \tag{2.30}$$

In the runaway model the energetic electrons define the scale length of the problem so that only advection of these electrons is included in most cases. The high-energy electron species can be created by the combination of ionization and acceleration in the cloud electric field. The low-energy electrons are produced by ionizing collisions associated with both species (primary and secondary). The runaway equation for the low-energy electrons includes impact ionization and differs from the treatment by *Wang and Kunhardt* [1990] because transport of these electrons over the much larger runaway scales is neglected, as is photoionization.

Chapter 3

State of the Art

This chapter discusses the current state of knowledge regarding the unusual NBP and VHF signals discussed in the previous chapters. First, existing models that give insight into the amplitudes and spatial scales of the currents involved in the production of the NBP waveforms is discussed. Second, models for the production of VHF associated with lightning processes other than the transient events of interest here are discussed. The predicted amplitudes and temporal characteristics from these models can be compared to the VHF associated with NBP events. Finally, a model that was explicitly devised to explain VHF radio emission by the TIPP events [*Roussel-Dupré and Gurevich*, 1996] is presented.

3.1 Parameterization of Possible Sources of NBP Signals

3.1.1 NBP Produced by Recoil Streamer

Much of the existing literature on RF lightning radiation includes derivations of the electromagnetic fields in terms of currents with modeled space and time variation. For empirical models, the space and time variation is often chosen such that the calculated electromagnetic fields will be consistent with observation, e.g. see *Master et al.* [1981]. Many of these models are transmission line models where the current pulse travels along a channel that was previously ionized, for example, by the stepped-leader process in a CG discharge. These types of models provide insight into the characteristics of the current sources. A model in which a time varying current pulse travels up a fixed channel for application to NBP signals was presented by *Le Vine* [1980]. This model was originally applied to the return stroke to explain the radiated waveform and, relatively weak, superimposed VHF. The tortuosity of the return stroke channel is thought to be responsible for the VHF radiation observed during a return stroke and this aspect of the model is discussed in section 3.2.2. For application to the NBP event, a slightly tortuous channel was taken to have a length of 1 km, with roughly vertical orientation, at an altitude of 5 to 6 km. The input current pulse, Eq (3.1), has an amplitude shape as a function of time that was proposed by *Uman*, [1987]. This is given below where α, β, γ, and δ are inverse time constants and I_1 and I_2 are fixed current amplitudes.

$$I_0(t) = I_1(t)(e^{-\alpha t} - e^{-\beta t}) + I_2(e^{-\gamma t} - e^{-\delta t}) \tag{3.1}$$

$$\alpha = \delta = 2.0 \times 10^4 \, [1/s] \quad \beta = 2.0 \times 10^5 \, [1/s] \quad \gamma = 1.0 \times 10^3 \, [1/s]$$

$$I_1 = 30 \, [kA] \qquad I_2 = 2.5 \, [kA]$$

For the NBP model, the current is negative and travels from a lower negative charge region to an upper positive charge region. The radiated waveform, observed from a range of 50 km, has a peak electric field of about 6 V/m. At a 100-km range, the expected peak field is about 3 V/m, which is consistent with the observations of *Willett et al.* [1989] and *Smith* [1998]. The current pulse is assumed to propagate at a speed of 1×10^8 m/s. This speed is typical for the current wave of the return-stroke process. This recoil streamer speed and length can explain the typical duration of NBP waveforms. The main differences between the NBP study and the return stroke study by *Le Vine and Meneghini* [1978] are that in the return-stroke study the channel was longer, the tortuosity was allowed to vary and results were given for current pulse propagation speeds of u=c/2 and u=c. No attempt was made to model the VHF radiation, and a spectrum of the radiation was not presented. The associated strong VHF radiation may be radiated by the breakdown process which rapidly forms the transmission line on which the NBP current flows [*Smith et al.*, 1998].

3.1.2 Estimates of Spatial Extent and Charge Transferred

"The relative timing between the RF [radio frequency in the HF range] emissions and the field-change emissions [NBP signal] suggests that the RF radiation is emitted during a breakdown process that forms a current-carrying channel...The temporal isolation of CIDs (compact intracloud discharges) suggests that initial breakdown in the events also occurs in virgin air." The HF/VHF radiation occurs during the first positive half cycle of the NBP signal. Based on these ideas, *Smith et al.* [1998] pursued a basic model to estimate the magnitude of the current, charge transferred, and spatial scale of the initial breakdown. This author assumed that the breakdown event occurred over a time of 3.2 μs. This was chosen because it is the median duration of a single TIPP pulse. The breakdown speed was treated as an independent variable. The speeds range from 1.0×10^7m/s, which is one-fifth the lower limit of the speed of a stepped leader pulse [*Uman*, 1987], up to the speed of light. Based on the fixed duration and various speeds, scale sizes were determined for the breakdown events. Then, based on a statistical analysis of the observed NBP waveforms and use of Eq (1.6), a typical dipole moment change, Δp, of 0.5 C-km was employed for the different cases. The charge transferred during the CID was calculated using $\Delta Q = \Delta p / \Delta z$. For a breakdown event with speed 1.0×10^7 m/s, a scale size of 32 m and a value of 16 C for charge transferred is estimated. For the case where the breakdown velocity is the speed of light, a scale size of 960 m and charge transferred value of 0.52 C is estimated. A range of other physical parameters were deduced that depend upon the breakdown speed.

3.2. Models of VHF Radiation Sources

3.2.1 Air breakdown related to the gliding discharge experiment (ONERA)

A somewhat detailed understanding of the physics responsible for fast current changes related to lightning processes is emerging through the work of *Bondiou et al.* [1987] and others. By analyzing discharges that occur on a dielectric surface, three different stages of spark formation have been identified, and these are compared to the natural lightning CG discharge. The physical quantity that clearly distinguishes the three phases is the conductivity of the ionized medium. The gliding discharge is thought to be started with the formation of an electron avalanche in an external or applied electric field. The charged particle density increases and the separation of charge under the influence of the applied field is the dominant process. This first stage is called the "predischarge", or "streamer" phase, and the spatial size of this phase varies depending upon the type of spark experiment. In the streamer phase, the electron temperature is much greater than the temperature of the quasi-neutral gas. The creation of this "predischarge" phase requires an applied electric field of about 11.2 kV/cm for negative streamers [*Labaune et al.*, 1990]. The streamer phase continues until the electrons heat the gas to a temperature of about 1500 K, at which any negative ions will have their excess electron detached, and then the streamer phase is said to transition to a leader phase.

Because of the increased number of free electrons, the resistivity of the gas decreases. The neutral particles reach thermodynamic equilibrium with the thermal electrons with a temperature of about 20,000 K within about 30 ns. These values are comparable to those of the lightning dart leader. The dart leader occurs in a previously ionized channel in contrast with the stepped leader, which ionizes neutral air. The experimental "leader" phase is characterized by a propagation speed of about 10^6 m/s, a current of about 100 A, and resistance per unit length of about 500 Ω/m.

The third process is referred to as the "arc" phase. This phase is characterized by a resistance of ~1 Ω/m and can occur when the streamer/leader touches a conducting surface.

Bondiou et al. [1987] present a semi-empirical model of the transient arc stage of a gliding discharge experiment. The transient arc corresponds to the transition from the streamer phase to the leader phase as discussed above. This particular stage is characterized by a current rise time of about 8 ns, which produces radiation in the VHF range. The transient arc phase is the fastest current change in the gliding discharge process. To quantify this transition phase based on physics, *Bondiou et al.* [1987] express the resistance, R, as a function of time based on a conductivity theory by *Rompe and Weizel* [1947]. In this model, the two processes of electron heating and ionization of the air are balanced by the power of the electron current in the applied electric field, E. Below, in Eq (3.2), the current density is j, the number density of electrons is n_e, the electron temperature is T_e, the Boltzmann constant is k, the ionization potential is ϕ_i, and the electron charge is e.

$$\frac{d}{dt}\left[n_e\left(\frac{3}{2}kT_e + e\phi_i\right)\right] = j \cdot E \tag{3.2}$$

The current is written in terms of the conductivity, σ, and the electron mobility, μ_e. The pressure factor, P_o/P, is included in the conductivity coefficient, A.

$$\sigma = n_e \mu_e e = \frac{j}{E} \tag{3.3a}$$

$$\sigma(t) = 2A\int_0^t j^2(\tau)d\tau \quad \text{where} \quad A = \frac{P_0}{P}\cdot\frac{\mu_e e}{\frac{3}{2}kT_e + e\phi_i} \tag{3.3b}$$

$$R(t) = \left(\frac{P}{2A_{exp}\int_0^t i^2(\tau)d\tau}\right)^{\frac{1}{2}} \tag{3.4}$$

Above, A_{exp} is the product of A with pressure. The value of $A\times P$ can be calculated by assuming the ionization potential to be that of nitrogen, 15.56 eV, the electron mobility to be 4.7×10^{-7} [$m^2\cdot V^{-1}\cdot s^{-1}$], and the electron temperature to be 2 eV. The calculated, or theoretical, value is $A_{th}=2.5\times10^{-3}$ [$atm\cdot m^2\cdot s^{-1}\cdot V^{-2}$], and the experimental value is $A_{exp} = 5.0\times10^{-5}$ [$atm\cdot m^2\cdot s^{-1}\cdot V^{-2}$]. A_{th} is greater than A_{exp} by a factor of 50, and the experimental coefficient is used for the model described below. *Bondiou et al.* [1987] explain that the discrepancy is because not all of the physics has been included in the theory. However, the duration of the transient arc phase and the propagation speed of the voltage pulse are in agreement with the experimental results.

The discharge plus the surface that it glides on, which includes a 2-mm thick dielectric and a metallic strip, are modeled as a RC transmission line. The capacitance per unit length of the dielectric/metallic strip system is 220 pF/m.

$$\frac{1}{R(x,t)}\frac{\partial^2 V}{\partial x^2} - \frac{1}{R^2(x,t)}\frac{\partial V}{\partial x}\frac{\partial R}{\partial x} = C\frac{\partial V}{\partial t} \tag{3.5}$$

The initial conditions are required and a solution to the second order differential equation for the voltage is obtained using an iteration method. The conditions of the discharge region just prior to the transient arc stage are characterized by a weak current and a constant electric field. The resistance as a function of time is calculated at each position along the channel using Eq (3.4) and is used in the solution of the RC transmission line equation. For application to the gliding discharge experiment, the length of the channel that transforms from a streamer to a leader is 5 cm.

Application of Model to Lightning VHF Radiation

To apply the ideas of the previous section to lightning *Bondiou et al.* [1987] run the previous calculation until a peak current of 1 kA is reached. The radiated electric field is then calculated for a 10-km range and a 1-kHz bandwidth for comparison with the Pierce curve. At this range the peak radiated field in the time domain is reported to be about 50 mV/m. The spectrum falls below the Pierce curve, but does lie within the lower range of values measured by both FORTE and the LMA (Figure 3.1). It would be interesting to see how the spectral and peak electric field results would change if the peak current were allowed to be 10 kA. By changing such parameters, this model might also be applied to the NBP events.

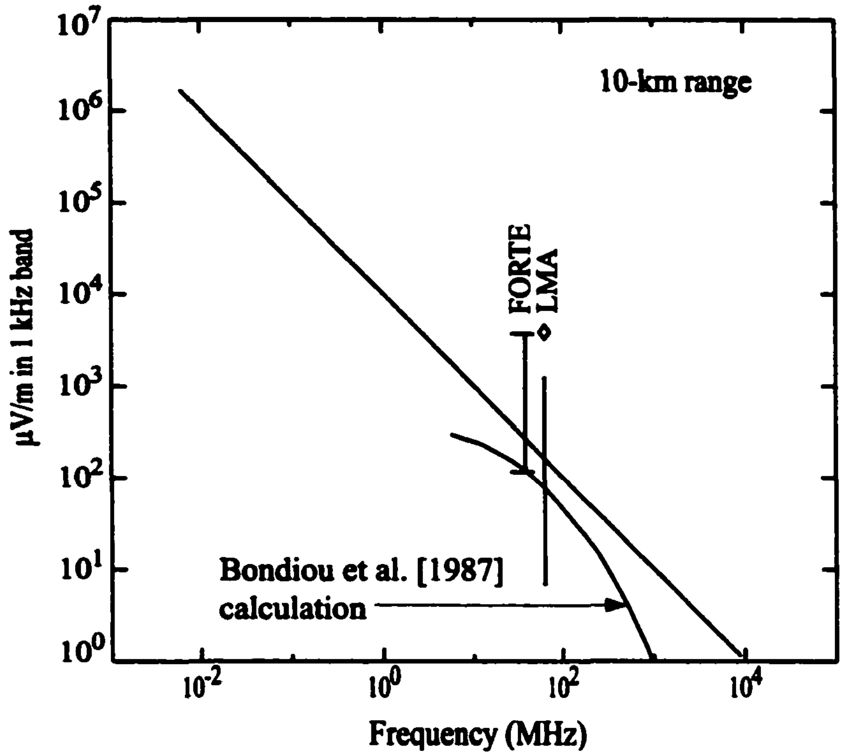

Figure 3.1. Calculation of electric field as a function of frequency by *Bondiou et al.* [1987] at a 10-km range. The Pierce curve is also shown for comparison.

3.2.2 Return Stroke VHF Radiation

Le Vine and Meneghini [1978] show that channel tortuosity and branching can increase the high frequency content present in a return stroke waveform. These authors use a random-walk computer simulation to produce a piecewise linear channel for the path of return-stroke current flow. For each channel segment, the time domain electric field is given by Eq (3.6a). The net radiated field is calculated by summing the field from each linear segment of the channel.

$$\begin{aligned}\bar{E}(\bar{r},t) = &\frac{\sqrt{\mu/\varepsilon}}{2\pi}\left\{\frac{\bar{\varepsilon}(\rho_b)}{\rho_b}I_0(t-\tau_b) - \frac{\bar{\varepsilon}(\rho_a)}{\rho_a}I_0(t-\tau_a)\right\} \\ &-\frac{1}{2\pi\varepsilon}\left\{\frac{\nabla\rho_b}{\rho_b^2}\int_0^t I_0(\xi-\tau_b)d\xi - \frac{\nabla\rho_a}{\rho_a^2}\int_0^t I_0(\xi-\tau_b)d\xi\right\}\end{aligned} \tag{3.6a}$$

$$\bar{\varepsilon}(\rho_{a,b}) = \left(\frac{1+\hat{l}\cdot\nabla\rho_{a,b}}{1-\hat{l}\cdot\nabla\rho_{a,b}} \right)^{1/2} \hat{\varepsilon}(\rho_{a,b}) \tag{3.6b}$$

$$\hat{\varepsilon}(\rho_{a,b}) = \frac{\hat{l}-(\hat{l}\cdot\nabla\rho_{a,b})\nabla\rho_{a,b}}{\left(1-(\hat{l}\cdot\nabla\rho_{a,b})^2\right)^{1/2}} \tag{3.6c}$$

Above, ρ_a and ρ_b are the distances from the bottom and the top of a given channel segment to the observer, respectively. The unit vector for the channel orientation is denoted l. The input current pulse, of the same form as Eq (3.1), has an amplitude vs. time shape that was proposed by *Uman* [1987].

These authors were successful in reproducing the $1/f^2$ dependence of return stroke spectra above 10 MHz. It is believed that channel tortuosity and branching are the sources of VHF coinciding with return strokes. Tortuous channels were shown to radiate signals with more high frequency (10^5-10^9 Hz) content than similar straight channels. These authors also point out that a decrease in the length of the channel segments will result in higher-ampiitude high frequency content. The spectral intensity for frequencies below about 100 kHz is dependent upon the input current and the total channel length. Longer total-channel lengths increase the low-frequency intensity of the return-stroke spectra. Radiation in the VHF range associated with the return-stroke process continues as the return stroke current moves up the partially ionized channel. The VHF radiation associated with the return stroke has ~100-μs duration, while the VHF radiation associated with NBP signals usually has ~3-μs duration.

3.2.3 VHF Associated with Runaway Beam: Analytic

The angular dependence of the radiated Poynting flux for a relativistic point charge that is increasing in magnitude exponentially in time and moving with a speed, $\beta_p = u/c$, near 1.0 and the corresponding secondary electron charge has been calculated by *Roussel-Dupré and Gurevich* [1996]. The Poynting flux, F_R, at range R is given by the following analytic expression.

$$F_R = \frac{c}{4\pi} \cdot \left(\frac{e\nu}{Rc}\right)^2 \cdot \frac{\beta_p^2 e^{2\eta} \sin^2\theta}{(1-\beta_p\cos\theta)^4} \left(1 + \frac{\varepsilon_p}{\varepsilon_i} \cdot \frac{\beta_s}{\beta_p} \cdot \frac{1-\beta_p\cos\theta}{1-\beta_s\cos\theta}\right)^2 \tag{3.7}$$

Above, ν is the avalanche rate, η is the number of e-foldings of the beam, and θ is the observation angle measured from the direction of beam propagation. The low-energy electron drift speed divided by the speed of light is β_s. The factor $\varepsilon_p/\varepsilon_i$ is the primary electron energy divided by the energy required to produce an electron-ion pair. The derived angular factors were plotted and it was shown that, for the primary electrons, the peak amplitude was higher than the amplitude for an observer at 90 degrees by a factor of about 1000. For the low energy electrons this ratio is about 100. The behavior of the spectral intensity as a function of angle for the primary electrons of the point charge model was given as

$$\frac{1}{\nu^2 + \left(1-\beta_p\cos\theta\right)^2\omega^2} \cdot \tag{3.8}$$

Thus, it was shown that for typical avalanche rates at sea level (20-600 MHz) the amplitude of the spectrum at radiated frequency, ω, in the VHF range would be significant for small observer angles. For $\omega >> \nu$, Eq (3.8) falls of $1/\omega^2$. Based on these results the radio emissions of a low-altitude and high-altitude runaway avalanche were calculated. The amplitude of the radio emissions depends on the number of e-foldings of the beam, η. In the following chapter, a numerical method for calculating the radiated electric field is compared with this analytic result.

Chapter 4

Problem Solution

This research investigates the VHF radio emissions and peak radiation electric fields that could be produced by runaway electron avalanches in external thunderstorm electric fields. Based on the information provided in the previous chapters, it is reasonable to hypothesize that the runaway avalanche process is responsible for the ionization, or initial breakdown, of air and the corresponding rise time of the NBP signals discussed in detail in Chapter 2. This investigation extends the work of *Roussel-Dupré and Gurevich* [1996]. The analytic model that these authors presented characterized the electron beam as a point charge, with speed β, that increased in magnitude exponentially in time. The relative electric-field amplitude and spectral intensity in the VHF range was reported as a function of observation angle.

This thesis is an important investigation because a very fundamental question about lightning remains unanswered. That is: How is lightning initiated? The NBP events sometimes precede large-scale lightning flashes. If modeling efforts such as this can or cannot reproduce observations of the NBPs, then we may have learned something about the source physics that produces these unusual signals. However, models are simply mathematical descriptions of real objects or events. They only provide a means for humans to conceptualize and predict phenomena. There is yet much to be learned about the NBP and time correlated VHF signals and this thesis is a small step toward gaining that knowledge.

To solve this problem a numerical calculation of electric fields in the radiation zone given a discrete set of current values in space and time was needed. The numerical method is discussed in section 4.1 and the program is given in Appendix A. In section 4.2 the assumptions made for the model of the 1-D runaway electron avalanche are presented. The runaway electron avalanche program is provided in Appendix B. In section 4.3, the ambient environment that the model runaway electron avalanche evolves in is discussed.

4.1 Numerical Calculation of Radiation Electric Field

The angular dependence of the radiated Poynting flux for a relativistic point charge that is increasing in magnitude exponentially in time and moving in the positive z direction with dimensionless speed, $\beta_p = u/c$, has been calculated by *Roussel-Dupré and Gurevich* [1996]. The low-energy, or secondary, electrons are modeled as a point charge of magnitude $(\langle\varepsilon_p\rangle/34\ \mathrm{eV})\cdot Q_p$. Because the primary electrons produce these, the secondary electrons are assumed to occupy the same point in space as the primary electrons. The corresponding peak electric field, E_p, as a function of observation angle is given by the following analytic expression in cgs units.

$$E_p = \frac{e\nu}{Rc} \cdot \frac{\beta_p e^{\eta} \sin\theta}{(1-\beta_p \cos\theta)^2} \cdot \left[1 + \frac{\varepsilon_p}{34eV} \cdot \frac{\beta_s}{\beta_p} \cdot \frac{1-\beta_p \cos\theta}{1-\beta_s \cos\theta}\right] \tag{4.1}$$

Above, ν is the avalanche rate, η is the number of e-foldings of the beam (i.e. high-energy or primary) electrons, and θ is the observation angle measured from the direction of the beam propagation. In the model avalanche discussed in section 4.2, the production rates will be variable and the decay of the avalanche will also be included, so the analytic expression (4.1) can not be used. It is necessary to solve for the electric field numerically.

Numerical computations are often tested by comparing the numerical results with analytic results. The analytic solution for the point-charge avalanche is considered here. The electric radiation field for relativistic point charges moving upward along a z-axis, and increasing in magnitude at an avalanche rate, ν, is calculated numerically for comparison. Einstein's postulate of the constancy of the speed of light, calculation and time differentiation of the Liénard-Wiechert vector potential, and a time step that resolves the phenomenon under investigation are employed in the numerical calculation. The angular dependence of the peak electric-field amplitude is shown to be in agreement with the analytic result given in Eq (4.1).

The numerical calculation is carried out as follows. An avalanche rate, ν, is selected that corresponds to a realistic ambient electric field. The source is a point charge moving up the z-axis with dimensionless speed β. The number of relativistic particles initiating the avalanche, N_o, is one.

$$N(z,t) = N_o \cdot e^{\nu t} \delta(z - \beta c t) \tag{4.2}$$

For comparison with Eq (4.1), the charge can be allowed to increase in magnitude for an arbitrary amount of time. It is only important that the maximum number of electrons be retained for use in calculating the number of e-foldings of the beam, η, using

$$\eta = \ln(N_{max} / N_o). \tag{4.3}$$

The vector potential is calculated as a running sum and an interpolation scheme is used. The analytic expression for the vector potential (see Chapter 1),

$$\vec{A}(\vec{r},t) = \frac{1}{c} \int \frac{\vec{J}(\vec{r}\,',t')}{|\vec{r} - \vec{r}\,'|} dV, \tag{4.4}$$

is converted to finite difference contributions ΔA. For each point along the z axis where the current density is non-zero, the component of ΔA transverse to the propagation vector, ΔA_t is taken. In equation (4.5), the factor (r_{obs}/R) is the sine of the observation angle. Since the transverse vectors for various positions, z', on the source grid will not have the same directions, these contributions are also broken up into vertical and horizontal components for the running sum (see Appendix A).

$$\Delta A_t(t'+R/c) = \frac{J(z',t')\Delta V}{cR}\left[\frac{r_{obs}}{R}\right] \tag{4.5}$$

Now the interpolation is discussed. The time at which a vector potential contribution like the one in equation 4.5 will be observed, $t'+R/c$, is known. However, an observation time grid is used in practice, $t_{obs}(m)$, for summing the vector potential contributions. A single simulation, or source, time is shown in Figure 4.1. Note that currents at different positions on the z axis will contribute to the vector potential sum at a single observation point, P, at different times. The time $t'+R/c$ will, in general, fall between two discrete points on the observation time grid. If these 2 discrete times are indexed by m and $m+1$, the linear interpolation factor in Eq (4.6.a) is used to weight the vector potential contributions. Note that a scaling factor for the time steps is also needed, and this is discussed below.

$$fac = \frac{(t'+R/c) - t_{obs}(m)}{t_{obs}(m+1) - t_{obs}(m)} \tag{4.6.a}$$

$$\Delta A_t(m) = (1 - fac)\cdot \Delta A_t(t'+R/c) \tag{4.6.b}$$

$$\Delta A_t(m+1) = (fac)\cdot \Delta A_t(t'+R/c) \tag{4.6.c}$$

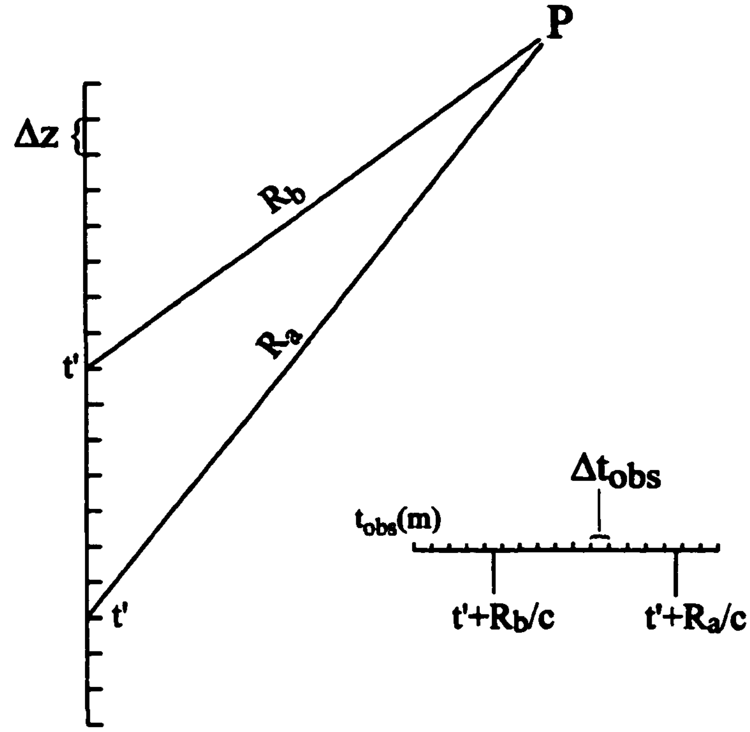

Figure 4.1. Spatial grid, observation point P, and observation time grid.

Once the vector potential is obtained, the electric field in the radiation zone is calculated by taking the time derivative.

$$\vec{E}_{\theta}(\vec{r},t) \cong -\frac{1}{c}\frac{\partial \vec{A}_t}{\partial t} \qquad \text{(analytic)} \qquad (4.7a)$$

$$E_{\theta}(m) = \frac{1}{c}\frac{A_t(m-1) - A_t(m+1)}{2\cdot \Delta t_{obs}} \qquad \text{(finite difference)} \qquad (4.7b)$$

Further discussion on the observation time step is provided here. First, it was necessary to resolve the smallest time scale of interest in the model. For the model electron avalanche, the rise time of the current and associated radiation field need to be resolved for calculation of the VHF radiation. The observation time grid was taken to have constant temporal cell size, Δt_{obs}, for each observation angle. However, Δt_{obs} was varied with observation angle. Each source current exists over a time Δt_{src}, which is constant and independent of observation angle.

The choice for the angle-dependent observation time step can be explained as follows. Consider the minimum time separation of two "events." For the point-charge source, the two events are marked by the time and space coordinates of the point charge locations. The first event of the point charge is chosen arbitrarily as some point on the z-axis and corresponding time. The second location and time considered are for the neighbor cell after the charge has moved a distance Δz. The time for a charge to move from one cell to its neighbor is Δt_{src}. The time separation of these two events as seen by an observer is different. If the observer is a satellite and the point charge is moving upward from the Earth's surface then the time for radiation to travel from the first location of the particle is larger than the time for radiation to travel from the second position. The time separation of the events is Δt_{src} minus the travel-time difference, which is $\Delta z \cdot \cos\theta / c$. Note that $\Delta z = \beta c \Delta t_{src}$. Thus, the optimal observation-time resolution for a relativistic point charge is

$$\Delta t_{obs} = \Delta t_{src}(1 - \beta \cos\theta)\,. \tag{4.8}$$

This is a consequence of relativistic speed of the point charge and the constant speed of light. Radiation will be relatively compressed for $\theta<90°$ and relatively spread out for $\theta>90°$. However, with a two-point interpolation scheme, the use of Eq (4.8) for the temporal resolution can lead to simulation noise. Noise occurs where there is zero contribution to the vector potential adjacent to non-zero contributions on the observation-time grid. The time derivative is taken to calculate the electric field, and, thus, it is not unusual to have negative and positive electric-field values at neighboring time steps. This results in large errors in the numerical calculation of radiation fields. In practice, the right side of Eq (4.8) is multiplied by a factor greater than one. This allows for a greater number of vector-potential contributions at a given Δt_{obs}. It is, however, important that Δt_{obs} is small enough to resolve the rise time of the radiation from the process under consideration. Therefore, a factor that minimizes the noise and still resolves the signal peak is chosen and this is not necessarily the same for each case.

Now consider conservation of charge for the source and observer. The observation time intervals are, in general, different from the source time intervals. If, for example, the observation time were longer than the source time, it would be incorrect to imply that the current from the source applies over the longer time interval with equal strength as it does in the shorter source time interval. It is necessary to multiply each contribution to the vector potential by $\Delta t_{src}/\Delta t_{obs}$ to ensure conservation of charge.

For the results shown in Figure 4.2, a spatial step of 0.25 m and simulation time step of 0.25[m]/(βc) was used, with β=0.98767. Thus, one time step corresponds to one step in the z direction. The analytic (solid curve) and numerical (dashed curve) results are within 10% for all observation angles. A non-relativistic case and a case including only the primary electrons of Eq (4.1), first term in parentheses, are shown in Appendix A. The true relative percent error is calculated for each observation angle using

$$\% error = \frac{E_A - E_N}{E_A} \times 100\% . \tag{4.9}$$

Above, E_A is the analytic peak electric field and E_N is the numerical peak electric field.

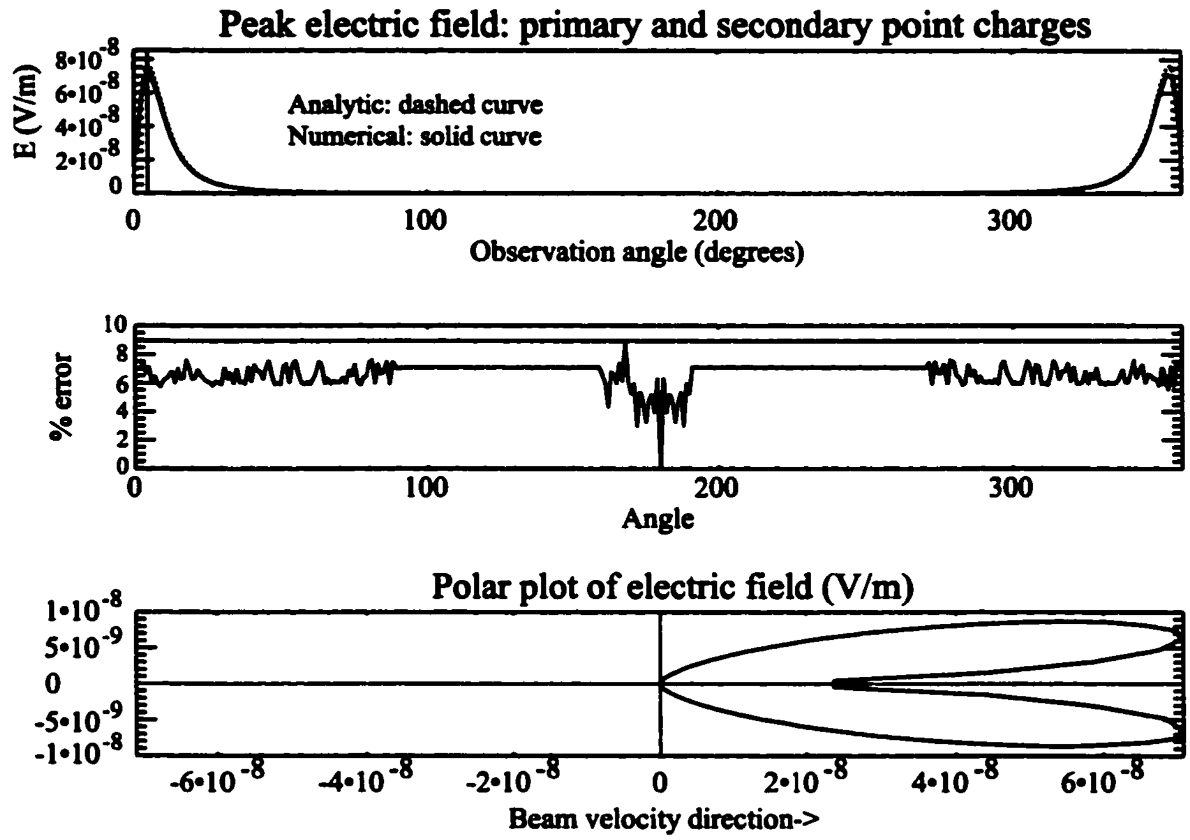

Figure 4.2 Results for model of primary and secondary electrons as point charges. Top: peak electric field as a function of observation angle. Middle: percent error relative to the analytic peak electric field model. Bottom: polar plot of peak electric field (numerical result).

4.2 One-Dimensional Model of Runaway Electron Avalanche

The point charge model represents an idealized case. A real electron avalanche will have a variable avalanche rate along its central axis and will be spread out in space. Both of these facts will cause the angular distribution of the radiated power to deviate from the analytic point charge case. The avalanche and loss rates control the rise time and the decay time of the beam and this will also determine the amplitude and spectrum of the radiated field.

The variation of the runaway avalanche rates with ambient electric field strength and pressure has been studied by previous investigators [*Babich et al.*, 2001; *Gurevich et al.*, 1992; *Symbalisty et al.*, 1998] and the results of *Symbalisty et al.* [1998] are employed here. The literature discussing the avalanche rates includes the physical effects of energy loss by Coulomb collisions and energy gain from the ambient electric field. This was discussed in Chapter 2.

The following physical processes are considered significant for the 1-D avalanche model considered here: high-energy, "primary", electron avalanche and loss rates, low-energy, "secondary", electron avalanche and loss rates, secondary electron attachment, and the reduction of the ambient electric field inside the beam because of the increasing conductivity. These processes are described in detail in the following paragraphs. Note that the term "primary" refers to the high-energy electrons of the avalanche. This is because, for this model, the high-energy electrons are responsible for all of the ionization. Some confusion results from the use of this term because new high-energy electrons are added to the beam via the ionization processes. These "new" high-energy electrons are really secondary electrons, but because they then produce further ionization they are called primary electrons. The low energy electrons do not produce any further ionization, in this model at least, and because of this they remain in the "secondary" electron category. The term "secondary" refers exclusively to the low-energy electrons.

4.2.1 Primary Electrons

The production rate of primary, or high-energy, electrons by ionization is written below as R_p. Primary electrons, which ionize atoms and molecules, free new electrons and these electrons have a probability of having a certain initial free kinetic energy. If these new energetic electrons have energy greater than about 10 keV, they are considered "energetic" secondary electrons. They accelerate in the electric field and reach an average energy of 7.2 MeV on a timescale approximately equal to the avalanche rate.

$$\frac{\partial n_p}{\partial t} = R_p(\delta_0)n_p \qquad (4.10)$$

Above, n_p is the number density of primary electrons and δ_0 is the ambient electric field divided by the threshold field required for an energetic electron to maintain its energy. The avalanche rate is a function of δ_0. Eq (4.10) is applied only when δ_0 is greater than or equal to 1.4. In this regime the primary electrons avalanche and maintain a mean energy of 7.2 MeV according to the detailed kinetic calculations. Note that in the program given in Appendix B, the ambient electric field is divided by the electric field required for avalanching.

The decay of the beam is treated using the assumption that the high-energy electrons are subtracted from the beam in collisions. The loss in the number density of primary electrons from collisional processes is

$$\frac{dn_p}{dt} = \frac{1}{\langle \varepsilon_p \rangle}\frac{d\langle \varepsilon_p \rangle}{dt}n_p. \qquad (4.11)$$

Above, $\langle \varepsilon_p \rangle$ is the mean energy of the primary electrons. This equation is applied only when the net electric field falls below a given threshold (δ_0 <1.0). Otherwise the beam is sustained by the electric field, or avalanches if δ_0 >1.4, and maintains a mean energy of approximately 7.2 MeV as mentioned previously. According to the kinetic calculations the electron beam produced by a runaway electron avalanche is collimated in the direction antiparallel to the applied electric field. When the electric field falls below the threshold needed for energetic electrons to maintain their energy, the mean energy of the beam decreases and by definition the number density of the beam must decrease. If the electric field is parallel to the beam motion then the beam loses energy faster and the number density decreases faster. This effect can be represented as

$$\frac{d\langle \varepsilon_p \rangle}{dx} = F_{net} = -F_D - qE\,. \tag{4.12}$$

Using this expression, the net force can be used to characterize the loss of primary electrons where the electric field is too low for primary electrons to maintain their energy. The minimum drag force, F_{Dmin}, occurs for an electron energy of about 1.4 MeV. The effective drag force on a 7.2-MeV electron is given by equation (2.7) and the factor related to the energy of the primary electrons, $\gamma^2/(\gamma^2-1)$, here is estimated to be about 1 for both the 1.4 and 7.2 MeV electrons. Furthermore, the approximation $S(\gamma(1.4\text{MeV})=S(\gamma(7.2\text{MeV})$ is made so that

$$\frac{1}{\langle \varepsilon_p \rangle}\frac{d\langle \varepsilon_p \rangle}{dt} = \frac{F_{net}}{\langle \varepsilon_p \rangle}\frac{dx}{dt} = \left[-\frac{F_D}{F_{D\min}} - \frac{qE}{F_{D\min}}\right]\frac{u_p}{\langle \varepsilon_p \rangle}F_{D\min} \cong -(1+\delta_0)\nu_{coll}\,. \tag{4.13}$$

Eq (4.13) provides an adequate approximation to the primary loss rate. A more precise formulation would require a detailed kinetic calculation coupled to Maxwell's equations. The proposed model captures the essential physics and is adequate for characterizing the rise time and peak electric field of the avalanche.

The primary electron current density, J_p, is calculated using

$$J_p = n_p \cdot e \cdot u_p\,. \tag{4.14}$$

If a certain number density, n_p, exists there will be a corresponding current density with constant velocity u_p. Note that for the energy range that defines the beam electrons $u_p \sim c$

so that the magnitude of the current density is effectively dependent upon the charge density.

The electron density is transported by shifting the density profile up one spatial step for each time step, which is taken to be $\Delta z/u_p$. A time step that is not exactly equal to the spatial step size divided by the velocity of the primary electrons can also be used, only it would be necessary to interpolate the density profile at each time. The beam is assumed to have an initial axial profile that is Gaussian in shape. The axial spread is the 1/e width of the density profile.

The cosmic-ray flux is assumed to be small for the 1-D runaway electron avalanche model. For an altitude of about 11.2 km, the cosmic-ray electron flux, Eq (2.19), is about 2.5 [e-/(cm^2·s)]. The mean free path of a high-energy electron (7.2 MeV) at this altitude, for the ambient electric fields considered in the thunderstorm model, is about 50 m. Since the length over which the avalanche develops is about 1 km (20 mean free paths), the radius is about 0.5 m, and the total time of the simulation is about 7μs, about 3 high-energy electrons will be added to this volume during the avalanche. This contribution is neglected. However, avalanching by these electrons may be important over a longer time scale and larger spatial scale. By neglecting this contribution, an avalanche initiated by a single electron is considered here.

4.2.2 Secondary Electrons

The energy distribution of the electrons that are ionized by the beam electrons has two peaks. One is at ε_p = 7.2 MeV and the other is at ~1-3 eV (see Chapter 2). The low-energy electrons have a random velocity component and a drift velocity in an applied electric field as determined from swarm measurements [*Ali*, 1986]. Their production rate is proportional to the production rate of energetic electrons, $R_s = R_p\varepsilon_p/\varepsilon_i$. The energy loss per ion pair produced, ε_i, is 34 eV. The secondary electrons are produced by the primary electrons and thus the secondary avalanche rate is multiplied by the primary electron density.

$$\frac{\partial n_s}{\partial t} = R_s n_p \tag{4.15}$$

The secondary electrons are assumed to be subtracted from the environment via 2-body and 3-body attachment, Eq (2.26). The attachment rate is much smaller than the secondary electron production rate for the ambient conditions considered here. However, it multiplies the secondary electron density where as the secondary production rate multiplies the primary electron density. The attachment rate is calculated for 5-km as a function of δ_o and this is shown in Figure 4.3.

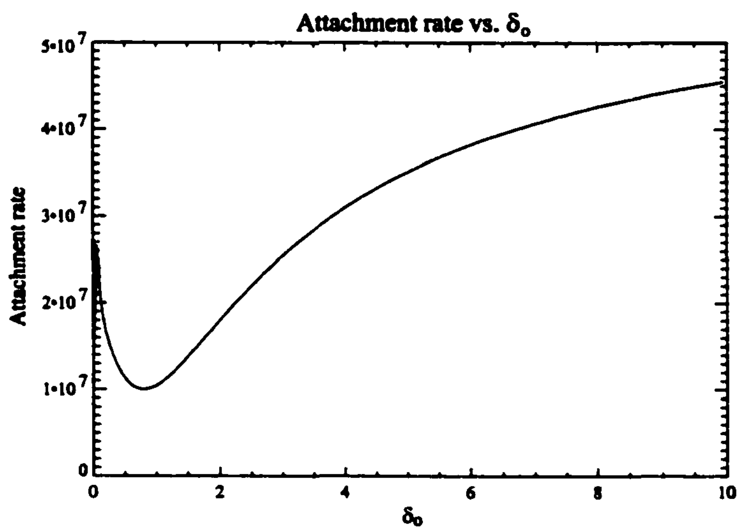

Figure 4.3 Attachment rate for 5-km altitude as a function of overvoltage.

Low-energy electrons continue to attach over the lifetime of the simulation. Primary, ionizing, electrons move out of a region leaving low-energy secondary electrons behind, and the low-energy electrons will attach with molecules and atoms at some rate as long as the species involved are present. Over longer timescales, attachment can reduce the conductivity of previously ionized regions. The rate equation for the secondary electrons is written

$$\frac{\partial n_s}{\partial t} = R_s n_p - \alpha n_s \ . \tag{4.16}$$

The other processes included in Eq (2.25), are small in comparison to avalanching and attachment and are not included in the 1-D model. The ionization by the secondary electrons may be important in the later stages of the discharge, but that is beyond the scope of this report.

The low-energy electron current is used in the calculation of the electric field in the radiation zone. The secondary current, J_s, is calculated using

$$J_s(z',t') = n_s(z',t') \cdot e \cdot u_{drift}(z',t'), \text{ where } u_{drift}(z',t') = \frac{e \cdot E}{m_e \cdot \nu_{coll}}. \tag{4.17}$$

The collision frequency, ν_{coll}, is dependent upon the ambient electric field and pressure. This is given in *Ali* [1986] for the ambient conditions of interest here as

$$\frac{\nu_{coll}}{P} = \frac{2.35 \times 10^9 (E/P)}{1 + 0.58(E/P)} \quad \text{for} \quad 1 \le E/P \le 30 \quad \text{or} \quad 0.35 \le \delta_o \le 10.5 \,. \tag{4.18}$$

The collision frequency for the low-energy electrons is typically on the order of 10^{12}/sec and is weakly dependent upon E/P. Because the drift velocity is proportional to the ambient electric field, the current goes to zero when the electric field goes to zero. A high value for the drift velocity calculated in the simulation is about 2×10^5(m/s). For the entire simulation time of about 7 μs the secondary electrons would move about 1.4 m if traveling at a constant peak drift velocity. Since the grid spacing used here is 0.5 m, the low-energy electrons are assumed to occupy the cell they are created in for the entire simulation.

Because the dominant rates are the production and destruction of the primary and secondary electrons and attachment, the equations

$$\frac{dn_s}{dt} = -\alpha n_s + R_s n_p \tag{4.19}$$

$$\text{and} \quad \frac{dn_p}{dt} = R_p n_p \tag{4.20}$$

are used. Heavy ion currents are neglected. These equations are coupled, linear, first-order ordinary differential equations and can be solved simultaneously using a non-standard finite difference approach presented by *Mickens* [2000]. A simultaneous solution is desirable since the densities of both species will be updated based on the previous values. The general eigenvalue method for solving systems of equations like these can be found in *Strang* [1988] and other linear algebra texts. It is assumed that the coefficients, rates, are constant over a simulation time step. The finite difference approach allows for the coefficients to be redefined at each time step.

The finite difference solution consists of the general solutions for n_s and n_p as a function of the rates and the eigenvalues, $\lambda_{1,2}$, for the above system of equations. Below, k is the time index, and Δt is the simulation time step.

$$\frac{n_{s,k+1} - n_{s,k}}{\phi} = -\alpha n_{s,k} + R_s n_{p,k} \quad \text{where} \quad \phi = \frac{e^{\lambda_1 \Delta t} - e^{\lambda_2 \Delta t}}{\lambda_1 - \lambda_2} \tag{4.21}$$

$$\frac{n_{p,k+1} - \psi n_{p,k}}{\phi} = R_p n_{p,k} \quad \text{where } \psi = \frac{\lambda_1 e^{\lambda_2 \Delta t} - \lambda_2 e^{\lambda_1 \Delta t}}{\lambda_1 - \lambda_2} \tag{4.22}$$

$$\lambda_{1,2} = \frac{(R_p - \alpha) \pm \sqrt{(\alpha - R_p)^2 + 4(\alpha R_p)}}{2} \tag{4.23}$$

In comparison with the formula given by *Mickens* [2000], pages 9-10, the coefficients are replaced by rates as follows: $a=-\alpha$, $b=R_s$, $c=0$, and $d=R_p$.

4.2.3 Local Conductivity

The conductivity is governed by the presence of the free low-energy, secondary, electrons. It is calculated using the relation

$$\sigma = \frac{n_s e^2}{m_e v_c}. \tag{4.24}$$

Above, v_c is the collision frequency of the low-energy electrons with neutral molecules. As mentioned above, this is assumed to be independent of the electric-field strength.

The relaxation time, τ, is the inverse of the conductivity times the permittivity of free space, ε_0. And the local electric field is updated using

$$E(t) = E(t - \Delta t) \cdot e^{-\Delta t / \tau} . \tag{4.25}$$

Thus, the electric field is reduced at a faster rate as secondary electron density increases and the relaxation time decreases.

4.2.4 Avalanche Radius

The radius of the electron beam as a function of time is important to know for any avalanche simulation. This is especially important for the 1-D approximation to the avalanche used here. The radius of the beam determines the volume of the beam, and for the one-dimensional model this is $dz \cdot \pi \cdot r^2$. In the numerical calculation, the number of particles in the avalanche is calculated using the high-energy and low-energy electron production rates. If these particles are allowed to fill a larger volume, then the number density of the electrons is lower. The density of the low-energy electrons controls the conductivity. When the conductivity gets high, the ambient electric field is reduced. However, by letting the electrons occupy a larger volume, the conductivity reaches a critical value to eliminate the electric field later in the simulation. Because of this, the total number of electrons can reach a higher value and result in larger currents and radiated electric fields. The frequency content of the radiation is also dependent upon time variation of the electron densities.

If the electric and magnetic forces of the beam can be neglected, then random walk diffusion can be used to estimate the radius of the avalanche [*Roussel-Dupré et al.*, 1993]. This approximation is valid for application to the phenomena of sprites and jets. However, for lightning the radial dimensions are on the order of centimeters or meters depending on what stage of lightning, or what section of a lightning channel, is under investigation.

The radial distribution of the beam electron density is considered here to be uniform. A widely used radial density profile in beam physics is called the Bennett profile. This is the profile for which the thermal and magnetic pressures of the beam are exactly balanced at every radial position. This applies to situations in which the beam is traveling within plasma and the space charge electric field of the beam can be assumed to be eliminated by the plasma. In the following expression, $n(r)$ is the electron density as a function of radius, r_o is the scaling radius, and n_o is the density on the axis [*Humphries*, 1990].

$$n(r) = \frac{n_o}{\left[1+(r/r_o)^2\right]^2} \tag{4.26}$$

For the avalanches considered here, the high-energy electrons produce a background density of low-energy electrons that outnumber the high-energy electrons by a factor of about 10^5. Because of this, the assumption that the low-energy electrons eliminate the space charge field of the beam is at least plausible. Equation (4.26) only gives the radial density profile for beam stability. Note that r_o is the radius at which the beam density falls off by a factor of 4. This value can be estimated for the peak density of the electron avalanche iteratively. The total current, I_o, of the beam is given by

$$I_o = \int_0^\infty 2\pi\, r\, n(r)\, dr\ . \tag{4.27}$$

Substituting in the Bennett stability condition, equation 4.27, one yields

$$I_o = \left(\pi\, r_o^2\right)\cdot e n_o \beta\, c\,. \tag{4.28}$$

Above, e is the electron charge, and βc is the speed of the relativistic electrons. An alternative form of the Bennett stability condition is

$$kT = I_o e\beta\, c\mu_o / 8\pi\,. \tag{4.29}$$

Here, kT is the transverse kinetic energy of the beam and μ_o is the permeability of free space and has a value of $4\cdot\pi\times10^{-7}$ (N/A^2).

For application to the 1-D model, the transverse energy of the beam is obtained from the high-energy electron energy distribution function. The average energy at which freed electrons are ejected transverse to the direction of motion is

$$\langle \varepsilon_p \rangle = \frac{\int_{\varepsilon_{min}}^{\varepsilon_{max}} f(\varepsilon, \cos(\pi/2)) \cdot \varepsilon \, d\varepsilon}{\int_{\varepsilon_{min}}^{\varepsilon_{max}} f(\varepsilon, \cos(\pi/2)) \, d\varepsilon}. \tag{4.30}$$

Electron energies that are represented in the energy distribution function have angle-dependent weights associated with them. These weights are a weak function of the ambient electric field. In the next chapter, 3 different thunderstorm charge configurations are presented in which only the magnitude of the charge varies. For the maximum value of ambient electric field the average energy for an ejection angle of 90 degrees is computed. This energy is used in Eq (4.29) to calculate the maximum expected current. A putative value of r_o was calculated using Eq (4.28) and the simulation was carried out to test whether the expected peak current value was achieved. After iterating to find the optimal value of r_o, it was found that a value of 0.5 m predicts the maximum current values within an order of magnitude for all 3 cases. The radius depends on the square root of the transverse energy, which is a rather weak functional dependence. This is a reasonable approximation since it is in rough agreement with observations of lightning. For example an approximate radius for the conductive core of a stepped-leader channel has been estimated to be 0.175 m by *Orville* [1968] based on his observations. The central core of the stepped leader is believed to be surrounded by a charge-holding envelope that has a radius of several meters [*Uman*, 1987]. Note that the envelope may contain secondary electrons. It is not necessarily appropriate to compare the radius of a stepped leader with the radius of a runaway electron avalanche. This comparison is made, however, because both processes are associated with the breakdown of air, both propagate with high instantaneous speed, and both are believed to produce VHF signals and X-radiation. Clearly, the beam radius should be analyzed in more detail in future investigations.

4.3 Ambient Field Model and Example

In the next chapter, three examples of runaway avalanches are presented in which only the total thunderstorm charge is varied. In these three cases, the thunderstorm charge is spherically symmetric and uniform. The charges have 500-m radii and their centers are separated by 2 km. In each case a high-energy electron is taken to have a velocity anti-parallel to the ambient electric field and has an initial position 300 m above the negative charge center. This initial primary electron density is modeled to have a Gaussian spread on the z-axis as explained above.

The heights and vertical separations of the negative and positive charge centers were chosen to approximate those in real storms. For example, reported values of positive charge center heights range from 4.6 to 10 km. Negative charge center altitudes range from 1-6 km with most observers reporting 3 or 5 km [*MacGorman and Rust*, 1998]. The vertical distance over which these charge layers exist is about 1 km [*Uman*, 1987]. Total charge values for the negative layer have been reported between –20 and –340 C. For the positive charge layer, the range of values reported for the total charge is 24 to 120 C [*MacGorman and Rust*, 1998]. Typical charge density values are less than or equal to about 10 nC/m^3 [*MacGorman and Rust*, 1998]. *Smith* [1998] approximated the charge densities needed for the production of NBP signals. These values are also higher than typical charge densities and, for example, *Smith* [1998] derives 93nC/m^3 for one case. The charge densities used here are higher than typical values, but they are needed to get significant radiation. One may conclude that either the process considered here is not realistic, or the storms producing NBP signals have unusually high charge densities.

In Figure (4.4) a snapshot of three variables along the propagation axis is shown for a run in which ±30-C positive and negative charge regions exist in the thunderstorm.

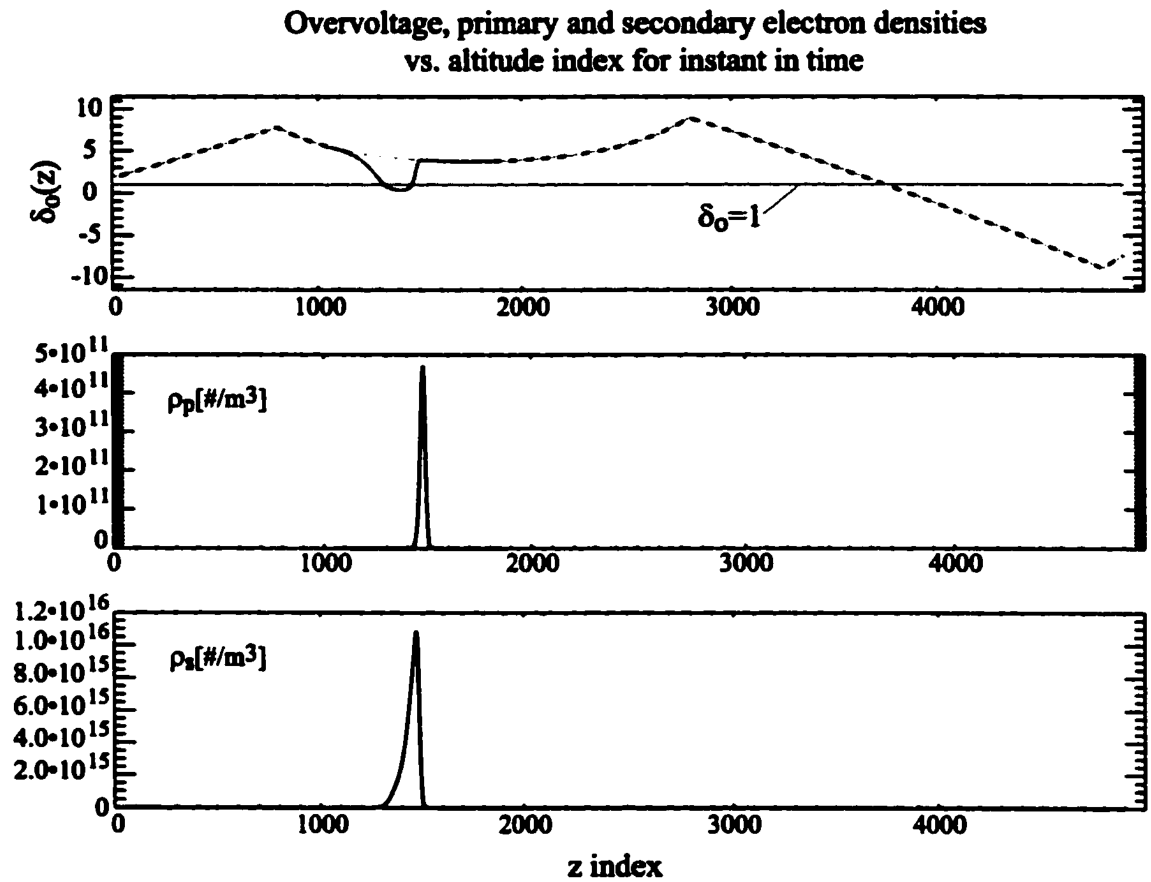

Figure 4.4 All quantities are plotted as a function of altitude index. Top: Ambient electric field divided by threshold electric field for runaway breakdown. Middle: Primary electron density [#/m^3]. Bottom: Secondary electron density [#/m^3].

In the top plot of Figure 4.4 the initial altitude-dependent δ_0 profile is shown as a dotted line. This is the electrostatic field created by two spheres. A negatively charged sphere is centered at z index –200, which corresponds to an altitude of 4.5 km. A positive charge is centered at 6.5 km, which corresponds to an index of 3800. Here each index increment corresponds to 0.5 m. Notice the electric field along the z axis is altered from its initial value and δ_0 drops below 1. This is because the secondary electron density (bottom plot) has increased the conductivity along the z axis.

The second plot in Figure 4.4 shows the evolved primary electron density along the z axis at this instant. Above it was mentioned that the initial primary electron density is modeled as a Gaussian profile. If one considers a frame of reference that travels along with the high-energy electron group, the peak density has shifted forward from its initial position. This is because the ambient electric field near the front of the beam is higher than the field within the beam, and the production rate of electrons is also higher near the front of the avalanche at this instant in time. In the bottom plot, the low-energy electron density is shown. These electrons are assumed to remain in the cell that they are "born" in. Because of this, the axial distribution of the secondary electron density is broader than that for the primary electrons.

Chapter 5

Results

In the previous chapter, a numerical method for computing the electric radiation fields from a discrete set of current values on a space and time grid was presented. In addition, a one-dimensional model of a relativistic electron avalanche was discussed. Runaway avalanches and their radiated electric fields are presented here for three cases in which the total thunderstorm charge is varied. The thunderstorm charge is allowed to be ±10, ±20 and ±30 C. The corresponding charge densities, peak ambient electric fields, and avalanche overvoltages are presented in Table 5.1.

	Case 1	Case 2	Case 3
Charge in spheres (C)	±10	±20	±30
Charge density of positive and negative charge regions (nC/m^3)	19.1	38.2	57.3
Maximum ambient E (V/m)	4.0×10^5	8.0×10^5	1.2×10^6
Overvoltage range (δ_o)	-3.0 to 3.0	-5.9 to 6.0	-8.9 to 9.0

Table 5.1 Physical parameters for the three thunderstorm charge models under consideration.

In each of the three cases, the results are presented by means of five figures that summarize the time histories of the changing physical quantities in the avalanche models and the radiated electric fields. The ambient electric fields, production and loss rates, and densities of particles during the avalanche are plotted for only one point of the electron density wave as a function of time. This point on the electron density wave was chosen as follows. The initial distribution of the relativistic electron density is modeled as a Gaussian function along the z-axis. This Gaussian has an initial peak at some distance z_o. The electron density at this initial position travels along the z-axis with speed βc, evolving along the way. In the following plots, time is plotted along the lower horizontal axes and is related to location along the z-axis by $t=(z-z_o)/\beta c$. Altitude in the thunderstorm, z, corresponding to the travel time, is plotted along the upper horizontal axes.

5.1 Case 1: ±10 C in Thunderstorm

In Figure 5.1 the top plot shows that the ambient static electric field, from this ±10 C of charge, is a substantial fraction of 5×10^5 (V/m) for much of the path covered by the avalanche. This is a strong field in comparison with the typical measured range of 1-8×10^4 (V/m) for thunderstorms [*Uman*, 1987]. Typical high values have been reported to range from 1.4 to 8×10^5 (V/m). All of the field values for this ±10-C case are about 4×10^5 (V/m) or less. The middle plot in Figure 5.1 is δ_0, the ratio of the actual ambient electric field to that required for runaway ionization processes to occur. Note that the ambient electric field can be divided by the electric field required to maintain the electron energy or by the electric field required for avalanche ionization. The maximum value of δ_0 is at the lower edge of the positive charge region. The bottom plot in Figure 5.1 shows the relaxation time, ε_o/σ, as a function of time. The ambient relaxation time is assumed to decrease exponentially from its value at 10 km [*Hale et al.*, 1981] with decreasing altitude. The conductivity and relaxation time do not change significantly because of the presence of the electron avalanche.

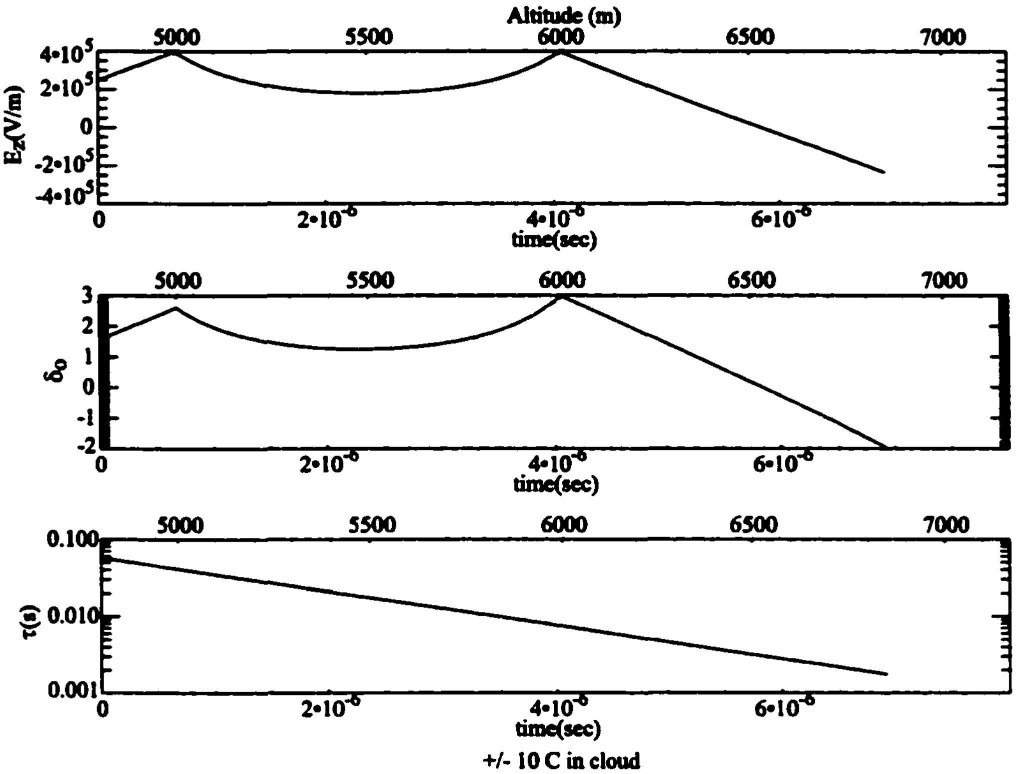

Figure 5.1. ±10 C case: All quantities are on the z-axis. Top plot: Vertical ambient electric field (Ez). Middle plot: δ_o, vertical ambient electric field (Ez) divided by electric field required for avalanche ionization. Bottom plot: Relaxation time of the atmosphere (s). In all plots time=$(z - z_o)/\beta c$.

Figure 5.2 shows the rates of production and loss of primary electrons, production of secondary electrons, and attachment of secondary electrons in the avalanche. The production rate of high-energy, or primary, electrons, R_p, has a maximum value of over 5 million per second where the ambient value of electric field over pressure, *E/p*, is optimal. Toward the end of the avalanche, above the positive charge center, the absolute value of the primary electron loss rate is about 1.28×10^7(1/s). The high-energy electrons are modeled to be subtracted from the beam and convert their energy to the production of low energy electrons. Above the positive charge center, collisions of the high-energy electrons with air no longer result in the newly-ionized electrons gaining energy from the electric field and becoming runaway electrons.

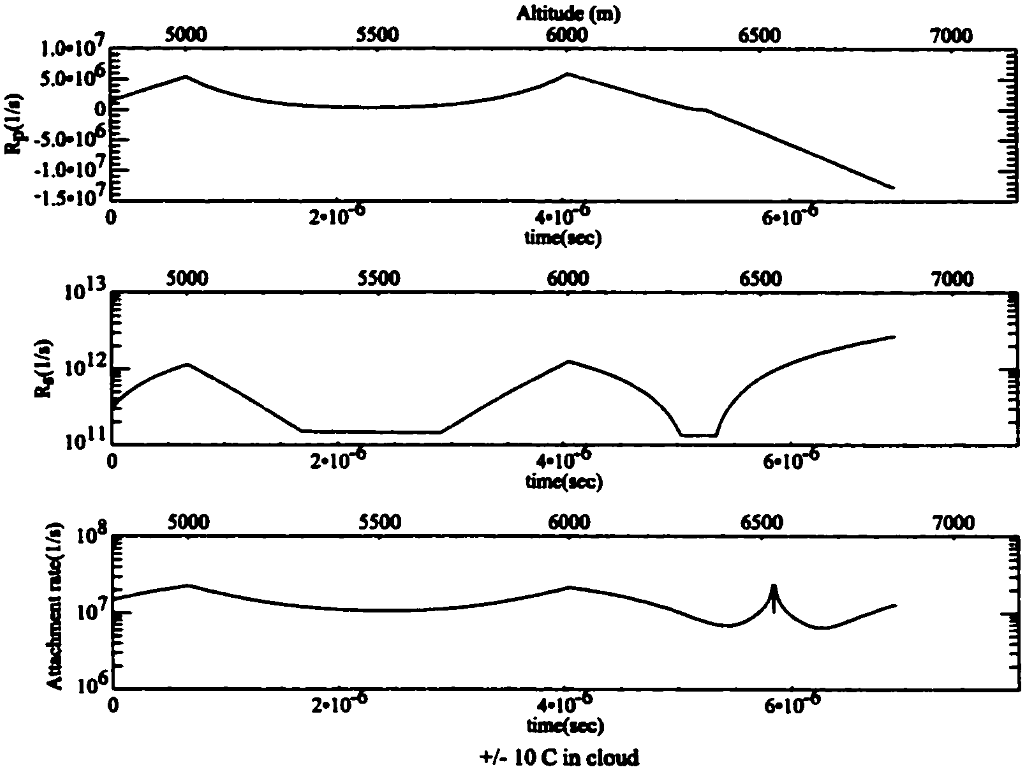

Figure 5.2. ±10 C case: Top plot: Primary electron production rate (1/s). Middle plot: Secondary electron production rate (1/s). Bottom plot: secondary electron attachment rate (1/s)

The low-energy electron production rate is shown on a logarithmic scale in the middle plot. R_s is proportional to the primary electron ionization rate in regions where the high-energy electrons gain energy from the ambient electric field. Note that as the primary production rate goes to zero, the secondary production rate maintains a minimum positive value. High energy electrons will continue to lose energy through ionization when they encounter a region of low electric field and secondary electrons are produced at the collision rate times an energy factor. The third plot of Figure 5.2 is the attachment rate as a function of altitude or beam travel time. This rate also depends on the ambient electric field and pressure. The attachment rate is low in comparison with the secondary production rate. However, to calculate this low-energy electron sink the attachment rate is multiplied by the low-energy electron density. The production rate, R_s, is multiplied by the primary electron density. Attachment limits the current of the low energy electrons because when they electrically bond with molecules and atoms, the mobility is considered to be insignificant.

In Figure 5.3, the primary and secondary electron densities are shown along with the varying drift velocity of the secondary electrons.

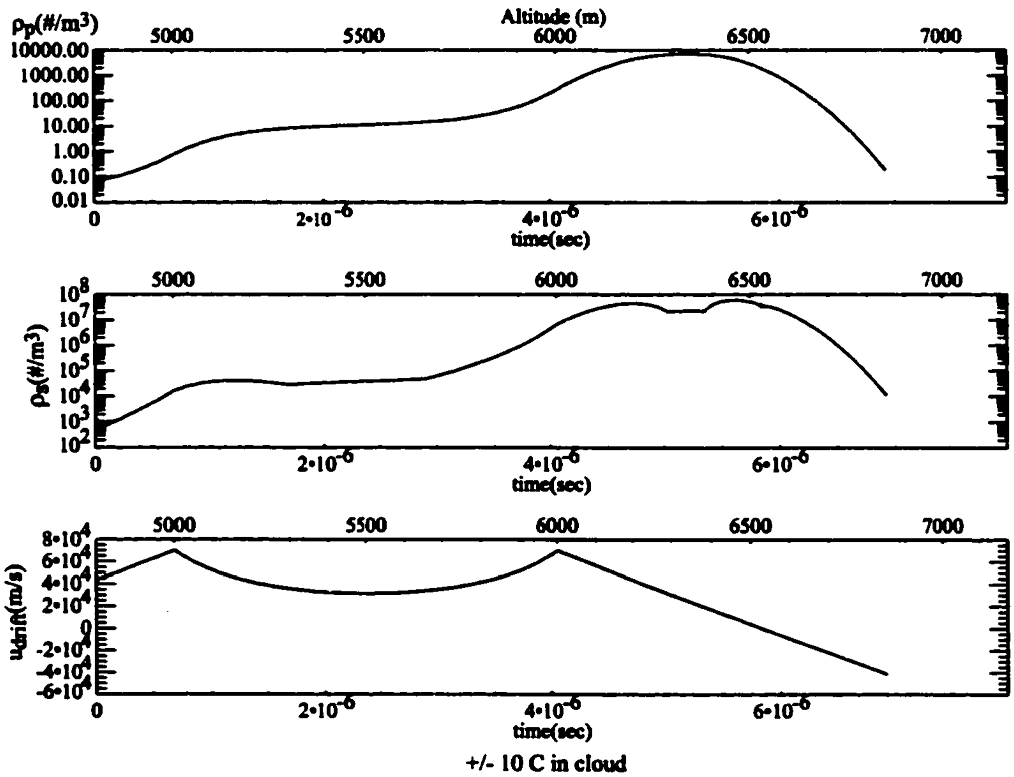

Figure 5.3. ±10 C case: Top plot: Primary electron density (ρ_s [#/m^3]) as a function of beam travel time. Middle plot: Secondary electron density (ρ_s [#/m^3]). Third plot: Drift velocity (m/s) of secondary electrons in ambient electric field.

The primary electron density reaches a maximum of 7.1×10^3/m^3 near an altitude of 6.35 km. The rate of production of these high-energy electrons reaches a maximum near 6.0 km. The primary electron density continues to increase until the production rate becomes zero at $\delta_{o,min}$ or negative in regions where $\delta_o < \delta_{o,min}$. The secondary electron density also reaches a local maximum just after the secondary electron production rate reaches a maximum around 6-km. A second maximum is achieved because of the rapid elimination of the high-energy electrons from the beam. The peak low-energy electron density is $6.1\times10^7/m^3$ near the positive charge center. The bottom plot of Figure 5.3 is the drift velocity of the secondary electrons. The drift velocity is a function of the ambient electric field and the electron mobility and is used to calculate the secondary electron current. Note that when the beam is above the positive charge center, the electrons drift downward instead of upward.

For the thunderstorm modeled with ±10-C spheres of charge the high-energy and low-energy electron densities, and density variations, do not reach levels that can produce substantial current changes and radio emissions (Figure 5.4). The top plot of Figure 5.4 shows the radiation electric-field waveform produced by the primary and secondary electron currents. The time-domain electric field is plotted for a range of 800 km. The peak field at this range and a 12-degree observation angle is about 9.0×10^{-11} (V/m). The significant portion of the electric-field pulse has a total duration of less than 1 μs. The bottom plot shows the Fourier transform of the top plot and it is scaled to have units of power spectral density per unit area. This is a low-amplitude spectrum. The noise that results from imperfectly smooth integration and differentiation in the numerical calculation of the radiation electric field. Above about 50 MHz this noise is approximately 5 orders of magnitude lower than the peak spectral amplitude, and is not clearly visible to the naked eye in the top plot of the following figure.

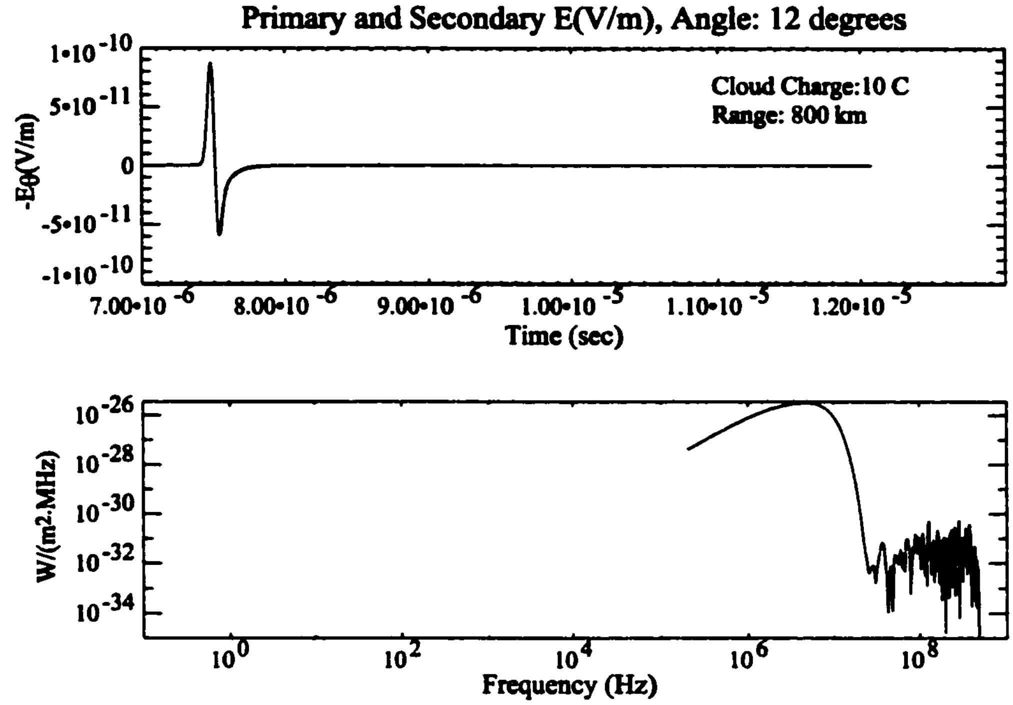

Figure 5.4. ±10 C case: Top plot: Superposition of radiation electric fields from primary and secondary electron currents as viewed from an 800-km range and observation angle of 12 degrees from the direction of beam propagation. Bottom plot: Power spectral density as a function of frequency for the signal in the top plot. This spectrum peaks below 10 MHz and is weak.

Figure 5.5 shows the overall results as a function of observer angle for the 10-C case. The top plot is the correlation of the two signals, from the primary and secondary electrons, as seen at the 800-km observation range. The two signals are calculated using integration to obtain the time-dependent vector potentials and time differentiation to obtain the radiated electric fields, on identical observation-time grids. Thus, the electric-field amplitudes as a function of time for the primary and secondary electrons were treated as two vectors and the phase correlation between these two vectors was calculated. The signals do not correlate perfectly, i.e. correlation coefficient=1, at any angle. The peak correlation occurs at about 20 degrees. The middle plot shows the power spectral density (PSD) per unit area as a function of observer angle for the combined signals in a 26-48-MHz band. The peak PSD occurs for an observation angle near 60 degrees. At this angle the signals do not correlate well, and the noise in the resulting waveform shows up as high frequency radiation in the time domain.

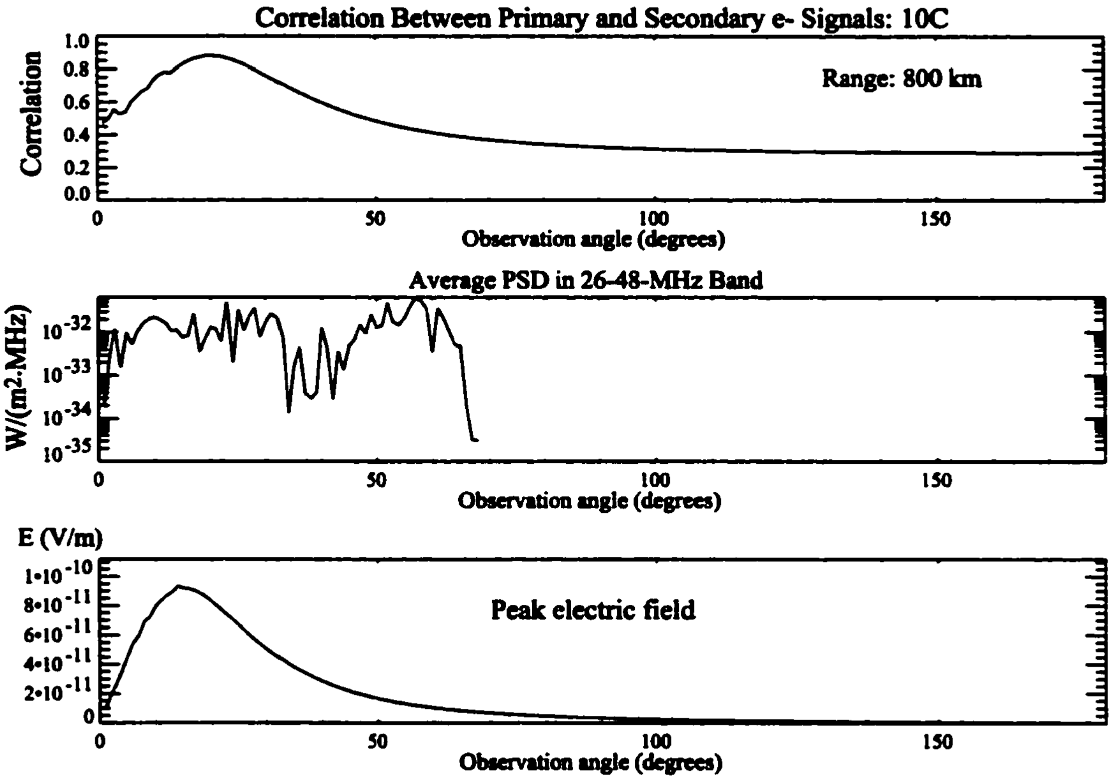

Figure 5.5. ±10 C case: Top plot: Correlation between time-domain electric field signals of primary and secondary electron currents as a function of observer angle. Middle plot: Power spectral density per area as a function of observer angle in a 25-48 MHz band. Zero amplitude values are not included on this logarithmic plot. Bottom plot: Magnitude of peak radiated electric field as a function of observer angle.

The bottom plot in Figure 5.5 shows the amplitude of the peak radiation electric field as a function of observation angle. The highest amplitude peak electric field is seen for an observer near 12-15 degrees from the direction of beam propagation. Near the maximum, the peak field is almost one order of magnitude higher than the peak electric fields observed at 1 degree and 70 degrees. These peak electric field values are much weaker than those recorded for NBPs and scaled to an 800-km range. For the 10-C case, the runaway electron avalanche produces no substantial radio radiation. The results for the 20-C and 30-C cases prove to be more interesting.

5.2 Case 2: ±20 C in Thunderstorm

The ±10 and ±20-C cases were chosen for discussion because the properties of the runaway avalanches occurring in these ambient fields are quite different. When the total charges in each sphere, representing charge layers in a thunderstorm, are doubled the ambient electric field is also doubled because this static electric field is proportional to the charge. As seen in the top plot of Figure 5.6, the initial static electric field for the ±20-C case is in the 0.5-0.8 MV/m range before the ionizing beam increases the conductivity along the z-axis. Thus, for much of the path to be traversed by the avalanching electrons, the electrostatic field lies within the range of values recorded for unusually strong thunderstorm electric fields. From a beam travel time of about 3.5-4 μs, the ambient electric field is reduced to zero along the z-axis. The middle plot of Figure 5.6 shows the corresponding overvoltage. The bottom plot shows the relaxation time as a function of beam travel time or altitude. The relaxation time reaches a minimum of about 10 ns after the beam has traveled for 4 μs. The simulation time step is $\Delta z/\beta c$ with a value of 1.69 ns, which remains smaller than the relaxation time throughout the simulation. Thus, in less than 10 simulation time steps, the ambient electric field is reduced to 1/e of its initial value.

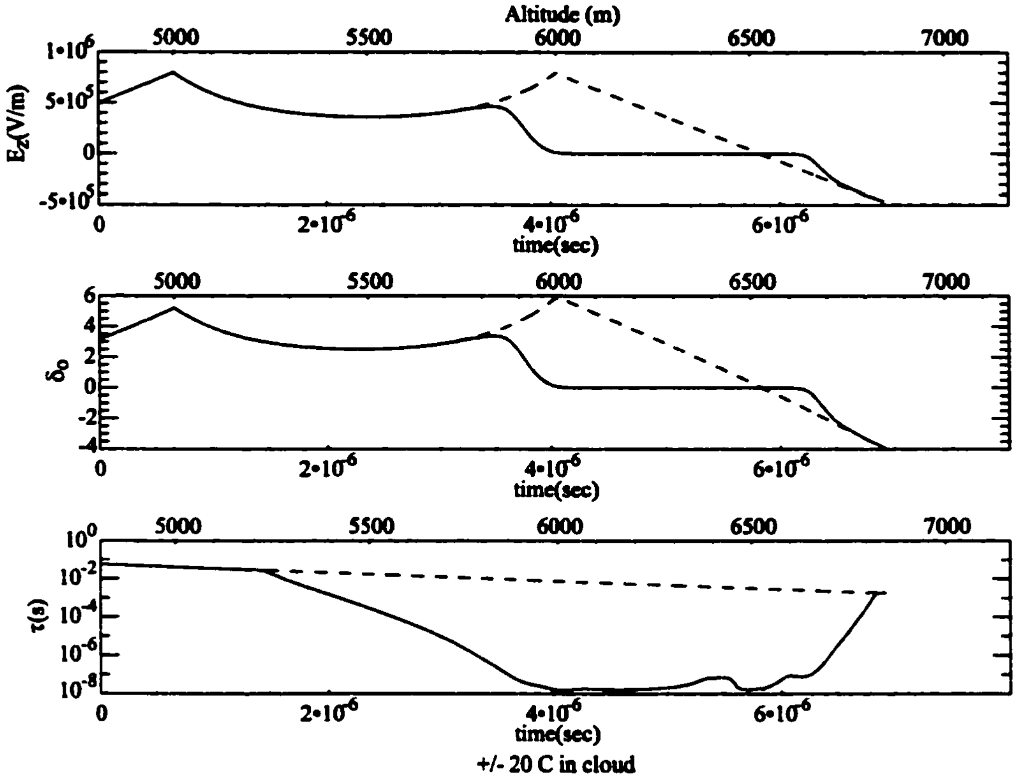

Figure 5.6. ±20 C case: All plotted quantities are along the z-axis. Top plot: Vertical ambient electric field (Ez). Middle plot: δ_o, vertical ambient electric field (Ez) divided by electric field required to accelerate high-energy electrons. Bottom plot: Relaxation time of the atmosphere (s). In all plots time=$(z - z_o)/\beta c$.

Figure 5.7 shows the primary and secondary electron production and loss rates R_p and R_s, respectively, and the secondary electron attachment rate as a function of beam travel time or altitude. The primary electron production rate is initially positive and proportional to the ambient electric-field strength. However, as the relaxation time decreases and the ambient electric field also decreases, the primary production rate goes to zero and then negative for the position followed in the beam. For positions in the beam where the relaxation time remains high, the avalanche continues.

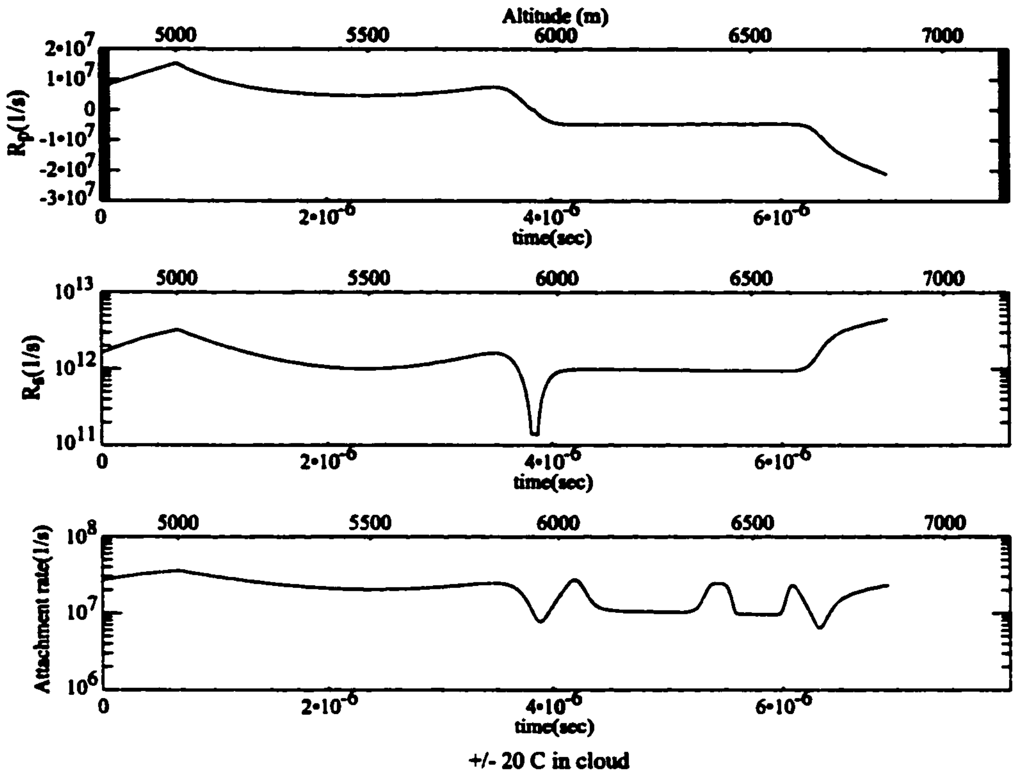

Figure 5.7. ±20 C case: Top plot: Primary electron production rate (1/s). Middle plot: Secondary electron production rate (1/s). Third plot: secondary electron attachment rate (1/s)

When the primary electron production rate is near zero, top plot of Figure 5.7, the secondary electron production rate defaults to the collision rate times the energy factor of 7.2 MeV / 34 eV. This situation represents the minimum secondary electron production rate shown.

Figure 5.8 shows the electron densities as a function of beam travel time. First notice that the maximum electron densities achieved are about the square of those achieved in the 10-C case. This can be understood qualitatively. The avalanche, or production, rates for both the primary and secondary electrons are roughly proportional to the ambient electric field. Note also that the number density of electrons increases exponentially with avalanche rate. Therefore, by doubling the external field the number density of electrons can be roughly squared. Again, the low-energy electrons dominate the conductivity and relaxation time in this problem. And it is at this value of about $10^{16}/m^3$, as opposed to $10^8/m^3$ in the previous case, that the relaxation time becomes short enough to reduce the ambient electric field and slow the ionization processes of the avalanche. The drift velocity of the low-energy electrons is also shown.

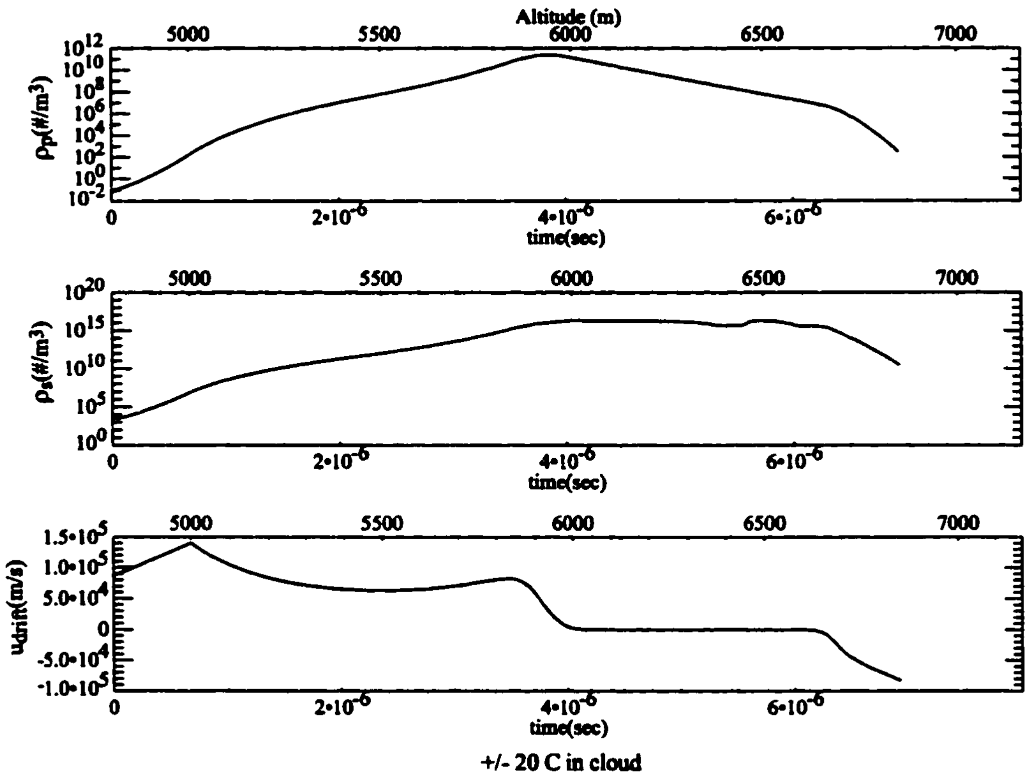

Figure 5.8. ±20 C case: Top plot: Primary electron density (ρ_p [#/m³]) as a function of beam travel time. Middle plot: Secondary electron density (ρ_s [#/m³]). Bottom plot: Drift velocity (m/s) of secondary electrons in ambient electric field.

Unlike the situation in the ±10-C case, the drift velocity is zero over a significant portion of the simulation. This will be reflected in the radiation electric field waveform for the low-energy electrons since and there is zero current, and zero rate of change of current with time, where the velocity and ambient field are zero. The high-energy electrons are carried forward by their momentum until they are subtracted from the avalanche as explained above.

The sum of the radiated waveforms produced by the primary and secondary electron currents is shown in Figure 5.9 for an observation angle of 12°.

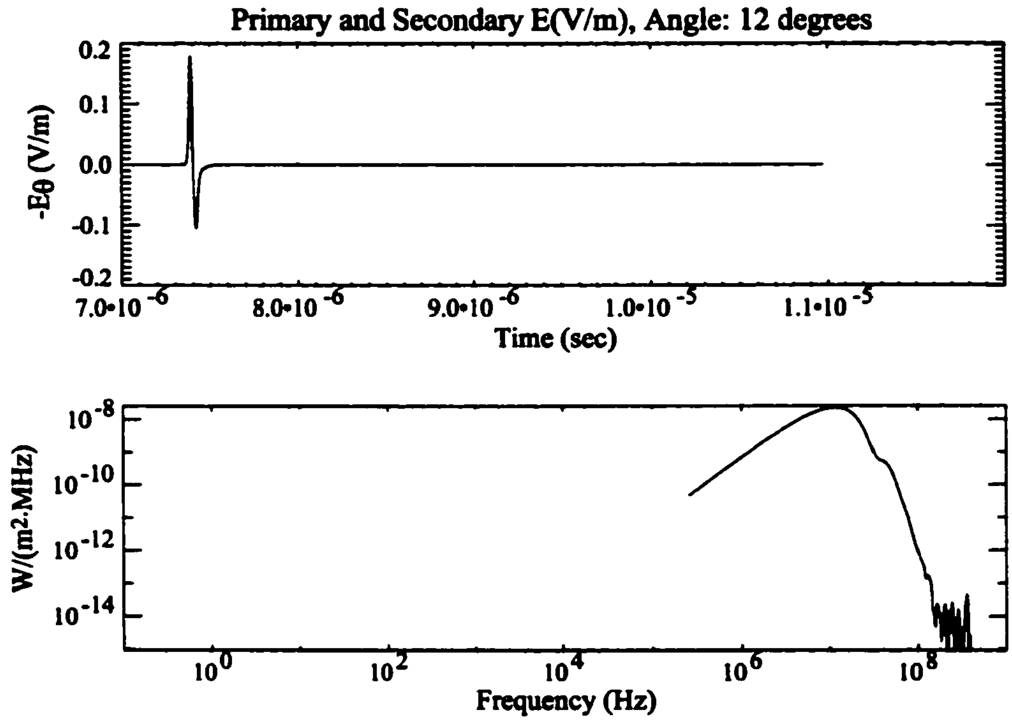

Figure 5.9. ±20 C case: Top plot: Superposition of radiation electric fields from primary and secondary electron currents as viewed from an 800-km range and observation angle of 12 degrees from the direction of beam propagation. Bottom plot: Power spectral density as a function of frequency for the signal in the top plot.

This electric field is calculated for an 800-km range. A peak E-field of about 0.2 V/m at an 800-km range corresponds to a peak E-field of about 1.6 V/m at a 100-km range. In contrast with the previous case, this value is much closer to the mean peak field, e.g. 8.0±5.3 V/m [*Willett et al.*, 1989], recorded for the NBP signals. And the overall duration of waveform produced by the electron avalanche by itself is clearly shorter than the 20-μs

NBP waveforms. The current hypothesis is that the runaway electron avalanche might, in part, represent the rise time and peak electric field associated with the NBP signals, and this is why the peak electric fields are of interest.

The bottom plot of Figure 5.9 shows the PSD per unit area. The peak is at a higher frequency than the ±10-C case. Here the PSD is a maximum near 10 MHz. This PSD per unit area is within the low end of the overall range of observations made by FORTE as shown in Figure 5.17 near the end of this chapter.

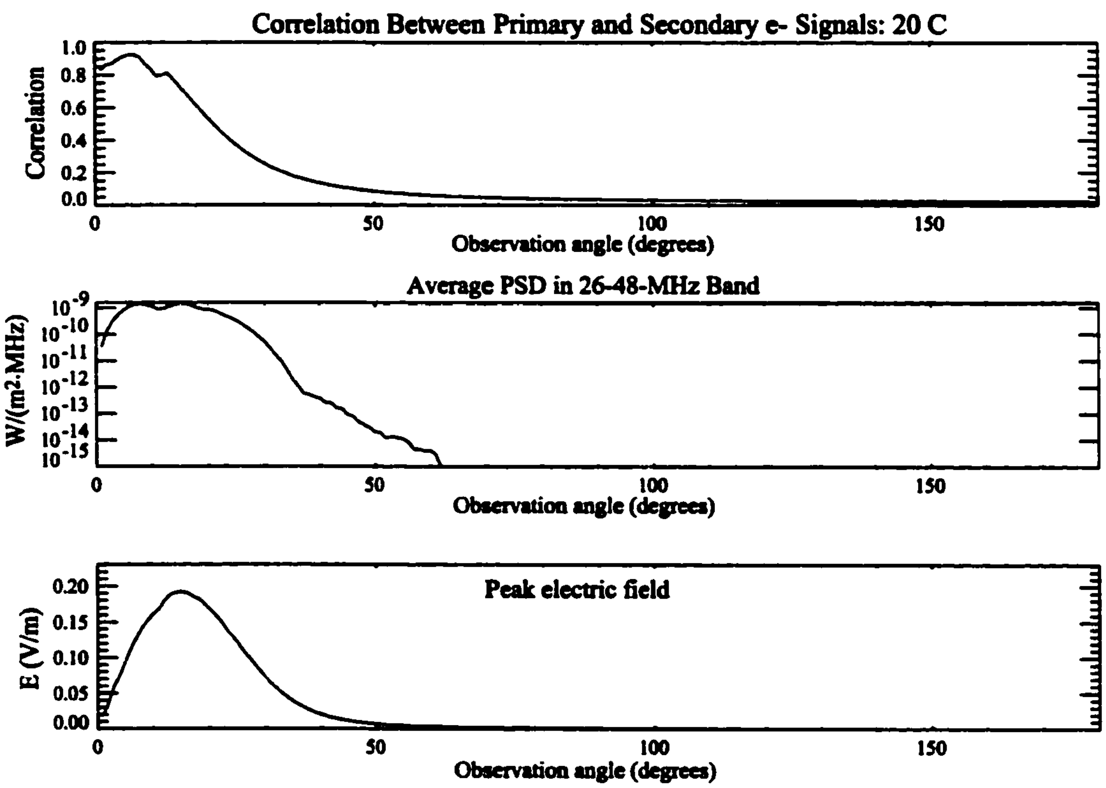

Figure 5.10. ±20 C case: Top plot: Correlation between time-domain electric field signals of primary and secondary electron currents as a function of observer angle. Middle plot: Power spectral density per unit area as a function of observer angle in a 25-48 MHz band. Zero amplitude values are not included on this logarithmic plot. Bottom plot: Magnitude of peak radiated electric field as a function of observer angle.

Figure 5.10 shows the correlation between the primary and secondary electron radiation electric fields for an 800-km range. The overall correlation is lower than in the

±10-C case. This is in part because the secondary electron current changes less continuously than it did in the previous case and is zero in some locations. This results in a noisier waveform for the secondary electrons. The first energy to arrive at the antenna in this case is associated with the rise time of the avalanche and this occurs before the ambient electric field is reduced to zero. The middle plot shows the PSD radiated per unit area as a function of observation angle. These values are within the range recorded by FORTE from about a few to thirty degrees. The bottom plot shows the magnitude of the peak electric field as a function of observation angle. The peak field is near, but below, peak electric field values reported by *Willett et al.* [1989] as discussed above. The relatively strong peak electric field values would be observed at angles where the VHF PSD per unit area is also high, as in observations of NBPs.

5.3 Case 3: ±30 C in Thunderstorm

The results for the ±30-C case improve upon the previous cases in terms of comparison with observations. Consider the top and middle plots of Figure 5.11. The ambient electric field within the beam is eliminated after the beam has traveled for only about 2 μs. This corresponds to a distance of approximately 700 m. The initial ambient electric field (dashed line) is above 1 MV/m for some locations between the two charge centers. The relaxation time of the beam is again about 10 ns for much of the time, at the location in the beam that is plotted, but it reaches this low value sooner than in the ±20-C case.

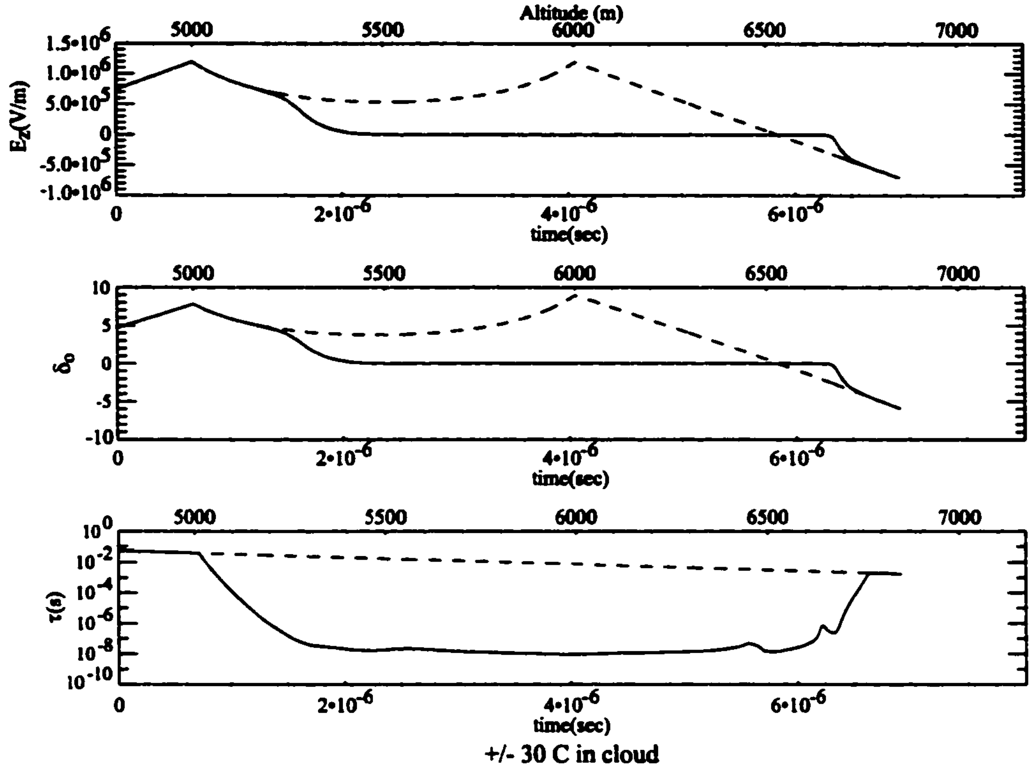

Figure 5.11. ±30 C case: All quantities are on the z-axis. Top plot: Vertical ambient electric field (Ez). Middle plot: δ_o, vertical ambient electric field (Ez) divided by electric field required to accelerate high-energy electrons. Bottom plot: Relaxation time of the atmosphere (s). In all plots time=$(z - z_o)/\beta c$.

Figure 5.12 shows the avalanche and loss rates for the primary and secondary electrons and the attachment rate for the secondary electrons. The primary electron production rate is higher for a shorter period of time as compared with the previous cases. Because of this, the electron currents will reach their maximum values in a relatively shorter period of time. This acts to increase the VHF content of the radiated electric-field waveform, in comparison with the previous two cases. The secondary electron production rate also has an initial peak before the ambient electric field is reduced, and a second peak when the high-energy electrons are removed from the beam where the ambient field is parallel to the direction of electron motion. The subtraction of the high-energy electrons from the avalanche occurs relatively quickly in this case compared with the other cases because the "decelerating" electric field above the positive charge region is stronger than in the previous cases.

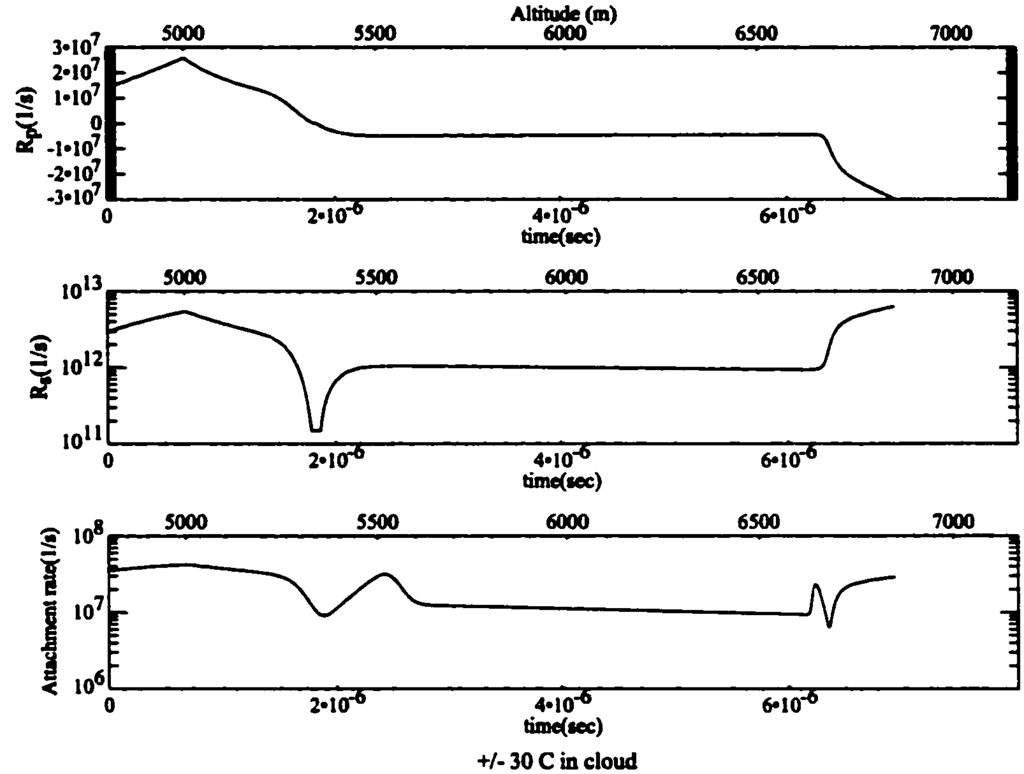

Figure 5.12. ±30 C case: Top plot: Primary electron production rate (1/s). Middle plot: Secondary electron production rate (1/s). Bottom plot: secondary electron attachment rate (1/s).

Consider Figure 5.13. When the thunderstorm field is tripled, as compared with the ±10-C case, the maximum number density of the beam is not proportional to the cube of the ambient electric field strength. There is a limit to the maximum attainable electron density, and the ±20 and ±30-C thunderstorms were chosen to demonstrate this fact. Comparison of Figure 5.13 to Figure 5.8 shows that the maximum number densities are quite close. The conductivity limits the electron density of the avalanche. The maximum low-energy electron density is of the order $10^{16}/m^3$, and the maximum high-energy electron density is between 10^{11} and $10^{12}/m^3$.

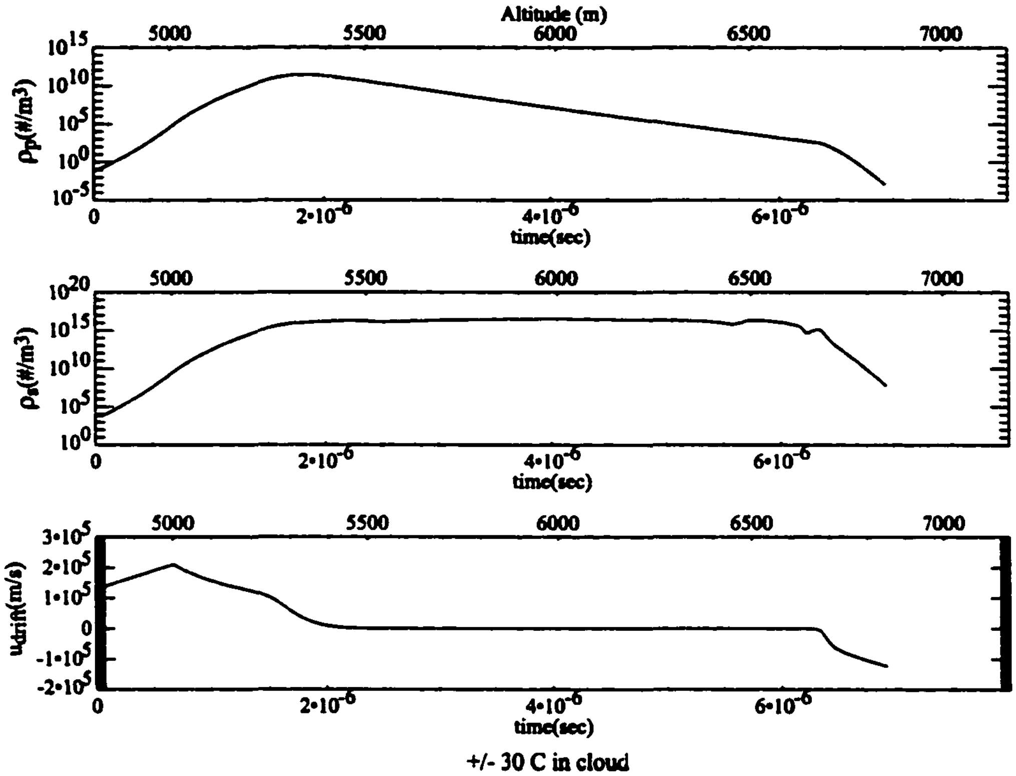

Figure 5.13. ±30 C case: Top plot: Primary electron density (ρ_p [#/m³]) as a function of beam travel time. Middle plot: Secondary electron density (ρ_s [#/m³]). Bottom plot: Drift velocity (m/s) of secondary electrons in ambient electric field.

Figure 5.14 shows the radiated electric field waveform and spectral amplitude for the ±30 C case for an observation angle of 12 degrees and 800-km observation range. The peak electric field shown in the top plot happens to be very close to the mean of the peak electric fields obtained observationally for NBPs, when scaled the same range. The spectral amplitude is stronger than that shown in the previous cases for this observation angle. In addition, the peak spectral amplitude is shifted to a higher frequency than in the previous cases. Here the peak PSD per unit area is about 10^{-7}[W/(m^2·MHz)], and this peak occurs above 10 MHz.

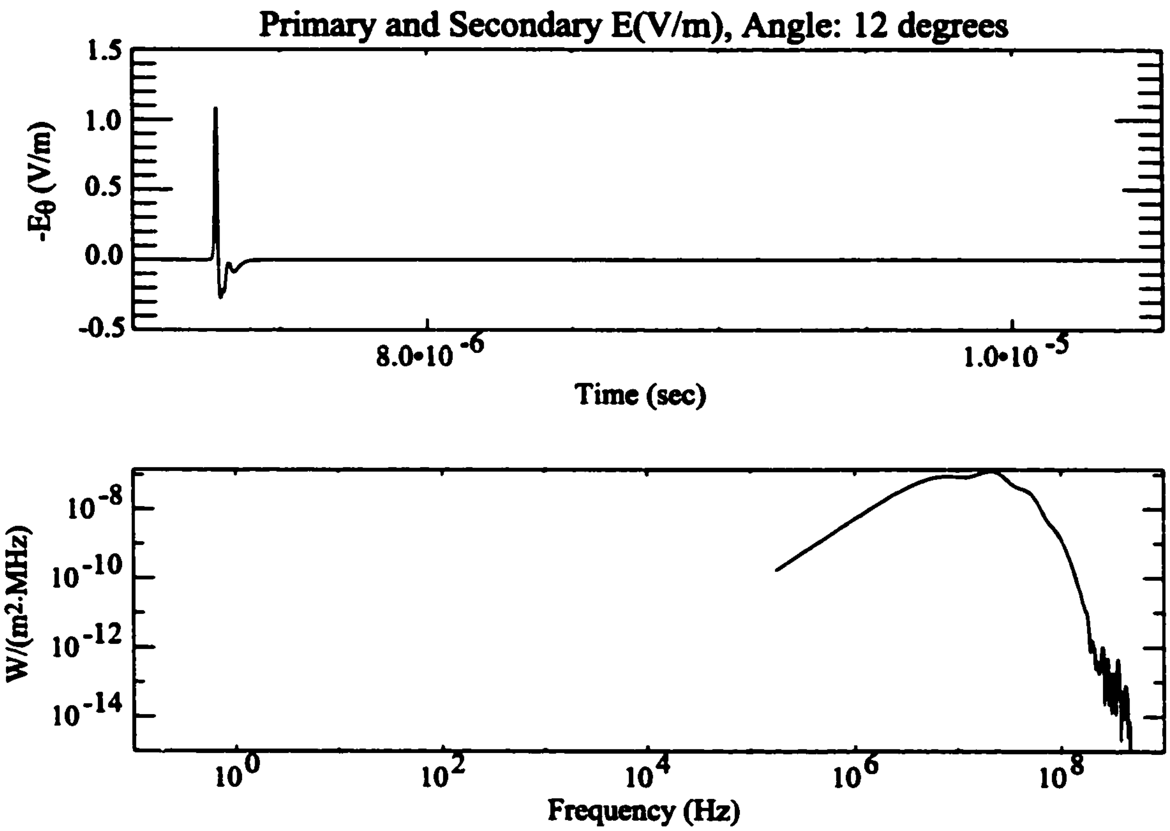

Figure 5.14. ±30 C case: Top plot: Superposition of radiation electric fields from primary and secondary electron currents as viewed from an 800-km range and observation angle of 12 degrees from the direction of beam propagation. Bottom plot: Power spectral density per unit area as a function of frequency for the signal in the top plot. This spectrum peaks above 10 MHz.

Figure 5.15 shows the overall results for the 30-C case as a function of observation angle. The correlation is high at small observation angles and falls below zero for large observation angles. The PSD per unit area is above 10^{-8} W/(m^2·MHz) for observation angles of 5 to about 22 degrees. The magnitude of the peak electric field is above 1 V/m from about 10 to 20 degrees at this 800-km range.

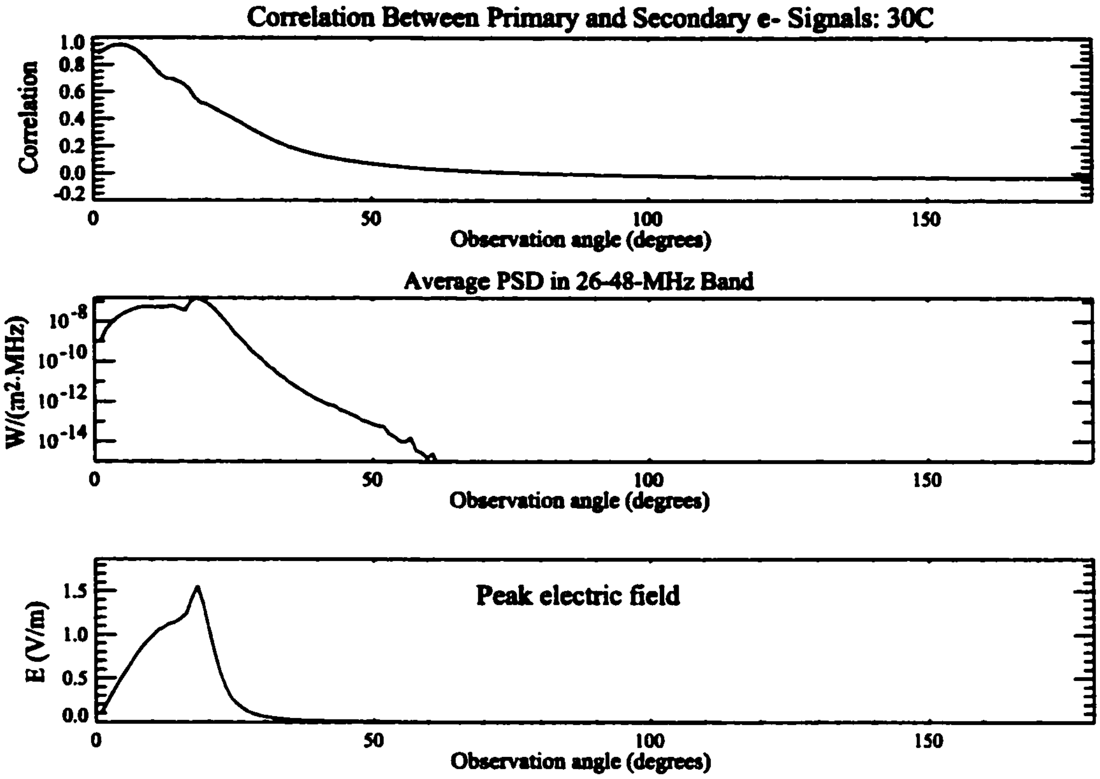

Figure 5.15. ±30 C case: Top plot: Correlation between time-domain electric field signals of primary and secondary electron currents as a function of observer angle. Middle plot: Power spectral density per area as a function of observer angle in a 25-48 MHz band. Zero amplitude values are not included on this logarithmic plot. Bottom plot: Magnitude of peak radiated electric field as a function of observer angle.

5.4 Intensity as a Function of Observer Angle: 10, 20, and 30-C Cases

The peak electric-field amplitudes and spectral amplitudes from the avalanches occurring in the 10, 20, and 30-C storms are now summarized and compared with observations. First the models are compared with frequency domain electric-field observations that have been scaled to a 10-km range, and 1-kHz bandwidth. The first three figures in this section are ordered based on the frequency range that they correspond to. Figure 5.16 shows the calculated and observed values of peak electric field (mV/m) for the HF band of 3-25 MHz.

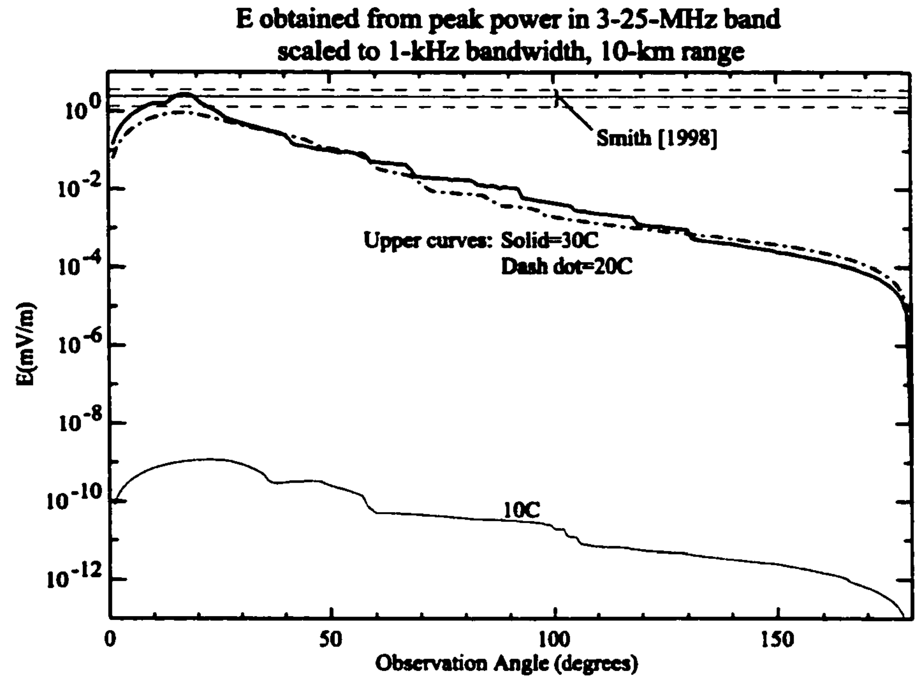

Figure 5.16. Scaled peak electric field amplitude in a HF band covering 3-25 MHz. The mean value and standard deviations of 2.4±1.1 (mV/m) reported by *Smith* [1998] are shown as horizontal solid and dashed lines, respectively.

The mean value and standard deviations of 2.4±1.1 (mV/m) reported by *Smith* [1998] are shown as horizontal solid and dashed lines, respectively. The lines corresponding to these amplitudes are drawn as if they are independent of angle because the angular dependence of the observed radiation is not reported or known. The peak spectral intensity in the 3-25 MHz range was also calculated for the avalanches occurring in the three thunderstorm models discussed above and was scaled to a 1-kHz bandwidth, 10-km range, and electric-field units of mV/m. For the ±30-C case the electric field radiated by the runaway avalanche falls within one standard deviation of the reported mean for observation angles lying within ±8 to 22 degrees from the propagation direction. For the ±20-C case, the peak electric field radiated in the 3-25 MHz band is below one standard deviation of the reported mean.

The VHF radiation in the band of 26-48 MHz, representing the FORTE low band, is plotted as a function of observation angle in Figure 5.17. For the FORTE data, a histogram of source powers was given (Figure 2.5). These source powers have been scaied to a 10-km range and a 1-kHz bandwidth, and converted to frequency domain electric-field values.

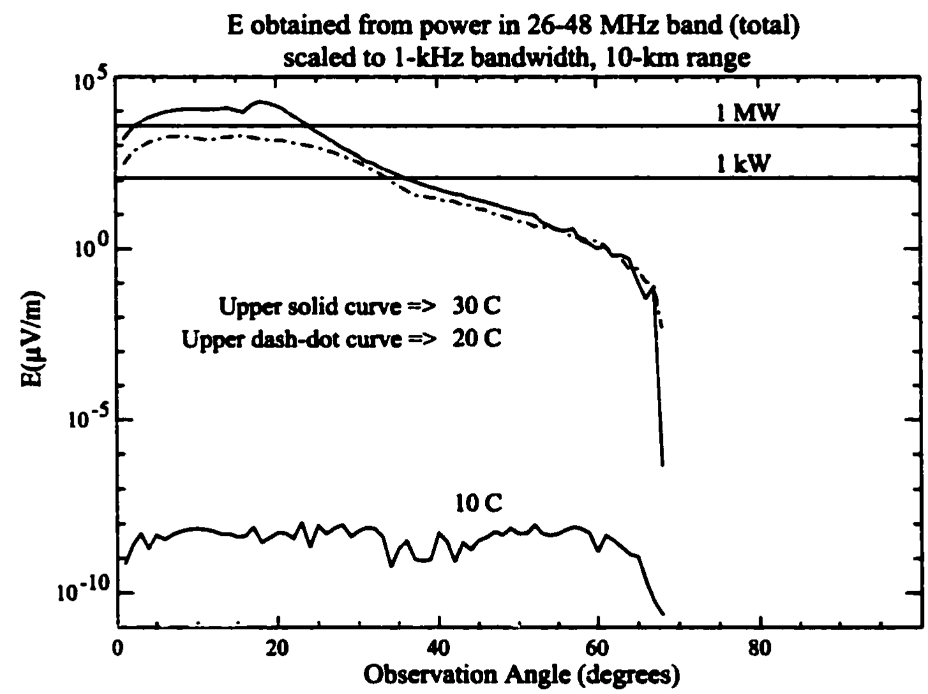

Figure 5.17 Scaled peak electric field amplitude in a VHF band covering 26-48 MHz. The electric field values corresponding to band-totaled source powers of 1 kW and 1 MW are shown as horizontal lines.

The source power values of 1 kW to 1 MW are drawn, after being scaled and converted to μV/m, as horizontal lines. The source powers reported for the FORTE data represent the *total* power in the 26-48 MHz band. Thus, the powers in this frequency range radiated by the model avalanches were also band summed (black curves). See section 2.1.3 for further discussion on scaling power and converting to electric field. As in the previous case, the avalanche occurring in the ±10-C environment doesn't produce any appreciable radiation in this frequency range. The avalanches for the ±20 and ±30 C cases easily fall within the range of values observed by FORTE for a limited angular range. This observation-angle range is, however, significantly broader than the angular range within which the modeled HF electric field amplitudes agree well with the data as shown in Figure 5.16. The radio radiation from the 30-C case falls within the given range for observation angles of 1 to more than 35 degrees.

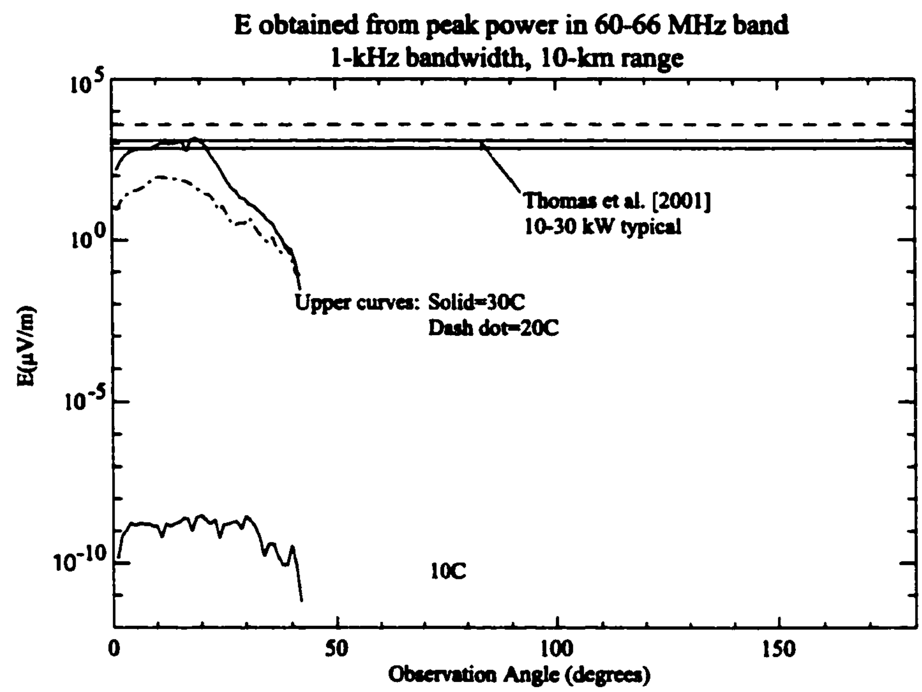

Figure 5.18 Scaled peak electric-field amplitude in a VHF band covering 60-66 MHz. The electric field values corresponding to peak source powers of 10 and 30kW are shown as solid horizontal lines. The dashed line corresponds to an event with 300 kW source power.

Observations made in the 60-66 MHz range using the LMA are compared with the radio emissions from the modeled electron avalanches. This is shown in Figure 5.18. Peak powers the 60-66 MHz band were used to calculate the LMA source powers reported by *Thomas et al.* [2001], assuming that the electromagnetic radiation was isotropic. Typical peak source powers of 10-30 kW were calculated and two solid straight lines in Figure 5.18 bound this range (scaled and converted to E). The unusually strong 300-kW source power is also scaled and converted to E(μV/m) and is shown as a dashed line. For this frequency range, only the runaway electron avalanche of the ±30-C storm falls within the 10-30 kW range for observation angles of about 5 to about 22 degrees. The 300-kW event is not explained by the model avalanches considered here.

Figure 5.19 shows the absolute value of the peak radiation electric field (time-domain) as a function of observation angle for the three cases presented here.

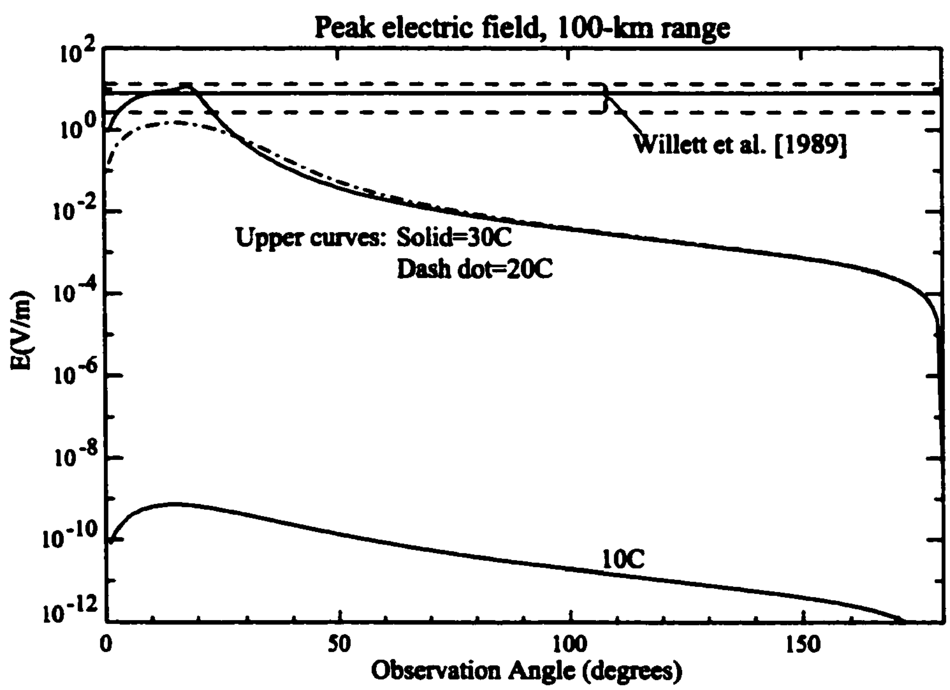

Figure 5.19 The mean peak E-field for 18 NPBPs observed by *Willett et al.* [1989] is 8.0±5.3 V/m. This is drawn for comparison as a solid line with equal amplitude at all angles. The standard deviations are drawn as dashed lines.

The mean value and standard deviations reported by *Willett et al.* [1989] for the NBP signals are shown as solid and dashed lines, respectively. The angles at which the peak radiation electric fields are measured correspond to the angles of maximum VHF intensity.

Table 5.2 shows the total source power (26-48 MHz band) and peak time domain electric fields for the avalanches occurring within the three ambient electric field models. The power density $f(R,\theta)$[W/m^2] from the avalanche simulations is known as a function of observation angle. Thus, the total power radiated is calculated without assuming that the power is independent of observation angle. The total power for the ±30-C case is almost half a mega Watt.

	Case 1	Case 2	Case 3
Charge in spheres (C)	±10	±20	±30
Maximum primary avalanche rate (1/s)	1.28×10^7	2.12×10^7	2.97×10^7
Maximum primary electron number density (#/m^3)	7.06×10^3	2.38×10^{11}	2.62×10^{11}
Maximum secondary avalanche rate (1/s)	2.7×10^{12}	4.5×10^{12}	6.29×10^{12}
Maximum secondary electron number density (#/m^3)	6.1×10^7	2.11×10^{16}	3.3×10^{16}
Total power radiated (Watts) in 26-48-MHz band	5.8×10^{-19}	8.2×10^3	4.4×10^5
Peak electric field (V/m)	7.5×10^{-10}	1.5	12.5
Angle of peak E (degrees)	14	15	18

Table 5.2 Power radiated from source (26-48 MHz) and peak radiation electric field for the three thunderstorm charge models considered.

In Figure 5.17 the upper horizontal line is for FORTE events calculated as radiating a total of 1-MW from the source based on band-summed peak power measurements. At some angles the peak power radiated by the model avalanche is higher than that observed by FORTE. Thus, for radiation signals from relativistic processes, the total power may be overestimated or underestimated if the power density is assumed to be radiated isotropically. The percent error will depend upon the angle at which the Poynting flux is sampled. For non-relativistic dipole radiators the assumption that the power radiated is independent of angle is reasonable. Further discussion of the results presented in this chapter is provided in Chapter 6.

Chapter 6

Conclusions and Discussion

6.1 Conclusions

The physics of runaway electron avalanches and associated radio emissions was discussed in Chapters 2 and 4. A simplified version of an existing model of runaway breakdown in thunderstorms was also presented in Chapter 4. Three examples of electron avalanches occurring within different ambient electric fields were presented. Results for the radio emissions from electron avalanches developing in these fields were obtained. Frequency domain electric-field amplitudes have been calculated in three frequency bands corresponding to ground-based and space-based observations. The peak electric fields in the time domain were also calculated because the rise times of runaway electron avalanches may be related to the rise times of NBP signals. From the results of the previous chapter, several conclusions are drawn.

1.) For the HF band of 3-25 MHz, *Smith* [1998] reports a peak amplitude of 2.4±1.1 mV/m, scaled to a 1-kHz bandwidth and 10-km range, for 24 compact intracloud discharges in his study. The modeled electron avalanche occurring within the ±30 C storm falls within this range, but only for observation angles from about 7 to 22 degrees from the direction of propagation.

2.) For the low band, 26-48 MHz, of a receiver onboard FORTE band summed electromagnetic power values were calculated for 400-μs data records. The peak powers radiated from the sources (1kW-1MW) were obtained assuming that the sources were isotropic radiators. Scaling the source powers to a 1-kHz bandwidth and a 10-km range gave the 117 and 3696.3 μV/m values shown in Figure 5.17. For the observation angle range of about ±1-35 degrees, with respect to the propagation direction of the beam, the electric-field amplitudes are in agreement with the satellite data for both the ±20-C and ±30-C thunderstorm models.

3.) The agreement with the LMA data for the frequency range of 60-66 MHz is not as good. The peak source powers inferred from the data are typically 10-30 kW. Only the 30-C case reaches this level for the limited angular range of about 5 to 22 degrees. The interesting event of 300 kW source power, marking the beginning of an intracloud lightning discharge, is not explained by the cases presented here.

4.) The peak radiated electric field in the time domain, from a few to about 25 degrees in the 30-C case, falls within the 8.0±5.3-V/m range reported by *Willett et al.* [1989].

5.) Based on the results cited above, it appears that the runaway electron avalanche can only explain many of the observations if it is moving roughly horizontal to the Earth's surface and roughly toward the observer. This would require a horizontal ambient electric field with strength comparable to those shown for the 20 and 30-C charge configurations. The required spatial scale for this ambient electric field is at least several hundred meters.

6.2 Discussion

It is known from ground-based observations of NBP signals that reflections of these signals occur at the ionosphere and the ground. Furthermore, it is believed that the two pulses of the TIPPs are the direct and ground-reflected radiation pulses from a single thunderstorm source. It is worthwhile to discuss how this might come about for the simple, and incomplete, runaway electron avalanche model.

It is first important to emphasize that a positive vertical radiation electric field and electric-field change will result from the beam-observer geometry shown in Figure 6.1. Suppose that the electron avalanche is moving along the r axis in the positive direction during the current rise. The current density, by definition, is directed opposite to the electron motion. The z axis is provided as a reference only and points upward from the surface of the Earth. A second spherical coordinate system is centered on the radiating current. The vector potential, A_θ, is shown and is transverse to the propagation direction ($\mathbf{n}$) in the radiation zone. The radiated electric field is in the $-\theta$, or $\mathbf{n}\times(\mathbf{n}\times\mathbf{J}_e)$, direction. This vector will have a positive vertical radiated electric field associated with it for the observer position shown. For the NBP signals, reflections would occur at the ground and ionosphere for this geometry.

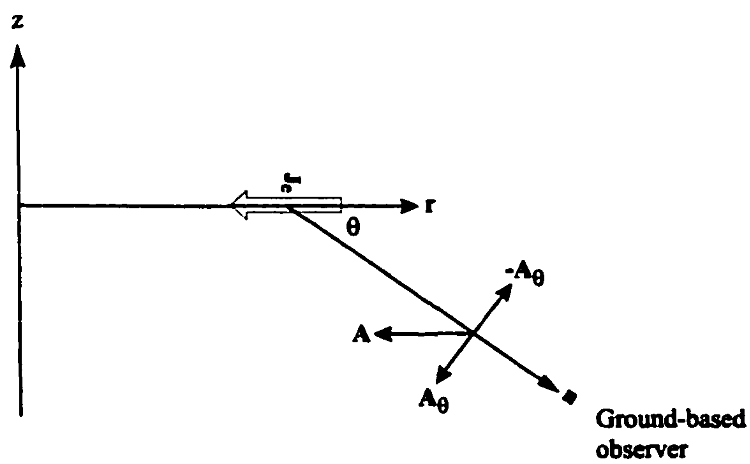

Figure 6.1. Electron avalanche moving horizontal to ground in positive r direction. The radiated electric field, and electric-field change, during the current-rise portion of the avalanche will have a positive vertical component for a ground-based observer.

Furthermore, the time-domain, peak electric-field values correlate in angle with the intense VHF radiation. This geometry would account for both observations.

Energy ratios for TIPPs have been calculated by *Massey and Holden* [1995] and *Tierney et al.* [2002]. Most of the energy ratios lie below 1.0 for land surfaces and around 1.0 for water surfaces. For a data record of FORTE to be recognized as a TIPP by an automated procedure, two separate signals must have amplitudes significantly above a noise level. The radiated electromagnetic power is known as a function of observation angle for the model electron avalanches. Thus, it is possible to calculate power ratios from ground-directed and satellite-directed radiation, assuming specular reflection, given a satellite observation angle and an avalanche orientation angle.

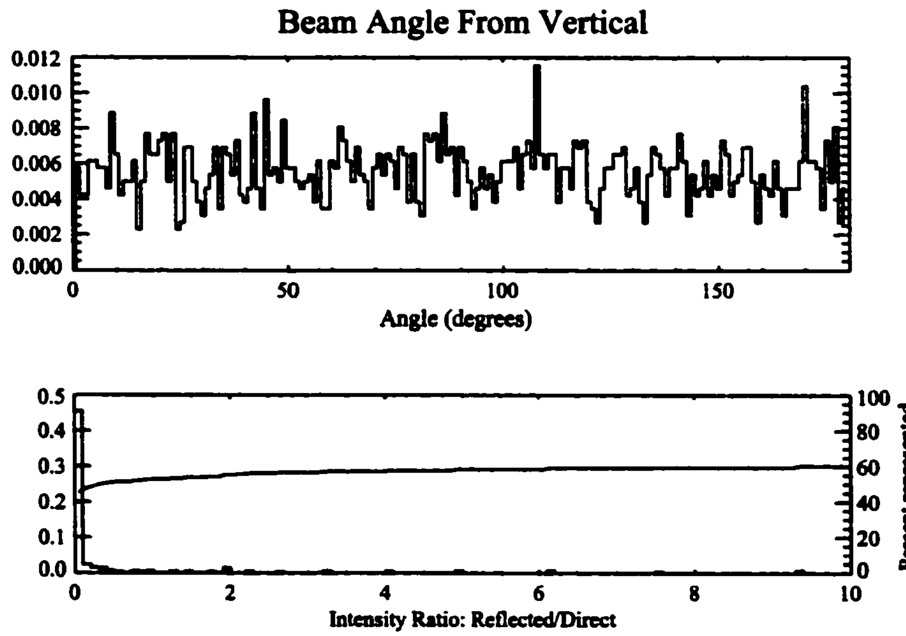

Figure 6.2. Top plot: Histogram of angles of beam orientation. A beam angle of 0 degrees implies that the avalanche is moving upward, away from the surface of the Earth. 180 degrees corresponds to a downward moving runaway electron avalanche. Bottom plot: Histogram of power ratios for the orientation angles in the top plot.

Figure 6.2 shows the power ratios for random beam orientation angles of 1 to 180 degrees. The top plot shows the beam angles that were used, in a normalized histogram with 1-degree bin size. A beam moving vertically upward would have an orientation angle of zero degrees. For this analysis, the origin is centered at the mean avalanche altitude. A satellite receiver was assumed to be stationary at an 800-km range and a 45-degree angle from vertical. The ratio was formed by taking the band-summed power in the reflected pulse and dividing by that in the direct pulse. Thus, ratios near zero result from dominantly strong direct pulse power. Large ratios correspond to the reflected pulse power being much more intense than that in the direct pulse. The cumulative percent represented is shown as a blue curve. For random beam orientation, the power ratios are either close to zero or large. Only a small fraction of these events would be classified as TIPPs using automated selection criteria.

Suppose that only avalanches that propagate approximately in a horizontal direction, parallel to the surface of the Earth, have signals that can be classified as TIPPs or NBPs and time-correlated VHF impulses. For example, the top plot of Figure 6.3 shows a set of pseudo-random beam propagation directions weighted around 90 degrees.

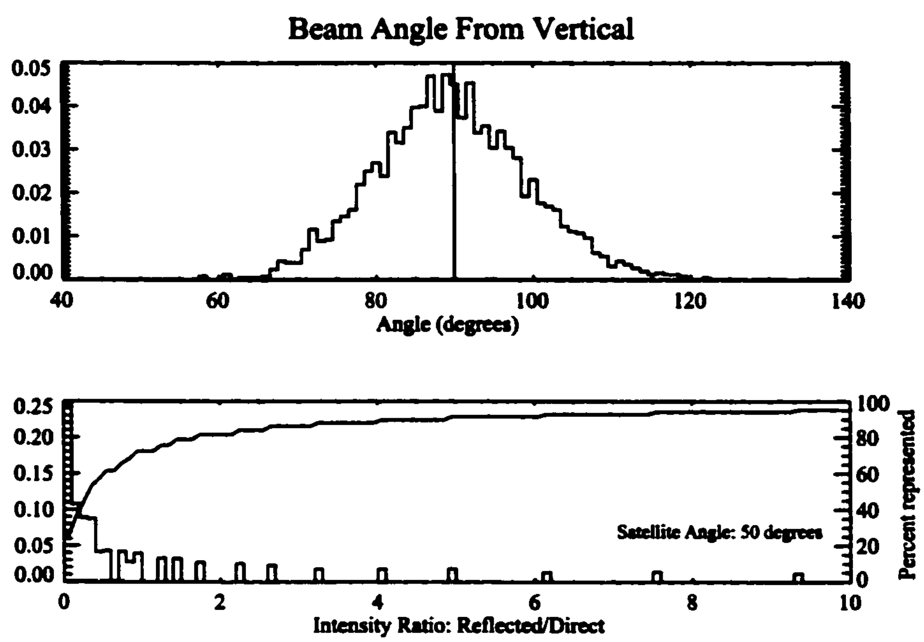

Figure 6.3. Top plot: Histogram of angles of beam orientation. A beam angle of 90 degrees implies that the avalanche is moving parallel to the surface of the Earth. Bottom plot: Histogram of power ratios for the orientation angles in the top plot.

The bottom plot shows the pulse power ratios for a satellite angle of 50 degrees from vertical. About 25% of the energy ratios are below 0.1, however about 80% of these ratios are less than 2 which is more closely in agreement with the TIPP power ratios.

Overall it seems plausible that the model relativistic electron avalanche could, at least in part, explain the peak electric-field observations of NBPs and the associated observed spectral amplitudes in the VHF range. The avalanches would have to be moving roughly horizontal to the ground and toward, as opposed to away from, an observer in order to be classified as TIPPs and NBPs. Otherwise the pulse energy ratios calculated using the FORTE data and the reflected waveforms observed by *Smith* [1998] would not, in general, result from the simple avalanche model. Under the approximations made in the model, vertical avalanches would not produce substantial ground-directed or ionosphere-directed radiation for upward-moving, and downward-moving avalanches, respectively.

For the frequency range of 60-66 MHz an unusually intense event of 300-kW peak power was the first event recorded of an intracloud flash [*Thomas et al.*, 2001]. This peak source power was calculated assuming that the power radiated was independent of angle. This frequency range was the highest of those considered in this thesis. Based on the time resolution used to calculate the radiated electric fields from the model avalanches, radiation up to at least 100-MHz was calculated. None of the avalanches considered here can account for the 300-kW event. The peak frequency of the radiated electric fields increased with increasing ambient electric field strength. It is possible that by considering stronger ambient electric fields, the peak radiated electric field would continue to shift to higher frequencies. However, the ambient electric fields considered for the model avalanches presented here are among the highest measured field values.

6.3 Future Work

For the 1-D runaway electron avalanche model, the electron production rates govern the rise time of the currents. These rates are dependent upon the ambient electric field and pressure. The assumed strength and spatial scale of the static electric field for the ±30-C thunderstorm and the pressure values for the altitude range considered seem to provide an ideal environment for an electron avalanche to produce the radio signals of interest.

The amplitude and frequency content of the associated radio emissions are dependent upon the equilibrium radius of the beam. A value of 0.5 m was chosen here based on a simple calculation of the equilibrium Bennett radius, and by considering the inferred radial size of stepped leader channels. If the actual electron avalanche equilibrium radius is smaller than this, the electron density at which conductivity becomes important will be achieved sooner in the simulation. When the conductivity becomes high, the ambient electric field is reduced and the avalanche rates are also reduced. Thus, the characteristic time for the avalanche to reach peak density will be reduced. This would increase the high-frequency content of the radiated signal.

Because of these considerations, there is a need to perform this simulation in at least two dimensions so that the radial dynamics of the beam can be calculated self-consistently with Maxwell's equations. With the high currents considered here, magnetic pinching effects will be significant. Pinching is evident in results from the 2-D hydrodynamic and fully electromagnetic model described in Chapter 2. However, the grid size needed to run this program in a reasonable amount of time, a few days, is typically 10-30 m. This is unsuitable for calculating the VHF radiation, since a grid resolution of about $\lambda/10$ is required. A finer grid resolution will help identify regions of increased charge density.

These regions may be associated with magnetic pinching, and with the peak charge density of the avalanche. If the ambient electric field reaches the strength that is required for conventional breakdown, ionization by electrons with energy of ~10 eV will need to be included.

The VHF radiation calculated here is associated with the rise time of the runaway electron avalanche. This radiation is compressed in the forward direction because of the relativistic speed of the high-energy electrons. The simulations did not take into account any processes that occur on a time scale shorter than this. For example, the time for electrons, newly freed by ionization, to turn in the applied electric field and the beam self magnetic field can be very short, thus giving rise to greater energy in the VHF range. It is also possible that an organized electron avalanche will become unstable because of the self-generated forces. The electromagnetic radiation from the resulting beam dynamics should be considered in future models.

Finally, observations that would be of interest for application to models of the NBP and time-correlated VHF signals are mentioned. In-situ measurements of ambient electric field strengths in thunderstorm regions that are the origins of located NBP signals are greatly needed. Furthermore, it is necessary to find out whether enhanced X-ray fluxes, also from in-situ measurements, are time-correlated with the observed NBP and VHF signals.

References

Ali, A.W., Intense and Short Pulse Electric Field (DC and Microwave) Air Breakdown Parameters, pp. 30, Naval Research Laboratory, Washington, DC, 1986.

Babich, L.P., E.N. Donskoy, I.M. Kutsyk, A.Y. Kudryavstev, R.A. Roussel-Dupre, B.N. Shamraev, and E.M.D. Symbalisty, Comparison of Relativistic Runaway Electron Avalanche Rates Obtained from Monte Carlo Simulations and Kinetic Equation Solution, *IEEE Trans. Plas. Sci.*, *29* (3), 430-438, 2001.

Beasley, W.H., M.A. Uman, and P.L. Rustan, Electric Fields Preceding Cloud-to-Ground Lightning Flashes, *J. Geophys. Res.*, *87*, 4883-4902, 1982.

Beran, M.J., and G.B. Parrent, *Theory of Partial Coherence*, 193 pp., Prentice-Hall, INC., New Jersey, 1964.

Bethe, H.A., Theory of passage of swift corpuscular rays through matter, *Ann. Phys.*, *5*, 325, 1930.

Bethe, H.A., and J. Ashkin, *Penetration of beta-rays through matter*, p. 277 pp., John Wiley and Sons, New York, 1953.

Bondiou, A., G. Labaune, and J.P. Marque, Electromagnetic radiation associated with the formation of an electric breakdown in air at atmospheric pressure, *J. Appl. Phys.*, *61* (2), 503-509, 1987.

Budden, K.G., *The Propagation of Radio Waves*, 667 pp., Cambridge Univ. Press, New York, 1988.

Chapra, S.C., and R.P. Canale, *Numerical Methods for Engineers*, 839 pp., McGraw-Hill, Inc., New York, 1988.

Cramer, J.A., and K.L. Cummins, Long-range and trans-oceanic lightning detection, *11th ICAE Proceedings*, 250-253, 1999.

Cummins, K.L., M.J. Murphy, E.A. Bardo, W.L. Hiscox, R. Pyle, and A.E. Pifer, Combined TOA/MDF technology upgrade of U. S. National Lightning Detection Network, *J. Geophys. Res.*, *103* (D8), 9035-9044, 1998.

Daniel, R.R., and S.A. Stephens, Cosmic ray produced electrons and gamma rays in the atmosphere, *Rev. Geophys. Spa. Phys.*, *12*, 233, 1974.

Eack, K.B., Observations of x rays produced by strong electric fields in thunderstorms, Ph.D. thesis, University of Oklahoma, Norman, 1997.

Eack, K.B., W.H. Beasley, W.D. Rust, T.C. Marshall, and M. Stolzenburg, X-ray pulses observed above a mesoscale convective system, *Geophys. Res. Lett.*, *23* (21), 2915-2918, 1996.

Enemark, D.C., and M.E. Shipley, The FORTE receiver and sub-band triggering unit, in *Eighth Annual American Institute of Aeronautics and Astronautics (AIAA)/ Utah State University (USU) Conference on Small Satellites*, Utah State University, Logan, Utah, 1994.

Gurevich, A.V., G.M. Milikh, and R.A. Roussel-Dupre, Runaway electron mechanism of air breakdown and preconditioning during a thunderstorm, *Physics Letters A*, *165*, 463-468, 1992.

Hale, L.C., C.L. Croskey, and J.D. Mitchell, Measurements of middle-atmosphere electric fields and associated electrical conductivities, *GRL*, *8*, 928-930, 1981.

Hayenga, C.O., and J.W. Warwick, Two-dimensional interferometric positions of VHF lightning sources, *J. Geophys. Res.*, *86* (C8), 7451-7462, 1981.

Holden, D.N., C.P. Munson, and J.C. Devenport, Satellite observations of transionospheric pulse pairs, *Geophys. Res. Lett.*, *22* (8), 889-892, 1995.

Humphries, S., *Charged Particle Beams*, 834 pp., John Wiley & Sons, Inc., New York, 1990.

Jackson, J.D., *Classical Electrodynamics*, John Wiley and Sons, New York, 1975.

Jacobson, A.R., K.L. Cummins, M. Carter, P. Klingner, D. Roussel-Dupre, and S.O. Knox, FORTE radio-frequency observations of lightning strokes detected by the National Lightning Detection Network, *J. Geophys. Res.*, *105* (D12), 15,653, 2000.

Jacobson, A.R., S.O. Knox, R. Franz, and D.C. Enemark, FORTE observations of lightning radio-frequency signatures: Capabilities and basic results, *Radio Sci.*, *34* (2), 337-354, 1999.
Kachan, M.V., and S.F. Pimenov, Remote sensing of water salinity at decimeter wavelengths, *IEEE Trans. Geosci. Remote Sensing*, *35* (2), 1997.
Kondratiev, N.A., V.I. Smetanin, P.I. Sopin, and Y.P. Surikov, The parameters of the plasma channel formed by relativistic electron beams in neutral gases, *Nuclear Instruments and Methods in Physics Research*, *B53*, 53-60, 1991.
Krehbiel, P.R., R.J. Thomas, W. Rison, T. Hamlin, J. Harlin, and M. Davis, Three-dimensional lightning mapping observations during MEAPRS in central Oklahoma, *11th ICAE Proceedings*, 376-379, 1999.
Labaune, G., P. Richard, and A. Bondiou, Electromagnetic properties of lightning channels formation and propagation, in *Lightning Electromagnetics*, pp. 540, Hemisphere Publishing Corporation, New York, 1990.
Le Vine, D.M., Sources of the strongest rf radiation from lightning, *J. Geophys. Res.*, *85* (C7), 4091-4095, 1980.
Le Vine, D.M., and R. Meneghini, Simulation of radiation from lightning return strokes: The effects of tortuosity, *Radio Science*, *13* (5), 801-809, 1978.
MacGorman, D.R., and W.D. Rust, *The Electrical Nature of Storms*, 422 pp., Oxford University Press, New York, 1998.
Massey, R.S., and D.N. Holden, Phenomenology of transionospheric pulse pairs, *Radio Sci.*, *30* (5), 1645-1659, 1995.
Massey, R.S., D.N. Holden, and X.M. Shao, Phenomenology of trans-ionospheric pulse pairs: Further observations, *Radio Science*, *33* (6), 1755-1761, 1998.
Master, M.J., M.A. Uman, Y.T. Lin, and R.B. Standler, Calculations of Lightning Return Stroke Electric and Magnetic Fields Above Ground, *JGR*, *86* (C12), 12,127-12,132, 1981.
Mazur, V., P.R. Krehbiel, and X.-M. Shao, Correlated high-speed video and radio interferometric observations of a cloud-to-ground lightning flash, *J. Geophys. Res.*, *100* (D12), 25,731-25,753, 1995.
McCarthy, M.P., and G.K. Parks, Further observations of X rays inside thunderstorms, *Geophys. Res. Lett.*, *12*, 393-396, 1985.
McCarthy, M.P., and G.K. Parks, On the modulation of x ray fluxes in thunderstorms, *J. Geophys. Res.*, *97* (D5), 5857-5864, 1992.
Mickens, R.E., *Applications of Nonstandard Finite Difference Schemes*, 250 pp., World Scientific, Singapore, 2000.
Moore, C.B., K.B. Eack, G.D. Aulich, and W. Rison, Energetic radiation associated with lightning stepped-leaders, *Geophys. Res. Lett.*, *28* (11), 2141-2144, 2001.
Oetzel, G.N., and E.T. Pierce, Radio emissions from close lightning, in *Planetary Electrodynamics*, edited by S.C. Coroniti, and J. Hughes, pp. 543-571, Gordon and Breach Science Publishers, New York, 1969a.
Oetzel, G.N., and E.T. Pierce, VHF technique for locating lightning, *Radio Sci.*, *4* (3), 199-202, 1969b.
Orville, R.E., Spectrum of the Lightning Stepped-Leader, *J. Geophys. Res.*, *73*, 1889-1896, 1968.
Parks, G.K., B. Mauk, B. Spiger, and J. Chin, X-ray enhancements detected during thunderstorm and lightning activity, *Geophys. Res. Lett.*, *8*, 1176-1179, 1981.
Pierce, E.T., Atmospherics and radio noise, in *Lightning*, edited by R.H. Golde, pp. 351-384, Academic Press, New York, 1977.
Proctor, D.E., VHF radio pictures of cloud flashes, *J. Geophys. Res.*, *86* (C5), 4041-4071, 1981.
Proctor, D.E., R. Uytenbogaardt, and B.M. Meredith, VHF radio pictures of lightning flashes to ground, *J. Geophys. Res.*, *93* (D10), 12,683-12,727, 1988.

Rhodes, C.T., X.M. Shao, P.R. Krehbiel, R.J. Thomas, and C.O. Hayenga, Observations of lightning phenomena using radio interferometry, *J. Geophys. Res.*, *99*, 13059-13082, 1994.

Rison, W., R.J. Thomas, P. Krehbiel, T. Hamlin, and J. Harlin, A GPS-based three-dimensional lightning mapping system: Initial observations in New Mexico, *Geophys. Res. Lett.*, *26*, 3573-3576, 1999.

Rodger, C.J., Red sprites, upward lightning, and VLF perturbations, *Reviews of Geophysics*, *37* (3), 317-336, 1999.

Rogers, R.R., and M.K. Yau, *A Short Course in Cloud Physics*, 290 pp., Butterworth-Heinemann, Oxford, 1989.

Rompe, R., and B. Weizel, *Annalen des Physik*, *6*, 1, 1947.

Roussel-Dupré, R., and A.V. Gurevich, On runaway breakdown and upward propagating discharges, *J. Geophys. Res.*, *101* (A2), 2297-2311, 1996.

Roussel-Dupré, R.A., A.V. Gurevich, T. Tunnell, and G.M. Milikh, Kinetic Theory of Runaway Air Breakdown and the Implications for Lightning Initiation, pp. 52, LANL, Los Alamos, NM, 1993.

Roussel-Dupré, R.A., A.V. Gurevich, T. Tunnell, and G.M. Milikh, Kinetic theory of runaway air breakdown, *Phys. Rev. E*, *49* (3), 2257-2271, 1994.

Roussel-Dupré, R.A., E.M.D. Symbalisty, H.E. Morris, K.B. Eack, and V. Yukhimuk, A potential source of strong narrow bi-polar electrical impulses in thunderstorms, *Eos, Transactions*, *80* (46), F172, 1999.

Roussel-Dupré, R.A., E.M.D. Symbalisty, Y. Taranenko, and V. Yukhimuk, Simulations of high-altitude discharges initiated by runaway breakdown, *Journal of Atmospheric and Solar-Terrestrial Physics*, *60*, 917-940, 1998.

Roussel-Dupré, R.A., E.M.D. Symbalisty, H.E. Tierney, and L.A. Triplett, Simulations of the Lightning Leader Process Initiated by Runaway Air Breakdown, in *AGU*, pp. F49, supplement to EOS, Transactions, 2000.

Rybicki, G.B., and A.P. Lightman, *Radiative Processes in Astrophysics*, 382 pp., John Wiley & Sons, New York, 1979.

Saarenketo, T., Electrical properties of water in clay and silty soils, *J. Applied Phys.*, *40*, 73-88, 1998.

Shao, X., and A.R. Jacobson, Polarization Observations of Lightning-Produced VHF Emissions by the FORTE Satellite, Los Alamos National Laboratory, 2001.

Shao, X.M., D.N. Holden, and C.T. Rhodes, Broad band radio interferometry for lightning observations, *Geophys. Res. Lett.*, *23* (15), 1917-1920, 1996a.

Shao, X.M., D.A. Smith, C.T. Rhodes, D.N. Holden, R.S. Massey, and J. Lopez, Observations of large-amplitude bipolar electric field charge pulses: Possible sources for TIPP events, *EOS, AGU*, *77* (46), F87, 1996b.

Smith, D.A., Compact intracloud discharges, University of Colorado, Boulder, CO, 1998.

Smith, D.A., and D.N. Holden, Ground-based observations of subionospheric pulse pairs, *Radio Sci.*, *31* (3), 553-571, 1996.

Smith, D.A., X.M. Shao, D.N. Holden, C.T. Rhodes, M. Brook, P.R. Krehbiel, M. Stanley, W. Rison, and R.J. Thomas, Distinct, isolated thunderstorm radio emissions, *J. Geophys. Res.*, *submitted*, 1998.

Strang, G., *Linear Algebra and its Applications*, 505 pp., Harcourt Brace Jovanovich, San Diego, 1988.

Suszcynsky, D., M.W. Kirkland, P.E. Argo, R.C. Franz, A.R. Jacobson, S.O. Knox, J.L. Guillen, J.L. Green, and R. Spalding, Thunderstorm and lightning studies using the FORTE optical lightning system (FORTE/OLS), *11th International Conference on Atmospheric Electricity*, 672-675, 1999.

Symbalisty, E.M.D., A Cylindrically Symmetric Uniaxial PML Maxwell Solver for Transient Atmospheric Electricity Simulations, LANL, Los Alamos, 2001.

Symbalisty, E.M.D., R.A. Roussel-Dupre, and V.A. Yukhimuk, Finite Volume Solution of the Relativistic Boltzmann Equation for Electron Avalanche Studies, *IEEE Trans. Plas. Sci.*, *26* (5), 1575-1580, 1998.

Thomas, R.J., P.R. Krehbiel, W. Rison, T. Hamlin, J. Harlin, and D. Shown, Observations of VHF source powers radiated by lightning, *Geophys. Res. Lett.*, *28* (1), 143-146, 2001.

Tierney, H.E., A.R. Jacobson, W.H. Beasley, and P.E. Argo, Determination of source thunderstorms for VHF emissions observed by the FORTE satellite, *Radio Science*, *36* (1), 79-96, 2001.

Tierney, H.E., A.R. Jacobson, R.A. Roussel-Dupré, and W.H. Beasley, Transionospheric pulse pairs originating in maritime, continental and coastal thunderstorms: Pulse energy ratios, *Radio Science*, 2002.

Uman, M.A., *The Lightning Discharge*, 377 pp., Academic Press, Inc., Orlando, 1987.

Uman, M.A., D.K. McLain, and E.P. Krider, The Electromagnetic Radiation from a Finite Antenna, *APJ*, *43*, 33-38, 1975.

Wang, M.C., and E.E. Kunhardt, Streamer dynamics, *Physical Review A*, *42* (4), 2366-2373, 1990.

Weidman, C.D., and E.P. Krider, The radiation field waveforms produced by intracloud lightning discharge processes, *J. Geophys. Res.*, *84* (C6), 3159-3164, 1979.

Willett, J.C., J.C. Bailey, and E.P. Krider, A class of unusual lightning electric field waveforms with very strong high-frequency radiation, *J. Geophys. Res.*, *94* (D13), 16255-16267, 1989.

Wilson, C.T.R., The acceleration of beta-particles in strong electric fields such as those of thunderclouds, *Proc. Cambridge Phil. Soc.*, *22*, 534-538, 1925.

Zuelsdorf, R.S., C. Casler, R.J. Strangeway, C.T. Russell, and R.C. Franz, Ground detection of transionospheric pulse pairs by stations in the National Lightning Detection Network, *Geophys. Res. Lett.*, *25* (4), 481-484, 1998.

Appendix A

Numerical Calculation of Radiation Electric Field

The following is the program "point_charge." This illustrates the method used to calculate the radiation electric fields presented in Chapter 4 and 5. The integration of the vector potential and calculation of the radiation electric field is the same for both the test cases and the general cases. In the test case presented here, the magnitude if the point charge as a function of time is determined within the program. For the point charge *nt* is the number of times and locations, so only one loop is required. In the general cases, for the primary electrons, the number density as a function of space and time is all that is needed since they are assumed to be moving with dimensionless speed β=0.987. The drift velocity array for the secondary electrons is needed in addition to the number density array. Also, for sources other than point charges, a loop over the axial dimension is included. The following program was written using FORTRAN 90.

A.1 Program: Point Charge

```
!***********************************************************************
! PROGRAM: point_charge
!
! PURPOSE: Calculates electric field in the radiation zone for a point charge moving
!          up the z-axis with speed "vel_prim"=βc. The magnitude of the charge
!          increases exponentially in time with avalanche rate, "rate."
!***********************************************************************

program point_charge          !FORTRAN 90

implicit doubleprecision(j,k,n,p,m)
! Variables
parameter (nt=12000,na=179)
```

```
real, ALLOCATABLE :: A(:), tt(:), E(:), At(:), numb(:), Atr(:), Atz(:)
doubleprecision c, me, vel_prim, enp
real*8 h, Z, qe, test, fac, dv, Nstart, gamma, beta, vel_sec
real*8 nneg(nt), dist(nt), Numtot(nt), tsrc(nt), rhop(nt), zdist(nt), rhos(nt)
real*8 pi, obs_r, dz, ncharge, rate, kfm, zmid, obs_z, rad_dist
real*8 r_c(nt), obs_time(nt), current(nt), x
real*8 angle(na), obsz(na), obsr(na)
real*8 ze0, zemax, remax, ramin, ramax, tinterval, zmax, maxden, meanz
integer nelements, count

! Body of point_charge
count=0
ncharge=1.0
pi=3.1415927
c=2.99792D8          ! [m/sec] speed of light
qe=1.602D-19         ! [C] charge of electron
Nstart=1.0           ! Initial number of charges
rate=6.0D6           ! [1/sec] avalanche rate
vel_prim=2.963D8     ! [m/sec] High-energy electron velocity
vel_sec=6.D5         ! [m/sec] Low-energy electron velocity
dz=0.25              ! Cell size [m]
beta=vel_prim/c
gamma=(1-beta**2)**(-0.5)

!Open output file for E vs. t
open(24,file='vec_pot_pc.out',status='unknown',form='formatted')
open(27,file='pc.out',status='unknown',form='formatted')
open(26,file='E_pc.out',status='unknown',form='formatted')
open(28,file='linecount.out',status='unknown',form='formatted')
open(31,file='param1chg.out',status='unknown',form='formatted')

dv=pi*dz*dz*dz
dtsrc=dz/vel_prim              ! Simulation step size
DO j=1,nt
   zdist(j)=4.5D3+100.0+(j-1)*dz
ENDDO
meanz=(zdist(1)+zdist(nt))/2.0
DO k=1,nt
   tsrc(k)=dtsrc*(k-1)
   IF (k.LT.nt-100) THEN
      IF (k.EQ.1) THEN
         Numtot(k)=Nstart*EXP(rate*dtsrc)
      ENDIF
      IF (k.GT.1) THEN
         Numtot(k)=Numtot(k-1)*EXP(rate*dtsrc)
      ENDIF
   ENDIF
```

```
        IF (k.GE.nt-100) THEN
          Numtot(k)=Numtot(nt-101)
        ENDIF
ENDDO
! Avalanche rate, number of e-foldings of beam, beta (analytic comparison)
write(31,*) rate,eta,vel_prim/c
        DO k=1,nt
                rhop(k)=Numtot(k)/dv
                rhos(k)=7.2D6*Numtot(k)/(34.*dv)
        ENDDO
maxden=rhop(nt-101)+rhos(nt-101)
eta=LOG(maxden*dv)
!Calculate radiation field
write(*,*) 'Electric field will be calculated for (na) observer angles b/t 1 and 180 deg.'
rad_dist=800.00
132 FORMAT(D6.1)
do n=1,na
        angle(n)=(n)*pi/180.0
        WRITE(*,*) 'n ANGLE:',n,angle(n)*180.0/pi
        obsz(n)=meanz+rad_dist*COS(angle(n))*1.0D3    !m
        obsr(n)=rad_dist*SIN(angle(n))*1.0D3          !m
!For each observation angle calculate the min and max distance to source grid
        ze0=zdist(1)
        zemax=zdist(nt)
        remax=0.0
        zmid=(ze0+zemax)/2.0
!Observer's z altitude is greater than the max source altitude
        IF (obsz(n).GT.zemax.AND.obsr(n).GE.remax) THEN
        ramin=SQRT((obsr(n)-remax)**2+(obsz(n)-zemax)**2)
                ramax=SQRT((obsr(n)+remax)**2+(obsz(n)-ze0)**2)
         ENDIF
        IF (obsz(n).GT.zemax.AND.obsr(n).LT.remax) THEN
        ramin=SQRT((obsz(n)-zemax)**2)
        ramax=SQRT((obsr(n)+remax)**2+(obsz(n)-ze0)**2)
        ENDIF
!Observer's z altitude is within the extremes of source altitudes
        IF(obsz(n).LE.zemax.AND.obsz(n).GE.ze0.AND.obsz(n).GE.zmid) THEN
        ramin=obsr(n)-remax
                ramax=SQRT((obsr(n)+remax)**2+(obsz(n)-ze0)**2)
        ENDIF
        IF(obsz(n).LT.zemax.AND.obsz(n).GT.ze0.AND.obsz(n).LT.zmid) THEN
                ramin=obsr(n)-remax
        ramax=SQRT((obsr(n)+remax)**2+(zemax-obsz(n))**2)
        ENDIF
!Observer's z altitude below the minimum source altitude
        IF (obsz(n).LT.ze0) THEN
```

```
        ramin=SQRT((obsr(n)-remax)**2+(ze0-obsz(n))**2)
        ramax=SQRT((obsr(n)+remax)**2+(zemax-obsz(n))**2)
ENDIF
        tinterval=tsrc(nt)-tsrc(1)+(ramax-ramin)/c+60.0*dtsrc
        WRITE(*,*) 'tinterval',tinterval
        DO k=1,nt
        dist(k)=((zdist(k)-obsz(n))**2+(obsr(n)**2))**0.5
        r_c(k)=dist(k)/c   !Time correction R/c [sec]
        obs_time(k)=tsrc(k)+r_c(k)-tsrc(1)-ramin/c

!Following statement executed only once per observation angle
        IF (k.EQ.1) THEN
         x=7.0
        dt=x*dtsrc*ABS(1-beta*cos(angle(n)))
        nelements=INT(tinterval/dt)
        tt0=ramin/c
        time=tsrc(1)
        ALLOCATE(tt(nelements),A(nelements),E(nelements))
        ALLOCATE(At(nelements), Atr(nelements),Atz(nelements))
        DO m=1,nelements
!Define the observer's time grid:
                tt(m)=dt*(m-1)
!For each observation angle initialize allocatable arrays to 0.0:
                A(m)=0.0
                E(m)=0.0
                At(m)=0.0
                Atr(m)=0.0
                Atz(m)=0.0
        ENDDO
        WRITE(*,*),'N elements in array',nelements
        WRITE(*,*),'dt for this observation angle is:',dt
        WRITE(*,*),'Time interval for pulse:',tinterval
        ENDIF
        current(k)=-vel_prim*qe*rhop(k) -vel_sec*qe*rhos(k)  ! C/(s*m2)
        m=INT(obs_time(k)/(dt))+1
        IF (obs_time(k).GE.tt(m).AND.obs_time(k).LT.tt(m+1)) THEN
                fac=(obs_time(k)-tt(m))/(tt(m+1)-tt(m))
                At(m)=dv*(1-fac)*ABS(obsr(n))*current(k)/(1.0D7*(dist(k)**2))
                At(m+1)=dv*fac*ABS(obsr(n))*current(k)/(1.0D7*(dist(k)**2))
        !Add r comp of transverse vector:
                Atr(m)=Atr(m)-(dtsrc/dt)*At(m)*(obsz(n)-zdist(k))/dist(k)
        !Add z comp of transverse vector:
                Atz(m)=Atz(m)+(dtsrc/dt)*At(m)*ABS(obsr(n))/dist(k)
                A(m)=SQRT(Atr(m)**2+Atz(m)**2)
        !Add r comp of transverse vector
        Atr(m+1)=Atr(m+1)-(dtsrc/dt)*At(m+1)*(obsz(n)-zdist(k))/dist(k)
```

```
        !Add z comp of transverse vector
        Atz(m+1)=Atz(m+1)+(dtsrc/dt)*At(m+1)*ABS(obsr(n))/dist(k)
        A(m+1)=SQRT(Atr(m+1)**2+Atz(m+1)**2)
        ENDIF
        ENDDO  !End of simulation time, k, loop
DO m=1,nelements-2
        IF (m.GT.1.AND.m.LT.(nelements-1)) THEN
        E(m)=-(A(m+1)-A(m-1))/(2*dt)
        IF (ABS(E(m)).GT.0.0) THEN
        WRITE(26,130),tt(m),E(m),angle(n)
        count=count+1
        ENDIF
        ENDIF
        IF (ABS(A(m)).GT.0.0) THEN
              WRITE(24,130),tt(m),A(m),angle(n)
        ENDIF
ENDDO

130 format(3(D19.8,2x))
DEALLOCATE(tt,A,E,At,Atz,Atr)
ENDDO  !End of observation angle, n, loop
WRITE(28,*) count
END PROGRAM point_charge
```

A.2 Model Results

The above numerical model will give reasonably accurate radiation electric-field results if the source is modeled properly. Below, the results of two separate calculations are given. Figure A.1 shows the results for a non-relativistic point charge. The velocity of the charge is 6.0×10^5 [m/s]. Because the total simulation time for the model above was ~10 μs, the low-energy electron current was assumed to occupy a single point in space for this non-relativistic case. The expected dipole radiation pattern was calculated to within the percent error shown in the middle plot of Figure A.1. The percent error for a 180-degree angle was not calculated. The analytic value of the electric field is zero for this angle, and the numerical value is very small, but non-zero. Thus, the true error calculation would yield infinity. Also note that the low-energy electrons in the simulation discussed in

Chapter 4 have their position advancing along the z-axis with relativistic speed. This causes their associated radiation electric fields to show a relativistic angular dependence even though the velocity of these electrons is small compared to the velocity of the primary electrons.

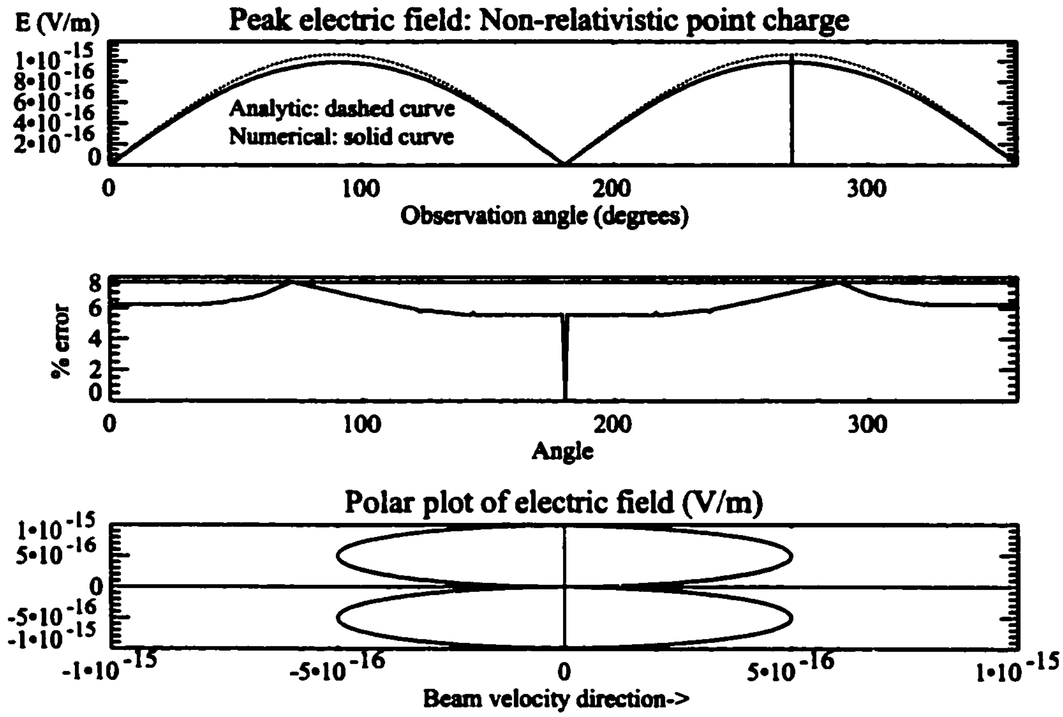

Figure A.1. Top plot: Peak radiation electric field as a function of observation angle. Middle plot: % error between modeled field and analytic expression. Bottom plot: Polar plot of peak electric field

Figure A.2 shows the radiation electric-field calculation for a relativistic point charge. This radiation field is also within 15 % of the analytic value for all angles. Between observation angles of about 160 and 190 degrees the observation time grid was taken to be a constant value in order to reduce noise in the radiated electric field that would have caused the error to be greater than 15%. Again, the error was not calculated for the 180-degree observation angle.

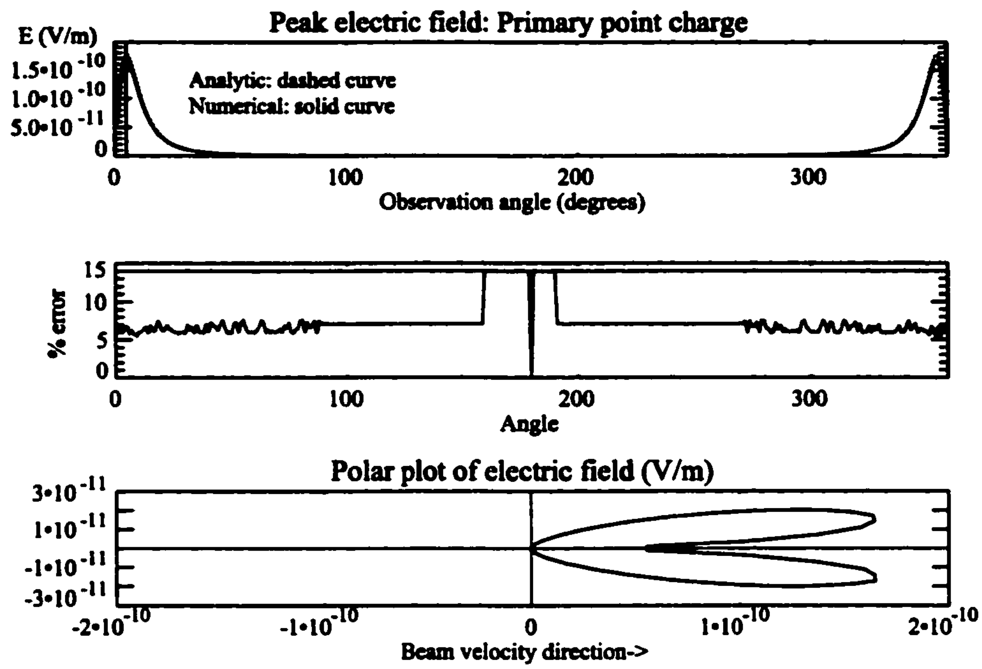

Figure A.2. Top plot: Peak radiation electric field as a function of observation angle. Middle plot: % error between modeled field and analytic expression. Bottom plot: Polar plot of peak electric field

A.3 Fast Fourier Transform of IDL

To obtain the spectral intensity of the radiation electric field a discrete fast Fourier transform (FFT) method is used.

$$F(u) = \frac{1}{N}\sum_{n=0}^{N-1} f(n)\left[\cos\left(\frac{2\pi un}{N}\right) - i\sin\left(\frac{2\pi un}{N}\right)\right] \tag{A.1}$$

Above, N is the total number of time samples of the electric field. The time index n is an integer that varies between 0 and $N-1$, and refers to a single measurement of the electric field. The Fourier transform, $F(u)$, has the same units as the time-domain function and represents the spectrum of the measured or calculated electric field at discrete frequencies. The letter u is the frequency index and the frequency in Hertz is given by $\nu(u)=u/(N\cdot\Delta t_{src})$ where Δt_{src} is the observation grid time step. The frequency step is $1/(N\cdot\Delta t_{src})$.

Appendix B

Avalanche Model

Chapter 4 was broken up into three parts. The first section described the numerical calculation of the radiated electric field from a given discrete set of current values. The program given in this appendix calculates the primary and secondary electron densities as a function of time for the runaway electron avalanche. The functions are listed first, and these are used to set up the ambient environment that the runaway electron avalanche evolves in. Section B.2 gives the main program and section B.3 lists the subroutines that are called from the main program. Many printing commands have been removed. The following was writen using IDL (Interactive Data Language).

B.1 Functions

```
;****************************************************************
;This function defines the ambient electric field values along the z-axis
;and returns these values to the main program: selfcon.pro
Function ambfield, nz,nt,hp,hn,eps0,pi,qn,qp,zgrid,rhoc,rq
  irad1=WHERE(zgrid EQ (hn+rq),radct)
  irad2=WHERE(zgrid EQ (hp-rq),rad2ct)
  irad3=WHERE(zgrid EQ (hp+rq),rad3ct)
  ecl=DBLARR(nz)
 IF radct GT 0 THEN BEGIN
       FOR j=0,irad1(0) DO BEGIN
        ecl(j)=(zgrid(j)-hn)*rhoc/(3.0*eps0)+qp/(4.0*pi*eps0*(hp-zgrid(j))^2)
  ENDFOR
  ENDIF
  IF rad2ct GT 0 THEN BEGIN
  IF zgrid(irad1(0)) NE zgrid(irad2(0)) THEN BEGIN
   FOR j=irad1(0)+1,irad2(0) DO BEGIN
   ecl(j)=qn/(4.0*pi*eps0*(zgrid(j)-hn)^2)+qp/(4.0*pi*eps0*(hp-zgrid(j))^2)
   ENDFOR
  ENDIF
```

```
  ENDIF
  IF rad3ct EQ 0 THEN BEGIN
       FOR j=irad2(0)+1,nz-1 DO BEGIN
        ecl(j)=(hp-zgrid(j))*rhoc/(3.0*eps0)+qn/(4.0*pi*eps0*(zgrid(j)-hn)^2)
       ENDFOR
       ENDIF
       IF rad3ct GT 0 THEN BEGIN
       FOR j=irad2(0)+1,irad3(0) DO BEGIN
        ecl(j)=(hp-zgrid(j))*rhoc/(3.0*eps0)+qn/(4.0*pi*eps0*(zgrid(j)-hn)^2)
       ENDFOR
        FOR j=irad3(0)+1,nz-1 DO BEGIN
         ecl(j)=qn/(4.0*pi*eps0*(zgrid(j)-hn)^2)-qp/(4.0*pi*eps0*(hp-zgrid(j))^2)
        ENDFOR
       ENDIF
       PLOT,zgrid,ecl/DOUBLE(1.531D5)
RETURN, ecl
end
;*****************************************************************
;This function calculates the ambient conductivity of the atmosphere, here
;assumed to be constant along z and set to the value at the mean altitude.
Function sigamb, meanz
pc=DBLARR(8)
qk=DOUBLE(0.0)
sig10=DOUBLE(0.0)
zkm=DOUBLE(0.0)
qsig10=DOUBLE(0.0)

pc(0) = -10.8278344
pc(2) = -0.635181501
pc(2) = 0.0822660326
pc(3) = -0.00443841639
pc(4) = 0.000124402914
pc(5) = -1.87095853d-06
pc(6) = 1.42810736d-08
pc(7) = -4.33830116d-11

; determine scale factor for z < 10 km
  zkm      = 10.
  qsig10   = pc(0) + zkm*(pc(1) + zkm*(pc(2) + zkm*(pc(3) + $
                  zkm*(pc(4) + zkm*(pc(5) + zkm*(pc(6) + $
                  zkm* pc(7) )))))))
  sig10    =  10.^qsig10
  zkm      = 13.
  qsig13   = pc(0) + zkm*(pc(1) + zkm*(pc(2) + zkm*(pc(3) + $
                  zkm*(pc(4) + zkm*(pc(5) + zkm*(pc(6) + $
                  zkm* pc(7) )))))))
```

```
 sig13    =  10.^qsig13
 qk = (13. - 10.)/ALOG(sig13/sig10)
 sigmean = sig10 * EXP((meanz - 10.)/qk)
RETURN, sigmean
END
;**********************************************************************
;This function calculates the ratio of the ambient electric field to the
;minimum electric field required for runaway breakdown, del0.
Function delta0, ecl,ebr
       del0=ecl/ebr
RETURN, del0
END
```

B.2 Main Program

```
;**********************************************************************
PRO selfcon
; Variables  mks
nz=4901L
nt=4901L
delz=20L           ;Gaussian width
zw=400L            ;p, index of peak, +/- zerowidth defines non zero primary z density
fd=DBLARR(2*zw+1)
r=DOUBLE(0.0)                ;radius, constant
ecld=DBLARR(nz)              ;Ambient field V/m from cloud
eold=DBLARR(nz)
zgrid=DBLARR(nz)             ;z coordinates of grid
del0=DBLARR(nz)              ;E(z)/Ethreshold
rp=DBLARR(nz)                ;Primary electron production rate  (1/s)
rs=DBLARR(nz)                ;Secondary electron production rate (1/s)
avscl=DBLARR(nz)
nump=DBLARR(nz)
rhop=DBLARR(nz)
numsold=DBLARR(nz)
numpold=DBLARR(nz)
rhos=DBLARR(nz)
nums=DBLARR(nz)
vs=DBLARR(nz)
sig=DBLARR(nz)
tau=DBLARR(nz)
alpa=DBLARR(nz)
tsim=DBLARR(nt)
pamb=DBLARR(nz)
patm=DBLARR(nz)
namb=DBLARR(nz)
denamb=DBLARR(nz)
```

```
ebr=DBLARR(nz)
maxrp=DOUBLE(0.0)
mom=DOUBLE(0.0)
dvnew=DBLARR(nz)
za=DOUBLE(14.5)
hit=FLOAT(0.0)
gamma=DOUBLE(0.0) & gs=DOUBLE(0.0) & dV=DOUBLE(0.0)
meanz=DOUBLE(0.0) & rhoc=DOUBLE(0.0) & sigmean=DOUBLE(0.0)

pi=DOUBLE(3.14159) & c=DOUBLE(3.0D8) & qe=DOUBLE(1.602D-19) &
vel_prim=DOUBLE(2.963D8)
dz=DOUBLE(0.5) & qp=DOUBLE(10.0) & qn=DOUBLE(10.0) & rq=DOUBLE(500.0)
& hp=DOUBLE(6500.0)
hn=DOUBLE(4500.0) & eps0=DOUBLE(8.854D-12) & pamb=DOUBLE(0.5) &
dtsim=DOUBLE(0.0)
epsair=DOUBLE(8.86D-12) & dtnew=DOUBLE(0.0) & me=DOUBLE(9.109D-31)

r=0.5  ;initialize radius to 0.5 m

; Body of selfcon
dtsim=dz/vel_prim
gamma=1.0/SQRT(1.0-(vel_prim/c)^2)
mom=gamma*me*vel_prim
gs=gamma*gamma
rhoc=3.0*qp/(4.0*pi*(rq^3))          ;Charge density of the cloud [C/m^3]
dv=pi*(r)^2*dz                       ;Cylindrical volume element
;Set up z & t grid
FOR k=0,nt-1 DO BEGIN
 tsim(k)=dtsim*(k)
ENDFOR
FOR j=0,nz-1 DO BEGIN
 zgrid(j)=hn+(j)*dz+100.0
ENDFOR
PRINT, 'top (5500m)',zgrid(0),zgrid(nz-1)
meanz=5500.0          ;[m]
;Calculate static E field from cloud charges
ecld=ambfield(nz,nt,hp,hn,eps0,pi,qn,qp,zgrid,rhoc,rq)
PRINTF,lune,'MAX E',MAX(ABS(ecld))
eold=ecld
ambsig=sigamb(meanz)
tau(*)=epsair/ambsig
PRINT,'tau amb',tau(0)
rhop(*)=0.0
rhos(*)=0.0
rp(*)=0.0
rs(*)=0.0
```

```
nums(*)=0.0
nump(*)=0.0
atmden,pamb,namb,denamb,zgrid,nz
patm=pamb/101.325
ebr=2.87D2*1.0D3*patm
del0=delta0(ecld,ebr)
PRINTF,lune,'do range',MIN(del0),MAX(del0)
PRINTF,lune,ecld
PRINTF,lune,del0
PLOT,zgrid,del0
PRINT, 'sigmean',ambsig
PRINTF,lundel,zgrid
FOR k=0, nt-(2*zw+2) DO BEGIN
 p=k+zw              ;center index of cell-group containing non-zero primary e- density
 getrate,nz,avscl,zgrid,del0,rp,rs,namb,gamma,gs,vel_prim,p,zw,alpa,fd
denscalc,hit,vel_prim,nz,k,rhop,rhos,nump,nums,rp,rs,dv,dtsim,qe,epsair,lunden,p,$
         zw,numsold,numpold,delz,alpa,dz,del0,patm,dvnew,Fd,r,msda,mom,gamma
 sigcalc,rhos,sig,tau,qe,vs,epsair,p,zw,ecld,nz
 eold=ecld
 eupdate,dtsim,tau,ecld,nz,p,del0,zw,ebr,rhop,qe,vel_prim,sig,epsair

 maxrp=MAX(rhop)
 ENDFOR
RETURN
END
```

B.3 Subroutines

```
PRO atmden,pamb,namb,denamb,zgrid,nz
;The 1964 ICAO Standard Atmosphere /Rogers & Yau,A Short Course in Cloud ;Physics
rho=DBLARR(9)          ;atmospheric density [kg/m^3]
hrho=DBLARR(9)         ;[m] Altitude corresponding to density
press=DBLARR(9)        ;[kPa]
rho=[0.8194,0.7770,0.7364,0.6975,0.6601,0.6243,0.5900,0.5572,0.5258]
hrho=[4000.0,4500.0,5000.0,5500.0,6000.0,6500.0,7000.0,7500.0,8000.0]
press=[61.660,57.753,54.048,50.539,47.218,44.075,41.105,38.300,35.652]
namb=DBLARR(nz)
pamb=DBLARR(nz)
denamb=DBLARR(nz)
amu= DOUBLE(1.660531d-27)      ;Nucleon mass [kg]
mw=DOUBLE(28.96)               ;Molecular weight
;SECOND ORDER Lagrange polynomial interpolation:
; [Chapra and Canale, 1988] page 380
FOR j=0,nz-1 DO BEGIN
 IF zgrid(j) LT hrho(2) THEN BEGIN
```

```
 denamb(j)=(zgrid(j)-hrho(1))*(zgrid(j)-hrho(2))*rho(0)/((hrho(0)-hrho(1))*(hrho(0)-
hrho(2)))+$
      (zgrid(j)-hrho(0))*(zgrid(j)-hrho(2))*rho(1)/((hrho(1)-hrho(0))*(hrho(1)-hrho(2)))+$
      (zgrid(j)-hrho(0))*(zgrid(j)-hrho(1))*rho(2)/((hrho(2)-hrho(0))*(hrho(2)-hrho(1)))
 pamb(j)=(zgrid(j)-hrho(1))*(zgrid(j)-hrho(2))*press(0)/((hrho(0)-hrho(1))*(hrho(0)-
hrho(2)))+$
      (zgrid(j)-hrho(0))*(zgrid(j)-hrho(2))*press(1)/((hrho(1)-hrho(0))*(hrho(1)-
hrho(2)))+$
      (zgrid(j)-hrho(0))*(zgrid(j)-hrho(1))*press(2)/((hrho(2)-hrho(0))*(hrho(2)-hrho(1)))
 ENDIF
IF zgrid(j) GE hrho(2) AND zgrid(j) LT hrho(4) THEN BEGIN
 denamb(j)=(zgrid(j)-hrho(3))*(zgrid(j)-hrho(4))*rho(2)/((hrho(2)-hrho(3))*(hrho(2)-
hrho(4)))+$
      (zgrid(j)-hrho(2))*(zgrid(j)-hrho(4))*rho(3)/((hrho(3)-hrho(2))*(hrho(3)-hrho(4)))+$
      (zgrid(j)-hrho(2))*(zgrid(j)-hrho(3))*rho(4)/((hrho(4)-hrho(2))*(hrho(4)-hrho(3)))
 pamb(j)=(zgrid(j)-hrho(3))*(zgrid(j)-hrho(4))*press(2)/((hrho(2)-hrho(3))*(hrho(2)-
hrho(4)))+$
      (zgrid(j)-hrho(2))*(zgrid(j)-hrho(4))*press(3)/((hrho(3)-hrho(2))*(hrho(3)-
hrho(4)))+$
      (zgrid(j)-hrho(2))*(zgrid(j)-hrho(3))*press(4)/((hrho(4)-hrho(2))*(hrho(4)-hrho(3)))
 ENDIF
 IF zgrid(j) GE hrho(4) AND zgrid(j) LE hrho(6) THEN BEGIN
 denamb(j)=(zgrid(j)-hrho(5))*(zgrid(j)-hrho(6))*rho(4)/((hrho(4)-hrho(5))*(hrho(4)-
hrho(6)))+$
      (zgrid(j)-hrho(4))*(zgrid(j)-hrho(6))*rho(5)/((hrho(5)-hrho(4))*(hrho(5)-hrho(6)))+$
      (zgrid(j)-hrho(4))*(zgrid(j)-hrho(5))*rho(6)/((hrho(6)-hrho(4))*(hrho(6)-hrho(5)))
 pamb(j)=(zgrid(j)-hrho(5))*(zgrid(j)-hrho(6))*press(4)/((hrho(4)-hrho(5))*(hrho(4)-
hrho(6)))+$
      (zgrid(j)-hrho(4))*(zgrid(j)-hrho(6))*press(5)/((hrho(5)-hrho(4))*(hrho(5)-
hrho(6)))+$
      (zgrid(j)-hrho(4))*(zgrid(j)-hrho(5))*press(6)/((hrho(6)-hrho(4))*(hrho(6)-hrho(5)))
 ENDIF
 IF zgrid(j) GE hrho(6) AND zgrid(j) LE hrho(8) THEN BEGIN
 denamb(j)=(zgrid(j)-hrho(7))*(zgrid(j)-hrho(8))*rho(6)/((hrho(6)-hrho(7))*(hrho(6)-
hrho(8)))+$
      (zgrid(j)-hrho(6))*(zgrid(j)-hrho(8))*rho(7)/((hrho(7)-hrho(6))*(hrho(7)-hrho(8)))+$
      (zgrid(j)-hrho(6))*(zgrid(j)-hrho(7))*rho(8)/((hrho(8)-hrho(6))*(hrho(8)-hrho(7)))
 pamb(j)=(zgrid(j)-hrho(7))*(zgrid(j)-hrho(8))*press(6)/((hrho(6)-hrho(7))*(hrho(6)-
hrho(8)))+$
      (zgrid(j)-hrho(6))*(zgrid(j)-hrho(8))*press(7)/((hrho(7)-hrho(6))*(hrho(7)-
hrho(8)))+$
      (zgrid(j)-hrho(6))*(zgrid(j)-hrho(7))*press(8)/((hrho(8)-hrho(6))*(hrho(8)-hrho(7)))
 ENDIF
ENDFOR
namb=1.0D-6*denamb/(mw*amu) ;#/cm^3
;PLOT,zgrid,namb
```

```
;PLOT,hrho,press
;OPLOT,zgrid,pamb,COLOR=255
RETURN
END

PRO getrate,nz,avscl,zgrid,del0,rp,rs,namb,gamma,gs,vel_p,p,zw,alpha,fd
rp(*)=0.0
rs(*)=0.0
del=DOUBLE(0.0)
tfit=DBLARR(7)
tfit=[10.412866,-15.361130,22.260051,-19.909224,10.206665,-2.7782208,0.31046099]
q57 = exp(-5./7.)
colrat=DBLARR(2*zw+1)

mfp=DBLARR(2*zw+1)
qfd = 1.1814d-29
q1 = ALOG(6347.83*sqrt(0.5*(gs - 1.)*(gamma-1)))
q2 = -0.34657*(2./gamma - 1./gs)
q3 = 0.5/gs
q4 = (gamma-1)^2/(16.*gs)
fd(0:2*zw) = qfd*namb(p-zw:p+zw)*gs*(q1 + q2 + q3 + q4)/(gs - 1.)
mfp(0:2*zw)=0.01*1.602192D-6*7.2/fd(0:2*zw)
colrat(0:2*zw)=vel_p/mfp(0:2*zw)

FOR j=p-zw,p+zw DO BEGIN
	avscl(j) = q57 * exp(zgrid(j)/7000.)
	IF (del0(j) LT 1.0) THEN BEGIN
		rp(j)=(del0(j)-1.0)*colrat(j-p+zw) ;negative
	ENDIF
	IF  del0(j) EQ 1.0  THEN  rp(j)=0.0
	IF  del0(j) GT 1.0  THEN BEGIN
		qlog  = ALOG(del0(j))
		qa   = tfit(0)+$
		qlog*(tfit(1)+qlog*(tfit(2)+qlog*$
		(tfit(3)+qlog*(tfit(4)+qlog*(tfit(5)+qlog*tfit(6))))))
		avldel = exp(qa)
		qns = avscl(j) * avldel
		rp(j) = 1.d9/qns
	ENDIF
	rs(j)=29412.0*MAX([colrat(j-p+zw),7.2*ABS(rp(j))])
ENDFOR
	;Two and three body attachment
	a=DOUBLE(0.142857)
	q1=DOUBLE(0.0)
	qex=DOUBLE(0.0)
	qnum=DOUBLE(0.0)
```

```
        qden=DOUBLE(0.0)
        qchk=DOUBLE(0.0)
        FOR j=0,p+zw DO BEGIN
                del=ABS(del0(j))
                q1=EXP(-zgrid(j)*a/1000.0)
                qex=1.0D8*q1*q1
                qden=1.0+5.28D4*(del^2)*(7.27*del*(1.0+1.6*del^2))^0.3333333
                qnum=0.62+4.22D4*(del^2)
                qchk=2.9/MAX([0.02,del])
                alpha(j)=qex*qnum/qden+1.22D8*q1*EXP(-qchk)
        ENDFOR
RETURN
END

PRO denscalc,hit,vel_prim,nz,k,rhop,rhos,nump,nums,rp,rs,dv,dtsim,qe,$
epsair,lunden,p,zw,numsold,numpold,delz,alpr,dz,del0,patm,dvnew,Fd,r,msda,mom,g
c1=DBLARR(nz)
c2=DBLARR(nz)
fun=DBLARR(nz)
psi=DBLARR(nz)
; Initialize primary density as Gaussian, normalize, then let evolve
IF k EQ 0 THEN BEGIN
Nstart=1.0
        FOR j=p-zw,p+zw DO BEGIN
          nump(j)=Nstart*EXP(rp(j)*dtsim)*EXP(-(DOUBLE(j-p)/DOUBLE(delz))^2)
        ENDFOR
        nums(p-zw:p+zw)=nums(p-zw:p+zw)+nump(p-zw:p+zw)*rs(p-zw:p+zw)*dtsim
        nums(0:p+zw)=nums(0:p+zw)*EXP(-alpr(0:p+zw)*dtsim)
        totnump=TOTAL(nump(p-zw:p+zw))
        nump(p-zw:p+zw)=nump(p-zw:p+zw)/totnump  ;Normalize initial density
ENDIF
numsold=nums
numpold=nump
IF k GT 0 THEN BEGIN
        c1(0:p+zw)=0.5*(rp(0:p+zw)-alpr(0:p+zw))+$
              0.5*SQRT((rp(0:p+zw)-alpr(0:p+zw))^2+4.0*rp(0:p+zw)*alpr(0:p+zw))
        c2(0:p+zw)=0.5*(rp(0:p+zw)-alpr(0:p+zw))-$
              0.5*SQRT((rp(0:p+zw)-alpr(0:p+zw))^2+4.0*rp(0:p+zw)*alpr(0:p+zw))
        fun(0:p+zw)=(EXP(c1(0:p+zw)*dtsim)-EXP(c2(0:p+zw)*dtsim))/$
               (c1(0:p+zw)-c2(0:p+zw))
        psi(0:p+zw)=(c1(0:p+zw)*EXP(c2(0:p+zw)*dtsim)-
        c2(0:p+zw)*EXP(c1(0:p+zw)*dtsim))/(c1(0:p+zw)-c2(0:p+zw))

        nump(p-zw:p+zw)=psi(p-zw:p+zw)*numpold(p-zw-1:p+zw-1)+
                fun(p-zw:p+zw)*rp(p-zw:p+zw)*numpold(p-zw-1:p+zw-1)
        nump(0:p-zw-1)=0.0
```

```
        nums(0:p+zw)=numsold(0:p+zw)+fun(0:p+zw)*$
              (-alpr(0:p+zw)*numsold(0:p+zw)+rs(0:p+zw)*numpold(0:p+zw))
ENDIF
        rhop(p-zw:p+zw)=nump(p-zw:p+zw)/(3.14159*r*r*dz)
        rhos(0:p+zw)=nums(0:p+zw)/(3.14159*r*r*dz)
RETURN
END

PRO sigcalc,rhos,sig,tau,qe,vs,epsair,p,zw,ecld,nz
 sig(0:p+zw)=rhos(0:p+zw)*(qe^2)/(9.11D-31*1.0D12)
 tau(0:p+zw)=epsair/sig(0:p+zw)
 PRINT,'tau=',tau(p),' rhos=',rhos(p)
 vs(0:p+zw)=ecld(0:p+zw)*qe/(9.11D-31*1.0D12)
 FOR j=0,p+zw DO BEGIN
 IF sig(j) LT 2.0D-12 THEN sig(j)=2.0D-12
 IF tau(j) GT epsair/2.0D-12 THEN tau(j)=epsair/2.0D-12
 ENDFOR
RETURN

PRO eupdate,dtnew,tau,ecld,nz,p,del0,zw,ebr,np,qe,vp,sig,epso
qzexp=DBLARR(nz)
FOR j=0,p+zw DO BEGIN
  IF sig(j)*dtnew LT 0.05 THEN BEGIN
    qzexp(j)=(1.-0.5*dtnew/tau(j))*dtnew
  ENDIF
  IF sig(j)*dtnew GE 0.05 THEN BEGIN
    qzexp(j)=tau(j)*(1.-EXP(-min(30.d0,dtnew/tau(j))))
  ENDIF
 ENDFOR
ecld(0:p+zw)=ecld(0:p+zw)*EXP(-dtnew/tau(0:p+zw))+$
           np(0:p+zw)*qe*vp*qzexp(0:p+zw)*epso
del0(0:p+zw)=ecld(0:p+zw)/ebr(0:p+zw)
RETURN
END
```